Ponderomotive action of light in the problem of multiple scattering of light in a randomly inhomogeneous medium

S. E. Skipetrov[a)] and S. S. Chesnokov
M. V. Lomonosov Moscow State University, 119899 Moscow, Russia

S. D. Zakharov, M. A. Kazaryan, and V. A. Shcheglov
P. N. Lebedev Physical Institute, Russian Academy of Sciences, 117924 Moscow, Russia

(Submitted 17 March 1998)
Pis'ma Zh. Éksp. Teor. Fiz. **67**, No. 9, 611–615 (10 May 1998)

The time correlation function of light reflected diffusely from a semi-infinite randomly inhomogeneous medium is calculated with allowance for the acceleration of the scatterers in the field of the laser beam incident on the medium. An analytical expression is found for the characteristic coherence time due to the ponderomotive action of light. It is shown that even with laser radiation power densities of the order of 1–10 W laser-acceleration effects substantially alter the character of the time autocorrelation function of the scattered light and must be taken into account in theoretical calculations. © *1998 American Institute of Physics.* [S0021-3640(98)00109-1]

PACS numbers: 42.25.Fx, 42.50.Vk, 78.66.Vs

It is well known that laser radiation can accelerate microparticles suspended in a liquid or gas up to substantial velocities.[1–3] Together with light pressure,[4] particle acceleration can be due to radiometric, gradient, or reactive forces,[5] which in many real situations exceed the force due to light pressure. The phenomena occurring when powerful laser beams interact with suspensions of micron- and submicron-size particles are very diverse: particle trapping, optical levitation,[2] formation of complicated hydrodynamic flows,[6] and so on.

In the present letter we analyze the role of laser-acceleration effects in the problem of dynamical multiple scattering of laser radiation by a suspension of micron- or submicron-size particles.

In a typical multiple scattering experiment[7] a laser beam with wavelength λ is focused into a spot of transverse size d on the surface of a cell containing spherical particles of radius $a \sim \lambda$ suspended in a liquid. For definiteness, we assume that $d < l_{tr}$ and $\lambda \ll l_{tr}$, where l_{tr} is the average transport mean free path of a photon in the medium, and also that the size of the cell is many times larger than l_{tr}. Then, if the coordinate origin is placed at the focusing point of the laser beam and the z axis is oriented along the beam axis, it can be assumed that the randomly inhomogeneous medium fills the half space

$z>0$. If the characteristic absorption length l_a is much greater than $l_{\rm tr}$, then the observed scattering will be of a substantially multiple character.

To calculate the time correlation function of the diffusely reflected light we shall employ the method of path integrals:[8] We shall consider the scattering of light in the medium as a random walk of individual photons over all possible trajectories. Each trajectory consists of a broken line at whose vertices the scattering centers are located. The light field $E(\mathbf{r},t)$ at the point $\mathbf{r}$ on the surface of the medium at time t is produced by the interference of partial waves scattering along the different trajectories. The correlation function of the field $G_1(\mathbf{r},\tau)=\langle E(\mathbf{r},t)E^*(\mathbf{r},t-\tau)\rangle$ is sensitive to the displacement of the scattering centers in the medium and is given by the expression[9]

$$G_1(\mathbf{r},\tau)=\sum_{n=1}^{\infty} I(\mathbf{r},n)\exp\left\{-\frac{1}{2}\langle\Delta\varphi^2(\tau)\rangle_n\right\}, \tag{1}$$

where $\langle\Delta\varphi^2(\tau)\rangle_n$ is the variance of the phase difference for two photons scattered along one and the same trajectory, consisting of n scattering events at times separated by the time interval τ. The averaging $\langle\ldots\rangle_n$ in Eq. (1) extends over all possible trajectories corresponding to n-fold scattering, and the summation extends over all orders of scattering n. $I(\mathbf{r},n)$ is the light intensity produced at the point $\mathbf{r}$ by scattering processes of order n. If the characteristic velocities of the scattering centers in the medium are much lower than the velocity of light, then it can be assumed that the motion of the scatterers has no effect on $I(\mathbf{r},n)$, which under the assumptions made above can be approximately calculated in the diffusion approximation.[7,10]

To simplify the exposition we shall confine ourselves to calculating the temporal coherence of the scattered radiation, which exits from the medium at a point in direct proximity (at a distance of the order of $l_{\rm tr}$) to the point of focusing of the incident radiation. Then $I(\mathbf{r},n)\propto n^{-5/2}\exp(-nl_{\rm tr}/l_a)$.[11]

In contrast to $I(\mathbf{r},n)$, $\langle\Delta\varphi^2(\tau)\rangle_n$ must be calculated with the dynamics of the scatterers in the medium taken into account. Ordinarily, the ponderomotive action of the light is neglected in so doing (see, for example, Ref. 9) and it is assumed that the scattering centers move as Brownian particles with diffusion coefficient D_B. In this case it is easy to show that

$$\langle\Delta\varphi^2(\tau)\rangle_n^{(B)}=\frac{\tau}{\tau_0}n, \tag{2}$$

where $\tau_0=(4k^2D_B)^{-1}$ and $k=2\pi/\lambda$.

We shall calculate $\langle\Delta\varphi^2(\tau)\rangle_n$ taking into account the light-induced motion of the scattering centers. For this we employ the result of Ref. 11, where a general scheme is proposed for calculating the dynamical multiple scattering by arbitrary scatterer fluxes. According to Ref. 11

$$\langle\Delta\varphi^2(\tau)\rangle_n^{(F)}=\frac{2}{15}\left(\frac{kl_{\rm tr}\tau}{\eta}\right)^2\int\left(\sum_{i\neq k}\sigma_{ik}^2(\mathbf{r}')\right)\rho_n(\mathbf{r}')\mathrm{d}^3\mathbf{r}', \tag{3}$$

where $\sigma_{ik}(\mathbf{r}')$ is the viscous stress tensor, η is the viscosity of the suspension, and

$$\rho_n(\mathbf{r}) = \frac{3}{2\pi l_{\rm tr}^2 r n} \exp\left\{ -\frac{3r^2}{l_{\rm tr}^2 n} \right\}. \tag{4}$$

The integration in expression (3) extends over the entire volume of the randomly inhomogeneous medium. However, formula (3) is applicable only if the velocity field **v(r)** of the scatterers in the randomly inhomogeneous medium is known. Therefore the next stage of the problem is to construct a model of the motion of the suspended particles in the liquid under the action of powerful laser radiation.

Since we have assumed that the beam incident on the medium is quite strongly focused ($d < l_{\rm tr}$), its ponderomotive action will be significant only in a narrow region of transverse size $\sim d$. However, the accelerated particles will drag the liquid and the liquid in turn will drag the particles that have not been directly affected by the laser radiation. As a result, a jet should form in the medium — even particles located quite far from the point of focusing of the laser beam will be entrained into collective motion. The formation of a light-induced jet was observed experimentally in Ref. 6. To find the velocity field **v(r)** in such a light-induced jet, it is sufficient to note the similarity between our problem and the ''submerged jet'' problem.[12] Indeed, according to what we have said above, the origin of coordinates can be treated approximately as a point source from which particles emanate in the direction of the z axis, temporarily forgetting about the reason for the appearance of this source. Then, neglecting the influence of the boundary of the medium we obtain in a spherical coordinate system[12]

$$v_r = \frac{P \cos\theta}{4\pi\eta r}, \quad v_\theta = -\frac{P \sin\theta}{8\pi\eta r}, \quad v_\phi = 0, \tag{5}$$

where P is the total momentum flux in the jet. Substituting expressions (5) into Eq. (3) gives

$$\langle \Delta\varphi^2(\tau) \rangle_n^{(F)} = \left(\frac{\tau}{\tau_F} \right)^2 f(n), \quad \text{where } \tau_F = \sqrt{10}\, \frac{\eta l_{\rm tr} \lambda}{P}, \tag{6}$$

$$f(n) = \exp\left\{ -\frac{3}{n} \right\} + \frac{3}{n} \mathrm{Ei}\left\{ -\frac{3}{n} \right\}, \tag{7}$$

and $\mathrm{Ei}(x)$ is the exponential integral.

Formulas (6) are the main result of our analysis. First, it should be noted that the dependence of $\langle \Delta\varphi^2(\tau) \rangle_n$ on τ for Brownian motion of scatterers ($\langle \Delta\varphi^2(\tau) \rangle_n^{(B)} \propto \tau$) is different from that for a light-induced jet ($\langle \Delta\varphi^2(\tau) \rangle_n^{(F)} \propto \tau^2$). Therefore laser-acceleration effects qualitatively change the form of the time correlation function of the diffusely reflected radiation. Moreover, the expression for the characteristic coherence time τ_F due to the ponderomotive action of the light is of definite interest. Consisting of a combination of hydrodynamic (η) and optical ($l_{\rm tr}, \lambda$) parameters together with a quantity (P) describing the efficiency of momentum transfer from the electromagnetic field to the medium, this expression can be obtained (to within a numerical factor) from dimensional considerations. We note that the Brownian motion of the scatters can be assumed to be

independent of light-induced motion, at least at low intensities. Then the expression for $\langle \Delta\varphi^2(\tau)\rangle_n$ with both types of motion taken into account can be written as a sum of two terms:

$$\langle \Delta\varphi^2(\tau)\rangle_n = \langle \Delta\varphi^2(\tau)\rangle_n^{(B)} + \langle \Delta\varphi^2(\tau)\rangle_n^{(F)}. \tag{8}$$

We shall now estimate the conditions under which the ponderomotive action of light is important for calculations of the temporal coherence of the scattered light. For this, evidently, it is necessary to specify the main mechanism of acceleration of the suspended particles in the laser field. For example, light pressure will play the main role for submicron-size polystyrene beads suspended in water, since light absorption in polystyrene is weak and all other mechanisms of acceleration are related with the absorption of light. Therefore $P \simeq W/c$, where W is the radiation power and c is the velocity of light in the medium. In this case the second term in Eq. (8) will be greater than the first term, if the radiation power exceeds the critical value

$$W > W_c(\tau,n) \simeq 4cl_{\mathrm{tr}} \sqrt{\frac{5\pi\eta k_B T}{3a} \frac{n}{\tau f(n)}}, \tag{9}$$

where k_B is Boltzmann's constant and T is the temperature of the suspension. In deriving formula (9) we employed the following expression for the diffusion coefficient of spherical particles in a suspension: $D_B = k_B T/6\pi\eta a$.

As one can see from expression (9), the critical power depends on the order of scattering n and on the time delay τ. Analysis shows that the ratio $n/f(n)$ is minimum for $n=5$, so that the maximum influence of the laser acceleration will be on photons scattered a small number of times (of the order of 5). At the same time, W_c decreases monotonically with increasing τ, so that it is most important to take laser acceleration effects into account when analyzing the ''tail'' of the correlation function.

To obtain an estimate, we set $a \sim 0.1$ μm and fix the volume particle concentration at 1%. Then $l_{\mathrm{tr}} \sim 200$ μm.[b)] For water $\eta \sim 10^{-3}$ Pa·s. We shall assume that the radiation wavelength λ equals 0.5 μm. As a result, for $n=5$ the critical power W_c will range from 15 W for $\tau = 1$ μs up to 0.5 W for $\tau = 1$ ms. As one can see, these critical values of the radiation power are low enough for the effect described in the present work to be observable experimentally. Nonetheless, the multiple-scattering of light by a microparticle jet induced by the light itself has still not been observed, since experiments are ordinarily performed for laser power no greater than 1 W and for time delays in the range $\tau < 1$ ms.

In conclusion, it should be noted that in accordance with the results obtained laser acceleration of microparticles should play a large role in experiments on dynamical multiple scattering of light in randomly inhomogeneous media even with laser powers of the order of several watts. The analytical expressions obtained in the present letter make it possible to estimate the critical laser power for which the ponderomotive action of the light must be taken into account in the calculations of the statistical characteristics of the scattered radiation. Our results are of great practical value in connection with the increasing interest in using optical methods for studying the dynamics of particles in turbid media,[13] for example, in optical diagnostics problems.[14]

[a)]e-mail: skipetr@fort.phys.msu.su
[b)]The calculation was performed using the standard formulas of the Mie theory.[10]

[1] G. A. Askar'yan, Zh. Éksp. Teor. Fiz. **42**, 1567 (1962) [Sov. Phys. JETP **15**, 1088 (1962)].
[2] A. Ashkin, Sci. Am. **226**(2), 63 (1972).
[3] S. D. Zakharov, M. A. Kazaryan, and N. P. Korotkov, JETP Lett. **60**, 322 (1994).
[4] P. N. Lebedev, *Collected Works* [in Russian], Academy of Sciences Press, Moscow, 1963; V. Fabricant, Usp. Fiz. Nauk **42**, 282 (1950).
[5] G. A. Askar'yan, Usp. Fiz. Nauk **110**, 115 (1973) [Sov. Phys. Usp. **16**, 414 (1973)]; G. A. Askar'yan and E. M. Moroz, Zh. Éksp. Teor. Fiz. **43**, 2319 (1962) [Sov. Phys. JETP **16**, 1638 (1962)].
[6] M. A. Kazaryan, N. P. Korotkov, and S. D. Zakharov, Phys. Scr. **52**, 678 (1995); S. D. Zakharov, K. I. Zemskov, M. A. Kazaryan, and N. P. Korotkov, Izv. Ross. Akad. Nauk, Ser. Fiz. **56**, 182 (1992).
[7] A. Ishimaru, *Wave Propagation and Scattering in Random Media*, Academic Press, New York, 1978 [Russian translation, Nauka, Moscow, 1981].
[8] R. P. Feynman and A. R. Hibbs, *Quantum Mechanics and Path Integrals*, McGraw-Hill, New York, 1965 [Russian translation, Mir, Moscow, 1968].
[9] G. Maret and P. E. Wolf, Z. Phys. B **65**, 409 (1987); P. M. Chaikin, D. J. Pine, D. A. Weitz, and E. Herbolzheimer, Phys. Rev. Lett. **60**, 1134 (1988).
[10] P. M. Morse and H. Feshbach, *Methods of Mathematical Physics*, McGraw-Hill, New York, 1953, Vol. 1 [Russian translation, IL, Moscow, 1958].
[11] D. J. Bicout and R. Maynard, Physica A **199**, 387 (1993).
[12] L. D. Landau and E. M. Lifshitz, *Fluid Mechanics*, 2nd ed., Pergamon Press, New York, 1987 [Russian original, Nauka, Moscow, 1986].
[13] M. Heckmeier, S. E. Skipetrov, G. Maret, and R. Maynard, J. Opt. Soc. Am. A **14**, 185 (1997); S. E. Skipetrov and I. V. Meglinskiĭ, Zh. Éksp. Teor. Fiz. **113**, 1213 (1998) [JETP **86**, 661 (1998)].
[14] V. V. Tuchin Phys. Usp. **167**, 517 (1997).

Translated by M. E. Alferieff

Dynamics of self-similar dispersion-managed soliton presented in the basis of chirped Gauss–Hermite functions

S. K. Turitsyn[a)] and V. K. Mezentsev
Institute of Automation and Electrometry, Russian Academy of Sciences, 630090 Novosibirsk, Russia

(Submitted 20 March 1998)
Pis'ma Zh. Éksp. Teor. Fiz. **67**, No. 9, 616–621 (10 May 1998)

Applying chirped Gauss–Hermite orthogonal functions we present an analytical description of the breathing dynamics of the chirped dispersion-managed soliton. The theory describes both self-similar evolution of the central, energy-containing core and accompanying nonstationary oscillations of the far-field tails of an optical pulse propagating in a fiber line with arbitrary dispersion map. © *1998 American Institute of Physics.* [S0021-3640(98)00209-6]

PACS numbers: 42.81.Dp, 42.79.Sz

Dispersion management (variation of the chromatic dispersion along the line) is an attractive technique that can be used to enhance the performance of fiber communication links both for soliton and non-soliton transmission (see, e.g., Refs. 1–6). Recent developments in optical fiber communications have demonstrated that dispersion management makes the features of soliton transmission close to those of non-soliton transmission.[4–6]. The dispersion-managed (DM) soliton is a new type of information carrier with properties[1–17] rather different from those of the traditional fundamental soliton (the soliton solution of the integrable nonlinear Schroedinger equation[18](NLSE)). In particular, during propagation along the fiber line the DM soliton undergoes rapid self-similar breathing-like oscillations of the width and power, and it is chirped and can propagate at zero or even normal average dispersion. A theory of DM solitons in systems with strong dispersion management has been presented in Ref. 17. The first implementation of commercial fiber optical networks based on DM solitons has recently been reported.[6] Although the basic theory of DM solitons has been already presented in Refs. 8,7,12–14,17, because of the wide range of possible practical system configurations many interesting problems are still open. An intriguing open theoretical problem is the origin and structure of the oscillatory tails of the DM soliton.[16,11] As was shown in Ref. 16, such tails manifest themselves as non-self-similar modulations of the soliton profile during the compensation period, though their amplitudes are rather small compared with the main peak. In this paper we present a systematic method to describe the dynamics of the self-similar core and oscillatory tails of the DM soliton using an orthogonal set of chirped Gauss–Hermite functions. This approach can be very useful in numerical modeling of the dynamics of an arbitrary initial signal in dispersion-managed communication systems, including chirped return-to-zero and non-return-to-zero formats.[4,5]

Pulse dynamics in dispersion-managed optical transmission systems is governed by the NLSE with periodic coefficients:

$$iA_z + d(z)A_{tt} + c(z)|A|^2 A = 0, \quad d(z) = \lambda_0^2 D(z) L/(4\pi c_l t_0^2),$$

$$c(z) = P_0 L \sigma \exp(-2L\gamma z). \tag{1}$$

Here the propagation distance z is normalized by the dispersion compensation period L, time t is normalized by the parameter t_0, and the envelope of the electric field is scaled by the power parameter P_0. The periodic function $c(z)$ takes into account the power decay due to fiber losses and the periodic amplification, σ being the nonlinear coefficient and γ describing the fiber losses. The lumped action of the amplifiers is taken into account through a transformation of the pulse power at junctions corresponding to the locations of the amplifiers. The normalized chromatic dispersion $d(z) = \tilde{d}(z) + \langle d \rangle$ represents the sum of a periodic, rapidly varying (over one compensation period) high local dispersion ($\tilde{d}$) and a constant residual dispersion ($\langle d \rangle \sim \langle c \rangle \sim \tilde{c} \ll \tilde{d}$). Here λ_0 is the operating wavelength, c_l is the speed of light, and D is the local dispersion coefficient. The amplification distance in general can be different from the compensation period, but without loss of generality we assume here that c and d have the same period L. Nonlinearity comes into play on the scale $Z_{NL} \sim 1/(P_0\sigma) \gg L$, and the physical problem that we consider is how to describe an asymptotic solution that strikes a balance between effects of nonlinearity, average dispersion, and the averaged effects resulting from the rapid variations of the dispersion $d(z)$ and power $c(z)$. The mathematical formulation of this problem is how to average Eq. (1) if the periodic oscillations of $d(z)$ are large. A small parameter in the problem is $L/Z_{NL} \ll 1$. Note that due to the large variations of d, direct approaches like the averaging method known for the so-called Kapitza pendulum problem[19] do not work here, because the rapidly varying field is of the same order as the averaged (slowly varying) part. Judging from the results of numerical simulations, we can say that qualitatively the solution of Eq. (1) represents a central peak, which oscillates with z in self-similar manner, and tails that are not self-similar and have lower power than the main peak but are responsible for soliton–soliton interaction. An important feature of the DM soliton is the rapid oscillation of the phase (quadratic in time near the center) during the period. The typical shape of the DM soliton found numerically is shown in Fig. 1.

As a first step, we remove from Eq. (1) the fast phase dynamics due to the large variations of d. To describe the rapid self-similar dynamics of the main peak, let us consider the following[17] exact transformation of the function $A(z,t)$, which, as a matter of fact, is a modification of the Talanov transform known in self-focusing theory:[20]

$$A(t,z) = N \exp\left[i \frac{M(z)}{T(z)} t^2 \right] \frac{Q(x,z)}{\sqrt{T(z)}}, \quad x = \frac{t}{T(z)}, \tag{2}$$

here T and M are periodic solutions of the following equations first obtained in Refs. 8 and 13:

$$\frac{dT}{dz} = 4d(z)M; \quad \frac{dM}{dz} = \frac{d(z)}{T^3} - \frac{c(z)N^2}{T^2}. \tag{3}$$

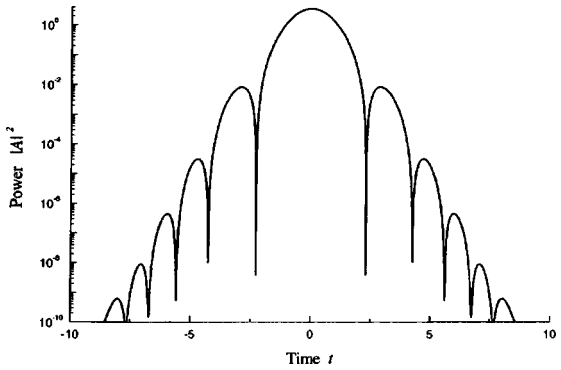

FIG. 1. Shape of the dispersion-managed soliton (periodic solution of Eq. (1)) is shown at the beginning (end) of the periodic cell.

The coefficient N in (3) is determined by the requirement that T and M be a periodic solution of equation (3). We then obtain a partial differential equation for $Q(x,z)$:

$$i\frac{\partial Q}{\partial z}=\frac{\delta H}{\delta Q^*}=-\frac{d}{T^2}(Q_{xx}-x^2Q)-\beta(z)(|Q|^2Q+x^2Q),$$

$$H=\int\left[\frac{d}{T^2}(|Q_x|^2+x^2|Q|^2)-\beta(z)\left(\frac{1}{2}|Q|^4+x^2|Q|^2\right)\right]dt. \tag{4}$$

Here $\beta(z)=c(z)N^2/T$. Next, we expand $Q(x,z)$ using the complete set of orthogonal normalized Gauss–Hermite functions $Q(x,z)=\Sigma_n b_n(z)f_n(x)$ with

$$(f_n)_{xx}-x^2f_n=\lambda_n f_n,\quad \lambda_n=-1-2n,\quad f_n(x)=\frac{1}{\sqrt{2^n n!\sqrt{\pi}}}\exp\left(-\frac{x^2}{2}\right)H_n(x). \tag{5}$$

Here $H_n(x)$ is the nth-order Hermite polynomial, and the coefficients b_n are given by the scalar product in $\mathcal{L}^2$ with f_n: $b_n=\langle f_n|Q\rangle$. Inserting this expansion into (4), after straightforward calculations we obtain a system of ordinary differential equations for the coefficients b_n:

$$i\frac{db_n}{dz}=\frac{\delta H_b}{\delta b_n^*}=-\frac{d}{T^2}b_n\lambda_n-\beta(z)\sum_m b_m S_{n,m}-\beta(z)\sum_{m,l,k} b_m b_l b_k^* R_{m,l,k,n}=0 \tag{6}$$

the Hamiltonian H_b is

$$H_b=-\frac{d}{T^2}\sum_{n=0}^{n=\infty}\lambda_n|b_n|^2-\beta(z)\sum_{n,m}S_{n,m}b_m b_n^*-\frac{\beta(z)}{2}\sum_{n,m,l,k}R_{n,m,l,k}b_l b_m b_n^* b_k^*. \tag{7}$$

Here we introduce the notation

$$S_{n,m}=\langle f_m|x^2f_n\rangle=\int_{-\infty}^{+\infty}f_m(x)x^2f_n(x)dx,$$

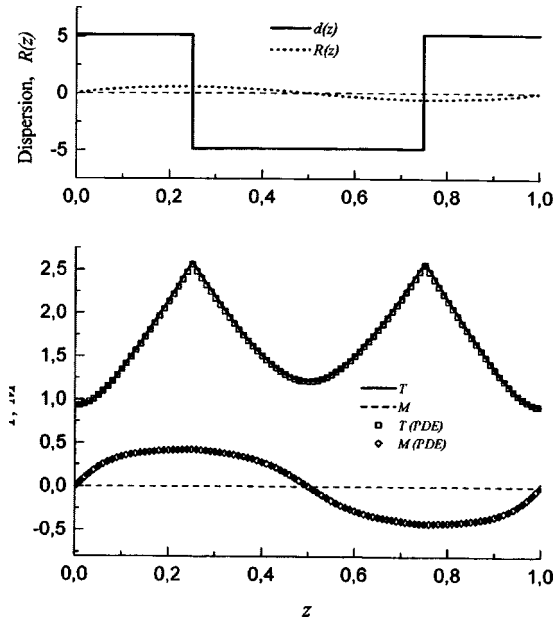

FIG. 2. The dynamics of T (solid line — solution of Eqs. (3) and squares — solution of Eq. (1)), M (long-dashed line — solution of Eqs. (3) and rhombus — solution of Eq. (1)) and R (short-dashed line) over one period is presented for the dispersion map (above) $d(z)=\pm d+\langle d\rangle$, with $d=5$ and $\langle d\rangle=0.15$. A lossless model with $c(z)=1$ is considered.

$$R_{n,m,l,k}=\langle f_m|f_nf_lf_k\rangle=\int_{-\infty}^{+\infty}f_n(x)f_m(x)f_l(x)f_k(x)dx. \tag{8}$$

Since integrals of the form $\int x^n e^{-\alpha x^2}$ can be calculated analytically, it is possible to determine any $S_{n,m}$ and $R_{n,m,l,k}$. As a next step we remove the rapid oscillations by the simple transform $b_n=B_n e^{iR(z)\lambda_n}$ with $dR/dz=d(z)/T(z)^2-\langle d/T^2\rangle$. Figure 2 shows the typical dynamics of T, M, and R for a specific practical dispersion map d. The equation for the B_n reads:

$$i\frac{dB_n}{dz}+\left\langle\frac{d}{T^2}\right\rangle\lambda_nB_m+\beta(z)\sum_m e^{i(\lambda_m-\lambda_n)R(z)}S_{n,m}B_m$$

$$+\beta(z)\sum_{m,l,k}e^{i(\lambda_m+\lambda_l-\lambda_k-\lambda_n)R(z)}B_mB_lB_k^*R_{m,l,k,n}=0. \tag{9}$$

An averaging procedure based on the Lie transform[21] can be applied directly to Eq. (9). The field B_n is then composed from slowly varying (U_n) and rapidly varying (η_n, $d\eta_n/dz\gg\eta_n$) parts: $B_n=U_n+\eta_n+\ldots$, where $\eta_n\ll U_n$. This procedure is a natural generalization of the result obtained in Ref. 17 for the case of strong dispersion management. Averaging over one period gives

$$i\frac{dU_n}{dz}=\frac{\delta H}{\delta U_n^*}=-\left\langle\frac{d}{T^2}\right\rangle\lambda_n U_n-\sum_m\langle\beta(z)e^{i(\lambda_m-\lambda_n)R(z)}\rangle$$

$$\times S_{n,m}U_m-\sum_{m,l,k}\langle\beta(z)e^{i(\lambda_m+\lambda_l-\lambda_k-\lambda_n)R(z)}\rangle U_m U_l U_k^* R_{m,l,k,n}=0. \tag{10}$$

Hamiltonian H reads

$$H=\left\langle\frac{d}{T^2}\right\rangle\sum_{n=0}^{n=\infty}(1+2n)|U_n|^2-\sum_{n,m}\langle\beta(z)e^{2i(n-m)R(z)}\rangle S_{n,m}U_m U_n^*$$

$$-\frac{1}{2}\sum_{n,m,l,k}\langle\beta(z)e^{2i(n+k-l-m)R(z)}\rangle R_{n,m,l,k}U_m U_l U_n^* U_k^*. \tag{11}$$

The averaged Eq. (10) is the main result of the present paper. A solution of equation (10) of the form $U_n=F_n\exp(ikz)$ (with F_n independent of z) gives the DM soliton for any given dispersion map. The equation obtained permits a rigorous mathematical description of the properties of DM solitons and more generally the propagation of any input signal for an arbitrary dispersion map. An important observation from Eq. (11) is that the sign of the average effective dispersion $\langle d/T^2\rangle$ plays a crucial role in the dynamics of a dispersion-managed pulse. The basic condition $\langle d\rangle>0$ that ensures the existence of the traditional fundamental soliton is replaced by the requirement $\langle d/T^2\rangle>0$ for the DM soliton. This explains a possibility, observed in Ref. 16, of transmitting a DM soliton at zero or normal average dispersion. We present an expansion of the DM soliton in terms of chirped Gauss–Hermite functions. A similar approach has been used[22] to describe the propagation of linear chirped pulse. The dynamics of any initial bell-shaped pulse (the bell shape provides rapid convergence of the expansion) can be effectively described using the method developed here. Any well-localized pulse will be represented by a limited number of terms in the expansion. This makes the basis under consideration very useful in different practical applications and numerical simulations of dispersion-managed transmission systems. The above expansion plays a role in the present problem which is similar to that played by the Fourier transform in linear problems.

The solution of equation (1) in the general case can be expanded in the complete set of chirped Gauss–Hermite functions:

$$A(z,t)=N\frac{\exp\left(i\frac{M}{T}t^2\right)}{\sqrt{T}}\sum_{n=0}^{n=\infty}B_n(z)f_n\left[\frac{t}{T(z)}\right]\exp[i\lambda_n R(z)], \tag{12}$$

where

$$B_n(z)=\exp[-i\lambda_n R(z)]\int_{-\infty}^{\infty}dx\ f_n(x)\exp(-iMTx^2)A[z,xT(z)].$$

Figure 3 shows a plot of the evolution over one period of few first $|B_n|^2$ calculated from the expansion of the true DM soliton. It is seen that the B_n^2 decay with increasing n, although due to the smallness of B_2 this decay is not exactly monotonic. The power of the solution in the general case is expressed as ($B_n=|B_n|\exp(i\Phi_n)$)

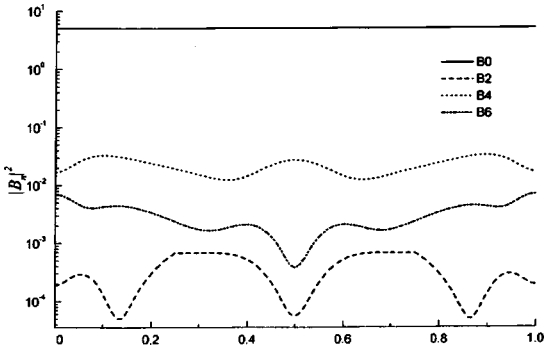

FIG. 3. Evolution over one period of the first coefficients $|B_n|^2$ in the expansion of dispersion-managed soliton (found numerically by solving Eq. (1)).

$$|A(z,t)|^2=\frac{N^2}{T(z)}\sum_n |B_n(z)|^2\left|f_n\left[\frac{t}{T(z)}\right]\right|^2+\frac{N^2}{T(z)}\sum_{n,m} f_n\left[\frac{t}{T(z)}\right]$$
$$\times f_m\left[\frac{t}{T(z)}\right]|B_n||B_m|\cos[2(n-m)R(z)+\Phi_m-\Phi_n]. \quad (13)$$

The first term in Eq. (13) is the self-similar core of the solution, and the last term is responsible for non-self-similar oscillations of the tails inside the compensation cell. It should be pointed out that the oscillating tails are an inherent part of the DM soliton but not of the long-lived radiative term as in the case of the NLSE soliton.[23]

To conclude, we have derived an average equation describing the shape of the dispersion-managed soliton for an arbitrary dispersion map. Using chirped Gauss–Hermite functions we have described both the self-similar structure of the main peak and the oscillating tails of the dispersion-managed pulse. The complete set of orthogonal chirped Gauss–Hermite functions is very useful in numerical simulations of the evolution of an arbitrary bell-shaped initial signal down a dispersion-managed fiber system.

This research has been supported in part by RFBR (Grant 96-02-19131-a) and INTAS (Grant 96-0413).

[a)]e-mail: tur@okibox.iae.nsk.su

[1] M. Suzuki, I. Morita, N. Edagawa *et al.*, Electron. Lett. **31**, 2027 (1995).
[2] A. Sahara, H. Kubota, and M. Nakazawa, IEEE Photonics Technol. Lett. **9**, 1179 (1997).
[3] D. Le Guen, F. Favre, M. L. Moulinard *et al.*, ECOC'97 (Edinburgh), Post Deadline paper **5**, 25 (1997).
[4] M. Suzuki *et al.*, Post Deadline presentation, PD17-1, OFC'98, San Jose, USA.
[5] N. S. Bergano *et al.*, Post Deadline presentation, PD12-1, OFC'98, San Jose, USA.
[6] N. Robinson *et al.*, Post Deadline presentation, PD19-1, OFC'98, San Jose, USA.
[7] N. Smith, F. M. Knox, N. J. Doran *et al.*, Electron. Lett. **32**, 54 (1996).
[8] I. Gabitov and S. K. Turitsyn, Opt. Lett. **21**, 327 (1996); JETP Lett. **63**, 862 (1996); ''Averaged pulse dynamics in the cascaded transmission systems with a passive dispersion compensation,'' Preprint Los Alamos, LAUR– 95–3633, October 13 (1995).
[9] T. Georges and B. Charbonnier, IEEE Photonics Technol. Lett. **9**, 127 (1997).
[10] M. Matsumoto and H. A. Haus, IEEE Photonics Technol. Lett. **9**, 785 (1997).
[11] E. A. Golovchenko, A. N. Pilipetskii, and C. R. Menyuk, Opt. Lett. **22**, 793 (1997).

[12] I. Gabitov, E. G. Shapiro, and S. K. Turitsyn, Opt. Commun. **134**, 317 (1996); Phys. Rev. E **55**, 3624 (1997).
[13] E. Shapiro and S. K. Turitsyn, Opt. Lett. **22**, 1544 (1997); Phys. Rev. E **56**, R4951 (1997).
[14] A. Hasegawa, Y. Kodama, and A. Maruta, Opt. Fiber Technol. **3**, 197 (1997).
[15] N. Kutz, P. Holmes, S. Evangelides, and J. Gordon, J. Opt. Soc. Am. B **15**, 87 (1997).
[16] J. H. B. Nijhof, N. J. Doran, W. Forysiak, and F. M. Knox, Electron. Lett. **33**, 1726 (1997).
[17] S. K. Turitsyn, JETP Lett. **65**, 845 (1997).
[18] V. E. Zakharov and A. B. Shabat, Zh. Eksp. Teor. Fiz. **60**, 136 (1971) [Sov. Phys. JETP **33**, 77 (1971)].
[19] L. D. Landau and E. M. Lifshitz, *Mechanics*, Pergamon Press, Oxford (1992).
[20] V. I. Talanov, JETP Lett. **11**, 199 (1970).
[21] A. Hasegawa and Y. Kodama, Opt. Lett. **15**, 1444 (1990); Phys. Rev. Lett. **66**, 161 (1991).
[22] P. Lazaridis, G. Debarge, and P. Gallion, Opt. Lett. **22**, 685 (1997).
[23] E. A. Kuznetsov, A. V. Mikhailov, and I. A. Shimokhin, Physica D **87**, 201 (1995).

Published in English in the original Russian journal. Edited by Steve Torstveit.

X-ray generation in low-voltage vacuum discharges

N. Vogel[a)]
University of Technology Chemnitz, Department of Physics, 09107 Chemnitz, Germany

(Submitted 20 March 1998; resubmitted 2 April 1998)
Pis'ma Zh. Éksp. Teor. Fiz. **67**, No. 9, 622–627 (10 May 1998)

The dynamics of x-ray emission from a low-voltage laser-induced discharge was studied with the aid of a picosecond x-ray streak camera. Directed x-ray emission in the spectral range from 100 eV to 10 keV in the form of point sources and thin layers with lifetimes ranging from 30 ps to 1 ns was observed in a low-voltage vacuum discharge ($U=150$ V) initiated by a picosecond laser beam. X-ray emission from a discharge was detected with a time delay (1–20 ns) relative to ignition by the laser beam in order to prevent the radiation of the laser plasma from entering the detector. Detection of directed x-ray emission in a low-voltage vacuum discharge is demonstrated. © *1998 American Institute of Physics.* [S0021-3640(98)00309-0]

PACS numbers: 52.80.Vp, 52.25.Nr, 07.85.Fv

The nature of vacuum sparks and arc discharges is still not completely understood despite the fact that they have been an object of investigation now for several decades in numerous research groups. One of the most important questions is still the question of how kiloampere currents can be conducted from the surface of a cold cathode through the vacuum gap. Very recent experimental and theoretical developments[1–4] have revealed many interesting effects in laser-induced vacuum discharges. They include: 1) Generation of nonstationary emission centers on the moving boundary of the cathode flame, so-called ''shooting solitons.'' The current density in them can reach values 10^{10}–10^{15} A/m^2 (Refs. 1–3). 2) Aperiodic focusing and defocusing of the current in the volume of the flame (typical time of the order of 1–4 ns),[3] when high-conductivity microchannels, along which the current streams, form in the region of nonideal plasma (where a ''metal–insulator'' transition occurs). 3) The development of ionization–overheating instability as a result of intense heating of the periphery of the cathode flame by ''shooting solitons.'' In this case the temperature of the plasma current can briefly (100 ps) reach 200 eV in a low-voltage discharge.[1–3] Finally, plasma-erosion circuit-opening in small electrode gaps, where the voltage drop in individual regions of the plasma flame can reach several kilovolts and higher.[2] These processes should all be accompanied by generation of x rays, as was pointed out in Refs. 1–4.

The objective of the present work is to investigate experimentally x-ray generation in a pulsed vacuum discharge induced by intense laser radiation (laser pulse duration 100 ps, pulse energy 30–60 mJ, wavelength 1064 nm) with a relatively low voltage between the copper electrodes ($U=150$ V). The x rays were detected with time delays longer than 1 ns relative to discharge ignition in order to detect reliably the radiation not from the

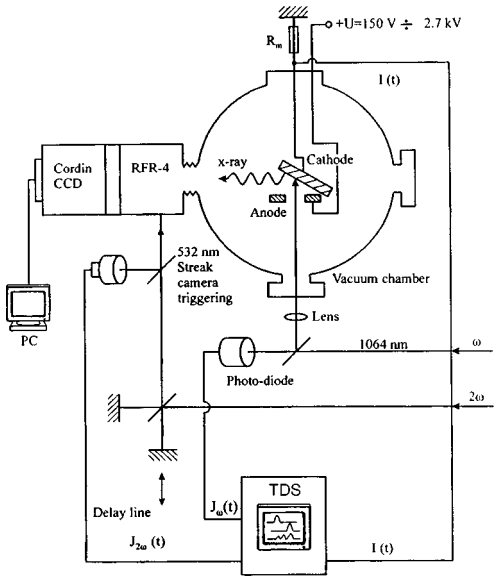

FIG. 1. Experimental arrangement for detecting x rays.

laser plasma but rather from the spark and arc stages of the discharge. In the experiments described below, the time-resolved radiation from the plasma of a vacuum discharge was investigated with an x-ray streak camera.[5] The cathode, which consisted of a flat 10 $\times$10 mm copper plate, was secured in the vacuum chamber, where a vacuum no worse than 10^{-5} Torr was maintained. The anode consisted of a narrow, tapered strip, the apex of which contained an opening 300 μm in diameter for focusing the laser beam on the cathode surface. The distance between the electrodes varied from 50 to 150 μm. The inductance of the electrode configuration did not exceed 150 nH. A 50-Ω coaxial cable was charged from the power source up to 150 V. The discharge duration, which was determined by the cable length, was equal to 750 ns. The discharge current was detected with a wide-band Tektronix TDS 620 digital oscilloscope (500 MHz bandwidth) with the aid of a calibrated current shunt in the discharge circuit. The oscilloscope was actuated by a signal from a picosecond photodiode after the radiation from the laser igniting pulse entered.

The experimental arrangement is shown in Fig. 1. Radiation from a Q-switched Nd:YAG laser at $\lambda = 1064$ nm was focused through the anode onto the cathode surface into a region 100 μm in diameter. The power flux density in this case was equal to 8 $\times 10^{12}$ W/cm^2. The plasma radiation from the electrode gap was detected with an x-ray streak camera.[5] An interchangeable gold photocathode was formed on a carbon film ranging in thickness from 0.2 to 2 μm, and the spectral detection range was 0.1–10 keV. According to the calculations of Ref. 5, the physical time resolution of the streak camera, determined by the difference of the travel times of the photoelectrons emanating with different velocities from different sections of the photocathode up to the deflecting plates, does not exceed 10 ps for an Au photocathode. The image is recorded from the output screen (fiber-optic plate) with the aid of a cooled CCD camera (Cordin CCD). The image

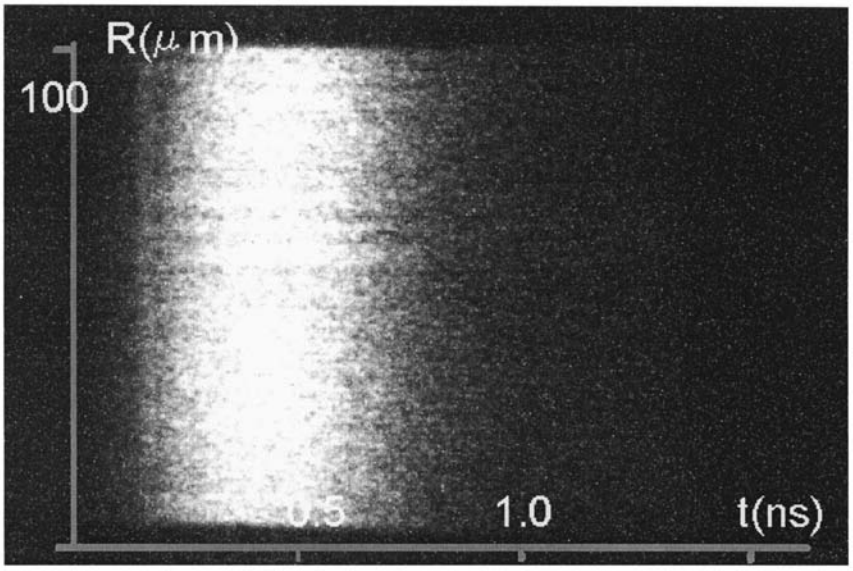

FIG. 2. Streak photograph of emission from a laser-induced plasma on a Cu target with the aid of a focused 60 mJ, 100 ps, laser pulse at wavelength 1064 nm.

signals were processed in the 14 bit range with specially developed image processing programs (Cordin CCD Readout System). The streak camera was mounted on the vacuum chamber, and the output slit of the chamber was positioned 35 cm from the center of the electrode. An image of a laser plasma spot from a 50–150 μm segment was projected onto the photocathode of the streak camera, which performed a temporal ''unfolding'' of the image obtained. When the image of the laser-plasma spot (which was 100 μm in diameter) was projected onto the entrance slit of the streak camera (15 mm high and 150 μm wide), a spatial resolution of 0.31 μm/pixel was obtained. The triggering of the sweep of the streak camera was synchronized to different stages of the laser-induced discharge with the aid of a laser signal at the second harmonic ($\lambda = 532$ nm), which was delayed by an optical delay line relative to the ignition pulse by an amount ranging from 3 to 30 ns. The delay of the triggering with respect to the light input did not exceed 5 ns, so that it was possible to detect radiation at the initial stage of breakdown in the presence of the laser radiation (approximately 500 ps) as well as in the spark and arc stages of the discharge. Interchangeable sweep units with rates of 3–30 ns/screen were used. Radiation from a low-current pulsed vacuum discharge with a maximum recorded current of 3 A was used. The discharge current had a square shape with a duration of 750 ns. When the laser plasma was initiated without voltage across the gap, the x-ray pulse had a uniform structure. The pulse duration is much longer than that of the warming pulse (100 ps) and equals 250 ps (wide-band emission in the spectral range 0.1–10 keV). As is well known, when copper targets are irradiated with 1064 nm laser radiation with power flux densities of the order of 10^{13} W/cm^2 the temperature reaches 200 eV in the laser plasma and 1 keV for the fast component of the plasma.[6] Figure 2 shows a photograph of the spatiotemporal detection of the x radiation for only the laser plasma. One can see from the photograph that the duration of the radiation does not exceed 250 ps and the structure of the emission

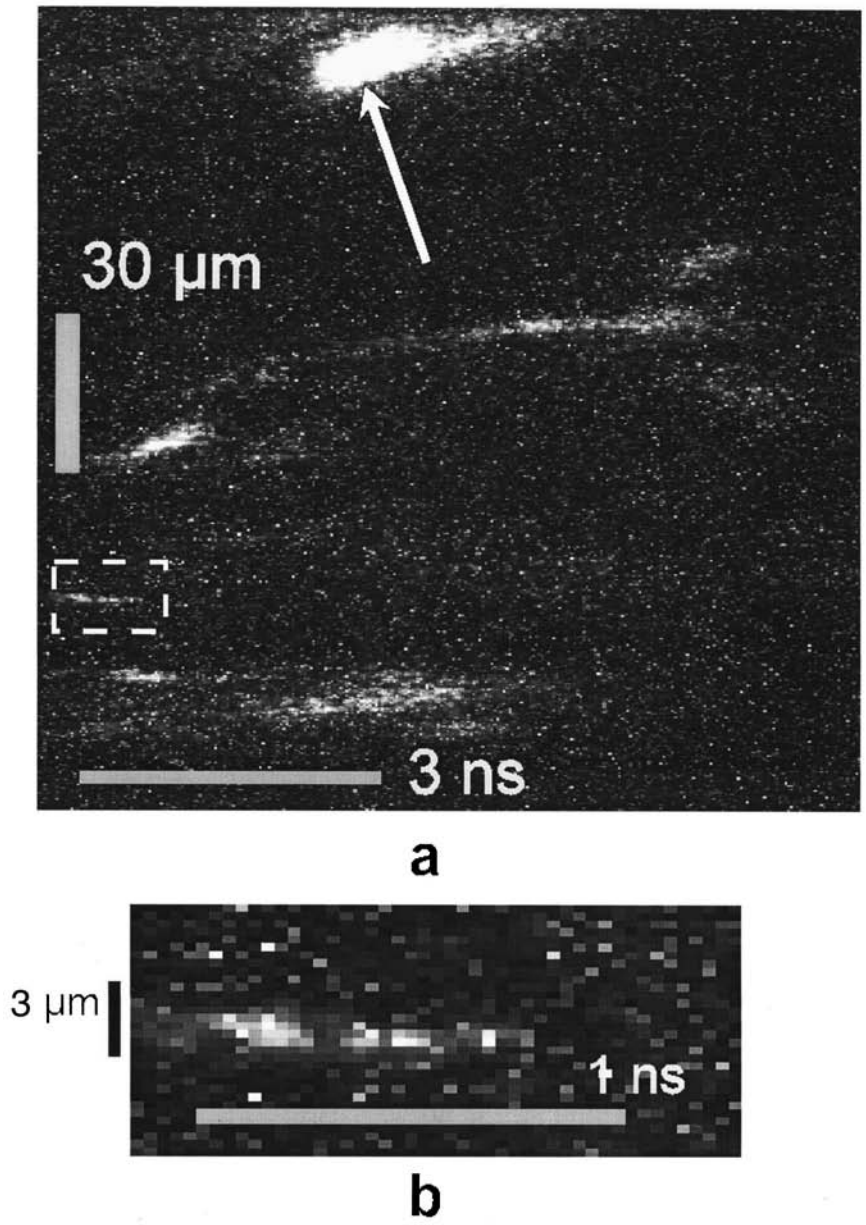

FIG. 3. a — Streak photograph of x-ray emission with time delay $t = 16.49$ ns. The arrow at the top of the photograph marks the possible appearance of radiation in the anode region; b — enlarged fragment of the photograph separated by the dashed line.

is uniform. The spatial distribution of the x radiation changes substantially if even a voltage as low as 150 V is applied to the electrodes. Figures 3, 4, and 5 show streak photographs reflecting the dynamics of the spatial distribution of the x radiation for a

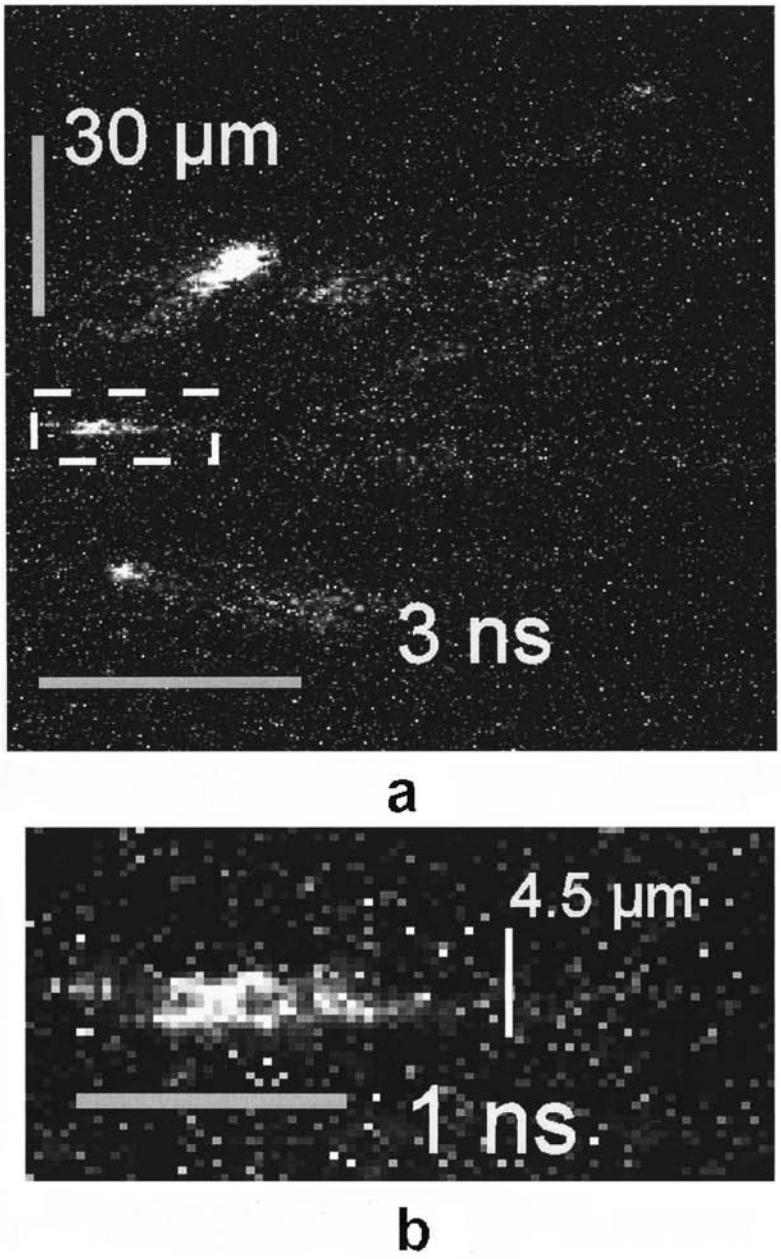

FIG. 4. a — Streak photograph of x-ray emission from a laser-induced discharge with voltage $U=150$ V for a time delay $t=16.49$ ns relative to the ignition pulse; b — enlarged fragment, separated by the dashed line, of the photograph.

laser-induced pulsed discharge with $U=150$ V between Cu electrodes separated by 50 μm. The image was recorded with a delay $t=16.49$ ns after ignition of the discharge by an infrared beam on the cathode surface. The scan rate was equal to 30 ns/screen. It

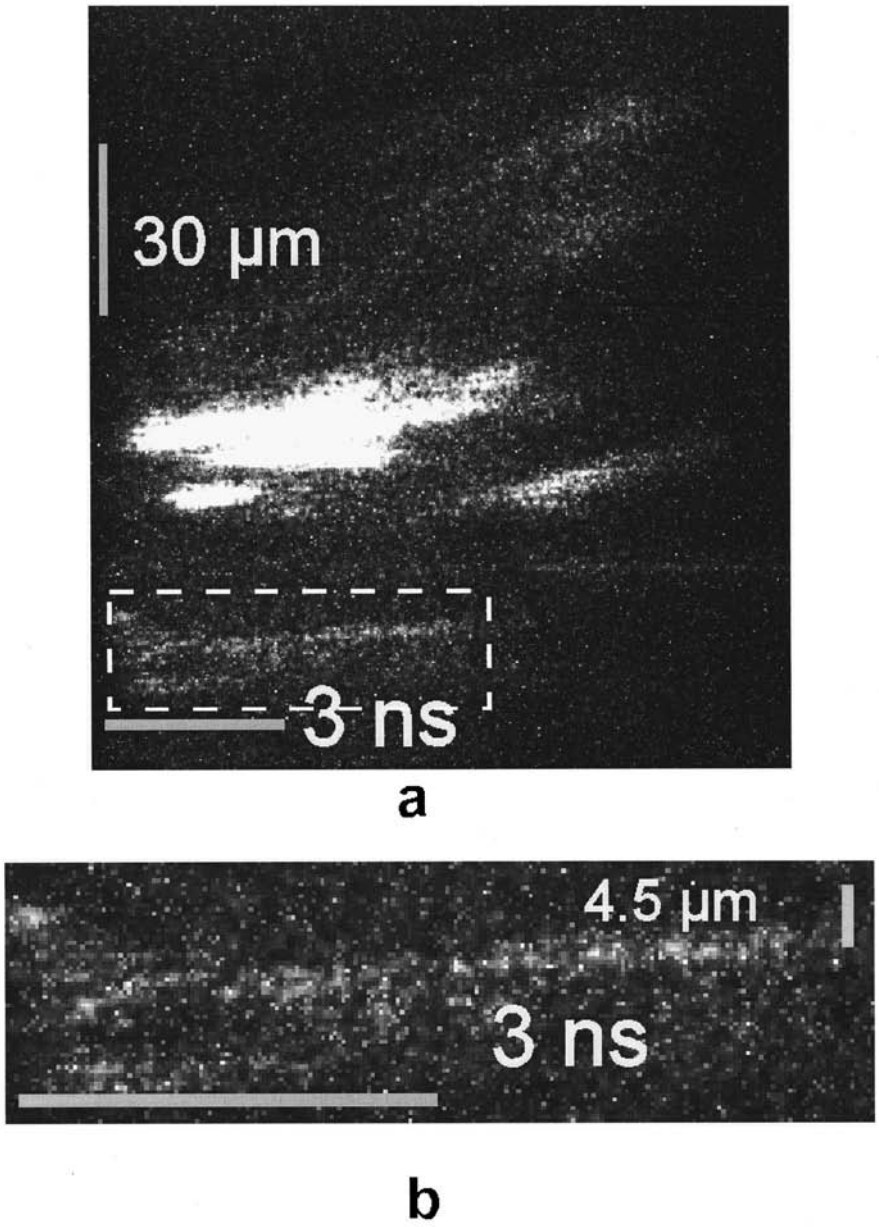

FIG. 5. a — Streak photograph of x-ray emission from a laser-induced discharge with voltage $U=150$ V for a time delay $t=16.49$ ns relative to the ignition pulse; b — enlarged fragment, separated by the dashed line, of the photograph.

should be noted that the reproducibility of the experimental results, i.e., the observed structure of the emission, was very good, as can be seen from the streak photographs presented for the same experimental conditions in Figs. 3, 4, and 5. A discrete emission structure is clearly seen. The size of the emitting sources is 1–10 μm and their lifetime

is 0.030–2.5 ns. It is obvious that two to five point sources can exist simultaneously on a 150 μm circle. The emission of radiation from the plasma dots can decrease and increase at the same spatial location in a time interval from 30 to 150 ps (see, for example, Figs. 3b, 4b, 5b). Contraction of the plasma channel to a radius of the order 1 μm can be seen in the enlarged streak photographs (Fig. 4b and 5b), while contraction to 0.3 μm can be seen in Fig. 3b. Besides groups of point sources, which leave horizontal tracks on the image scan, one can see several tracks that make an angle with the horizontal line of the trace, indicating motion of the source relative to the detection slit. The velocity of the moving sources can be determined from the inclined tracks and equals $(3-10)\times 10^3$ m/s for the time interval 1–2.5 ns. Evidently, if the expanding plasma touches the anode surface, hot spots can appear on the anode. From the photographs in Figs. 3a and 5a one can see the appearance of emission regions 10 μm in size with a duration of the order of 1–1.5 ns.

The velocity of the expanding plasma can be determined from the inclined track in Fig. 3a and equals 1.2×10^6 cm/s, in agreement with the value of the known expansion rate of the plasma of the cathode flame from the emission zone in a vacuum arc for copper.[7] For a 50 μm gap the expanding plasma requires ~ 4 ns to reach the anode surface. When the hot plasma touches the anode, intense vaporization starts in a local region and the cold nonconducting vapor increases the resistance in the discharge gap. As a result of the potential jump, the electric field intensity, distributed nonlinearly in space, can correspondingly increase and give rise to new emission centers. As was shown in Ref. 2, on account of intense electronic currents the plasma in the region near the anode can be heated up to temperatures of the order of 1 keV. It is obvious that the spots in Figs. 3a and 5a correspond to the region near the anode. The x-ray generation described above in the form of point sources is also observed for other experimental conditions, for which the voltage on the gap varied from 150 V up to 2.7 kV, the gap width varied from 50 μm up to 150 μm, and the triggering time of the scan relative to the moment of ignition varied from 3 to 20 ns.

Besides the above-indicated mechanisms of generation of soft and hard x rays, which are caused by the ionization–overheating instability or plasma-erosion circuit-opening,[1–4] the following mechanism can also be considered. Strictly directed x-ray emission from spatially localized point sources can be explained by pinching in the cathode-flame plasma. As shown in the experiments of Ref. 3 on measurement of the electron density in the cathode spots of a laser-induced discharge, which were performed with high spatial (<1 μm) and temporal (100 ps) resolutions, the cathode-flame plasma consists of subfragments — plasma channels less than 5 μm in diameter with electron density $N_e > 5\times 10^{26}$ cm^{-3}. Numerical simulation[3] showed that the current density can increase for a short period of time of the order of 10–100 ps in such plasma-emission channels up to 10^{14} A/m^2. Such high current densities automatically result in pinching in the plasma — the appearance of hot spots. This phenomenon was observed in low-inductance vacuum spark discharges back in the 1970s[8] for discharge currents of the order of kiloamperes and voltages on the discharge capacitance greater than 30 kV. The experiments presented in the present work were performed with measured currents $I=1.3-3$ A, $U=150$ V, and we observed similar structures of the x-ray emission, indicating the possibility that micropinches appear in our low-voltage discharge also. A spontaneous increase of the current density up to the values indicated above gives rise

instantaneously to the generation of a magnetic field of the order 10^5–10^7 G in the plasma fragments. As long as the current density and correspondingly the magnetic field exceed the kinetic pressure in the plasma fragment, we can observe in the form of horizontal tracks in the streak photographs a contracted channel with x-ray generation.

There are some ''hot'' spots in the streak photographs (see, for example, Figs. 3a, 4a, 5a) that expand at a rate of the order of 3×10^3–10^4 m/s. As long as the magnetic pressure exceeds the kinetic plasma pressure (this happens for $B>140$ T and plasma temperatures of the order of 100 eV in the plasma channel), intense heating of the channel and micropinching should occur. When the kinetic pressure has increased to a value above the magnetic pressure, the channel undergoes radial expansion. The typical decay time of the channel can be estimated as $\tau\approx\Delta r/V_s$, where Δr (3 μm) is the radius of the contracted channel and V_s ($\approx10^4$ m/s) is the speed of sound in the plasma. Then we obtain $\tau\approx300$ ps, which is in agreement with experiment (see Figs. 4b, 5b).

Further experiments and the results of an accurate mathematical calculation using an electrohydrodynamic model will be presented in a separate paper.

In our experiments we detected a strictly directed x-ray emission from plasma sources of the order of 1 μm in size in the spectral range 0.1–10 keV in low-voltage laser-induced discharges at the arc stage. This allows us to assert that: 1) the temperature in the plasma subfragments of the cathode flame can reach values of the order of 100 eV and higher, which corresponds to accurate numerical calculations,[3] and 2) micropinching of plasma channels occurs up to diameters of the order of 1 μm.

I wish to express my appreciation to V. A. Skvortsov and T. I. Filippova for many discussions concerning this work and to N. Kochan for faultless technical support. This work was supported by the German Academy of Scientific Research Leopoldina.

[a)]e-mail: n.vogel@physik.tu-chemnitz.de

[1] V. A. Skvortsov and N. Vogel, in *Proceedings of an International Conference on the Physics of Stongly Coupled Plasmas*, Binz/Rugen, Germany, 1995, edited by W. D. Kraeft and M. Schlanges, World Scientific, Singapore, 1996, p. 343.
[2] V. A. Skvortsov and N. Vogel, in *Proceedings of the 11th International Conference on High Power Particle Beams*, BEAMs'96, Prague, 1996, Vol. I, p. 513.
[3] N. Vogel and V. A. Skvortsov, IEEE Trans. Plasma Sci. **PS-25**, 553 (1997).
[4] V. A. Skvortsov and N. I. Vogel, in *Proc. of the 24th Conference on Physics of High Temperature Plasmas and Confinement Fusion* [in Russian], Zvenigorod, 1997, p. 196.
[5] S. I. Petrov, V. P. Lazarchuk, V. M. Murugov *et al.*, in *Proceedings of the 22nd International Congress on High-Speed Photography and Photonics*, Santa Fe, New Mexico, USA, 27 October–1 November, 1996.
[6] B. Soom, R. Weber, and J. E. Balmer, J. Appl. Phys. **68**, 1392 (1990).
[7] G. A. Mesyats, *Ektons* [in Russian], Nauka, Ekaterinburg, 1994, Pt. 2, p. 72.
[8] C. R. Negus and N. J. Peacock, J. Phys. D: Appl. Phys. **12**, 91 (1979).

Translated by M. E. Alferieff

Generation and interaction of large-amplitude solitons

E. N. Pelinovskiĭ[a)]
Division of Nonlinear Waves, Institute of Applied Physics, Russian Academy of Sciences, 603600 Nizhniĭ Novgorod, Russia

A. V. Slyunyaev
Nizhegorod State University, 603600 Nizhniĭ Novgorod, Russia

(Submitted 19 March 1998)
Pis'ma Zh. Éksp. Teor. Fiz. **67**, No. 9, 628–633 (10 May 1998)

The results of a numerical simulation of the interaction and generation of solitons in nonlinear integrable systems which admit the existence of very-large-amplitude solitons are reported. The nonlinear integrable system chosen for study is the Gardner equation, particular examples of which are the Korteweg–de Vries equation (for quadratic nonlinearity) and a modified Korteweg–de Vries equation (for cubic nonlinearity). It is shown that during the evolution process solitons of opposite polarity appear on the crest of the maximum soliton. © *1998 American Institute of Physics.* [S0021-3640(98)00409-5]

PACS numbers: 03.40.Kf

The Korteweg–de Vries equation, discovered back in 1895 for waves on water, is the most popular model for describing nonlinear waves in weakly dispersive media. It has essentially become the first proving ground for demonstrating particle-like properties in the form of stable solitons for a nonlinear wave field and proving the integrability of an evolutionary problem by the method of the inverse problem of scattering theory, making it possible to prove the essential role of solitons in the asymptotic representation of a wave field at long times. The Korteweg–de Vries equation is obtained in first-order perturbation theory in the small amplitude of the wave and in the weak high-frequency dispersion. For this reason, it is applicable for describing diverse wave motions in the ocean and the atmosphere as well as in plasmas and in astrophysical objects. In its most general form it can be represented as

$$\frac{\partial u}{\partial t}+(c+\alpha u)\frac{\partial u}{\partial x}+\beta\frac{\partial^3 u}{\partial x^3}=0, \tag{1}$$

where c, α, and β are constants, determined by the specific nature of the physical problem. A modified Korteweg–de Vries equation is obtained in first-order perturbation theory:

$$\frac{\partial u}{\partial t}+(c+\alpha_1 u^2)\frac{\partial u}{\partial x}+\beta\frac{\partial^3 u}{\partial x^3}=0. \tag{2}$$

Such an equation has been obtained for electromagnetic surface waves in an electric field,[1] waves in size-quantized films,[2] internal waves in the ocean with a definite stratification,[3] and some other situations. The modified Korteweg–de Vries equation can also be solved exactly by the method of the inverse problem of scattering theory,[4] and here solitons and kinks (shocks) also determine the asymptotic representation of the wave field. If the quadratic nonlinearity is nonzero, then a cubic nonlinearity is obtained in the next order of perturbation theory and can be retained in the equation together with corrections of the next order in the dispersion, including also nonlinear dispersion (see, for example, Ref. 5). The study of equations of this type has virtually only just begun.[6] However, it is clear from general considerations that within the perturbation theory effects due to small higher-order corrections should be small and should not radically alter the soliton shape, for example. Meanwhile, in certain situations the coefficient of the quadratic nonlinearity can be small enough that the quadratic and cubic nonlinearities are of the same order of magnitude while at the same time the next orders in the dispersion can be neglected. The equation obtained in this manner is called the Gardner equation:

$$\frac{\partial u}{\partial t}+(c+\alpha u+\alpha_1 u^2)\frac{\partial u}{\partial x}+\beta\frac{\partial^3 u}{\partial x^3}=0. \tag{3}$$

Our objective in the present letter is to demonstrate new physical effects due to the generation and interaction of large-amplitude solitons when the quadratic and cubic nonlinearities are of the same order of magnitude.

Apparently, the Gardner equation (3) was first derived rigorously in an asymptotic theory for internal waves in a two-layer liquid with a density jump at the interface.[7,8] The corresponding expressions for the coefficients of this equation have the form (in the approximation of a small density jump)

$$c=\sqrt{\frac{\Delta\rho}{\rho}\frac{h_1h_2}{h_1+h_2}},\quad \beta=\frac{ch_1h_2}{6},\quad \alpha=\frac{3c}{2}\frac{h_1-h_2}{h_1h_2},$$

$$\alpha_1=-\frac{3c}{8h_1^2h_2^2}(h_1^2+h_2^2+6h_1h_2), \tag{4}$$

where u is the displacement of the interface, h_1 and h_2 are, respectively, the thicknesses of the top and bottom layers, $\Delta\rho/\rho$ is the relative magnitude of the density jump, and g is the acceleration of gravity. As one can see from Eq. (4), the coefficient of the quadratic nonlinearity can change sign (and this leads to interesting features of the transformation of a soliton in the case of an inclined interface; see Ref. 9), while the coefficient of the cubic nonlinearity is negative. Recently, the formulas for the coefficients in Eq. (3) were generalized for an arbitrary density stratification of the liquid[10] and it was shown that the coefficient of the cubic nonlinearity can have either sign.[3] If it is assumed that the depths of the layers are approximately equal to one another and the wave amplitude is small compared with the depth, then the quadratic and cubic nonlinearities can be regarded as small and comparable to one another ($\alpha u/c\sim\alpha_1u^2/c\ll 1$) as well as to the dispersion. Since both nonlinearities are then terms of the same order of magnitude (in the conventional perturbation schemes the cubic nonlinearity is always less than the quadratic nonlinearity), in this sense we can talk about waves of large amplitude (we note that in the

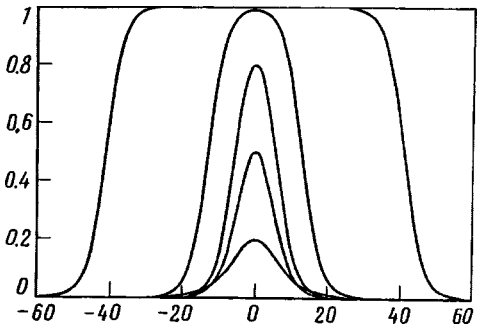

FIG. 1. Soliton shape for different amplitudes.

real world such waves in the ocean can reach large amplitudes of tens of meters). Here we shall consider the case when the coefficient of the cubic nonlinearity is negative, as for a two-layer liquid.

The one-soliton solution of the Gardner equation can easily be found in explicit form:

$$u(x,t)=\frac{6\beta\Gamma^2}{\alpha}\,\frac{1}{1+\sqrt{1+\dfrac{6\alpha_1\beta\Gamma^2}{\alpha^2}\cosh(\Gamma(x-Vt))}},\quad V=c+\beta\Gamma^2, \tag{5}$$

where Γ^{-1} is the effective width of the soliton. For small Γ the solution (5) describes a Korteweg–de Vries soliton with amplitude $A=3\beta\Gamma^2/\alpha$ (its polarity is determined by the sign of the coefficient of the quadratic nonlinearity), and as $\Gamma\to\alpha/(6|\alpha_1|\beta)^{1/2}$ the soliton acquires a rectangular shape (Fig. 1) with the limiting amplitude

$$A_{\lim}=\alpha/|\alpha_1|\,. \tag{6}$$

It is convenient (especially near the limiting soliton) to represent the one-soliton solution in the form of a kink–antikink combination:

$$u(x,t)=\frac{A_{\lim}}{2}(\tanh Z_+-\tanh Z_-),\quad Z_\pm=\frac{\alpha}{\sqrt{24|\alpha_1|\beta}}(x-Vt\pm\delta), \tag{7}$$

and then δ determines the width of the limiting soliton.

It should be noted first and foremost that the Miura transformation[8]

$$v=\frac{\alpha u+\alpha_1 u^2}{\sqrt{-6\alpha_1\beta}}+\frac{\partial u}{\partial x} \tag{8}$$

reduces Eq. (3) to the classical Korteweg–de Vries equation (1) and thereby proves that the Gardner equation is integrable by the method of the inverse problem of scattering theory[8,11] and therefore soliton collisions are elastic. Nonetheless, to ''reconstruct'' the

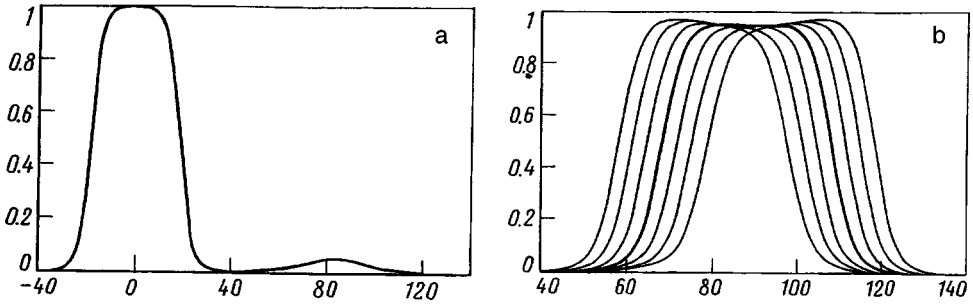

FIG. 2. Interaction of the limiting soliton with a small-amplitude soliton (amplitude ratio 1:20): a) initial distribution; b) at different times; the heavy line shows a symmetric distribution.

function $u(x,t)$ in terms of $v(x,t)$ requires solving the Ricatti equation (8), which cannot be solved in quadratures. At the same time, the simple change of variables

$$u = A_{\text{lim}}/2 + w \tag{9}$$

reduces the Gardner equation (3) to a modified Korteweg–de Vries equation (2) and makes it possible to use the known exact solutions of this equation. However, most known solutions of Eq. (2) refer to a zero pedestal and cannot be used to solve impulsive perturbations of the Gardner equation. For this reason, we solved Eq. (3) numerically in order to analyze the interaction and generation of large-amplitude solitons. In the calculations we set $c=0$, $\alpha=1$, $\alpha_1=-1$, and $\beta=1$.

INTERACTION OF SOLITONS

As expected, the interaction of solitons with amplitudes less than the limiting amplitude follows the well-known Korteweg–de Vries scenario: If the difference in the amplitudes is large, then the large soliton, having the higher velocity, simply overtakes the small soliton. However, if the difference in the velocities is small, then the trailing (large) soliton gives up energy to the leading (small) soliton and itself slows down, while the leading soliton accelerates (exchange of amplitudes between solitons). Such an exchange interaction is observed for two solitons with amplitudes close to the limiting level. The most interesting case is where the amplitude of one (trailing) soliton is close to the limit while the amplitude of the other (leading) soliton is ''normal'' (Fig. 2a). Even if the leading soliton is small, in the interaction process the ''combined'' wave does not exceed the threshold value (Fig. 2b), and the dip that is characteristic of an exchange interaction forms in it. The interaction process for closer values of the amplitudes is shown in Fig. 3 (amplitude ratio is 1.4). The small soliton interacts with the front slope of the limiting soliton (which moves more rapidly) and flips over at the summit, moves freely along the summit, and then slides down the trailing slope of the limiting soliton, restoring its initial polarity. The existence of a negative-polarity soliton on the summit of the limiting soliton can be understood from the Gardner equation (3): If the soliton is studied on a pedestal $u=A_{\text{lim}}$, then the solution will satisfy the same equation (3) but with a quadratic nonlinearity of opposite sign (in our case negative). This is what leads to the appearance of a negative-polarity soliton. At the same time it is clear from Fig. 3 that the small soliton interacts successively with each slope of the limiting soliton, each of which can be

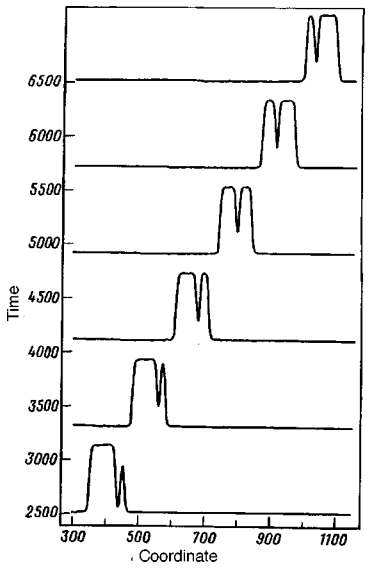

FIG. 3. Interaction of the limiting soliton with a large-amplitude soliton (amplitude ratio 1:1.4) at different times.

interpreted as a kink and antikink. The interaction of a soliton with a kink (antikink) ''in pure form'' has been analyzed previously for the modified Korteweg–de Vries equation,[1] to which Eq. (3) can be reduced by the substitution (9). A successive collision first with a kink and then with an antikink should restore the initial, experimentally observed, polarity of the soliton. Essentially, the dip in Fig. 2b can be interpreted as a negative-polarity soliton, though admittedly, because of its large width it is difficult to interpret the dip as being the result of an interaction of a soliton with a kink.

Thus the result of an interaction depends on the closeness of the total amplitude of the solitons to the limiting value. If this quantity does not exceed the limiting value, then the solitons interact without a change in their polarity, and here the overtaking (large difference in amplitudes) or exchange (close amplitudes) processes are observed. However, if the total amplitude is greater than the limiting value, then at the moment of a collision a dip appears against the background of the large wave, and at any moment in time the amplitude of the wave does exceed the limiting value. The interaction of a small soliton with a large one can be interpreted as a successive interaction of a soliton with each slope of the limiting soliton (kink and antikink) with a change in the polarity of the soliton at the intermediate stage.

DECAY OF AN INITIAL DISTURBANCE

An initial distrubance with amplitude less than the limiting value once again decays according to the Korteweg–de Vries scenario: A positive initial disturbance (in the calculations the initial shape was described by the hyperbolic secant function sech) decays into a group of solitons (or one soliton) and an oscillating tail. Interesting features arise in the case when an initial disturbance with initial amplitude greater than the limiting value decays (Fig. 4a). In this case two steep drops (quasi-shocks) arise at the first stage

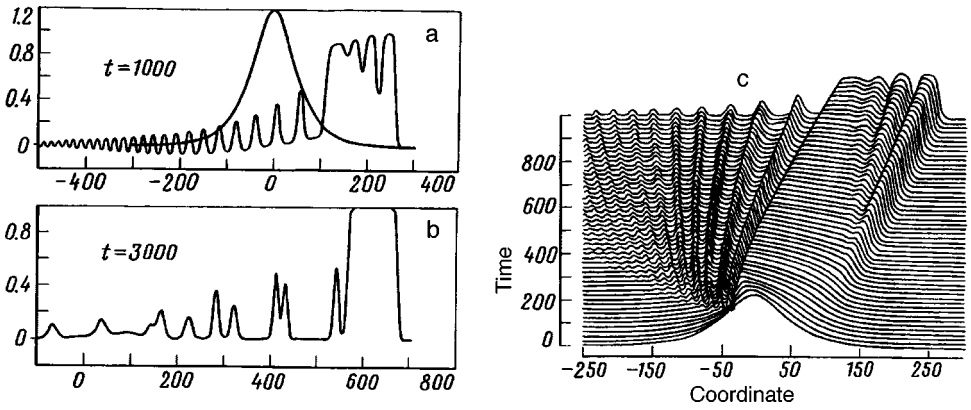

FIG. 4. Evolution of an initial disturbance with amplitude greater than the limiting value: a) $t=0$ (heavy line) and $t=1000$; b) $t=3000$; c) interaction dynamics.

on account of the cubic nonlinearity (in pure form relative to the level $A_{\text{lim}}/2$). Then, small-scale waves are generated at each drop, some of which transform into solitons with different polarity depending on the pedestal on which they are generated (Fig. 4a). Next, the negative solitons on the crest of the wave interact with an antikink and descend from the limiting soliton, changing polarity and superposing on the group of solitons which are formed together with the antikink (Fig. 4b). In the asymptotic limit one limiting soliton and a group of small-scale waves are formed. The broadening of an initial disturbance with an amplitude above the limiting value results in the formation of a wider limiting soliton. The formation of a limiting soliton has been predicted previously by the inverse problem of scattering theory,[12] but no analysis was made of the intermediate stage with the formation of solitons of different polarity.

Thus the existence of a limiting-amplitude soliton in integrable nonlinear systems leads to new effects in the interaction of solitons and the generation of solitons from initial disturbances, the main effect being that at an intermediate stage solitons (one or several) of opposite polarity form on the crest of the limiting soliton.

This work was supported in part by INTAS under Grant 95-969, the Russian Fund for Fundamental Research under Grants 96-05-64108 and 96-05-64111, and by the Ministry of Science under the program ''Nonlinear dynamics.'' We thank T. G. Talipova for participating in the development of the numerical program for solving the Gardner equation and in discussions of the results obtained.

[a)]e-mail: enpeli@appl.sci-nnov.ru

[1] T. L. Perel'man, A. Kh. Fridman, and M. M. Él'yashevich, Zh. Éksp. Teor. Fiz. **66**, 1316 (1974) [Sov. Phys. JETP **39**, 643 (1974)].
[2] E. P. Pelinovskiĭ and V. V. Sokolov, Izv. Vyssh. Uchebn. Zaved. Radiofiz. **19**, 536 (1976).
[3] R. Grimshaw, E. Pelinovsky, and T. Talipova, Preprint No. 97/29, Monash University (1997); Nonlinear Processes in Geophysics (in press).
[4] V. E. Zakharov, S. V. Manakov, S. P. Novikov, and L. P. Pitaevskiĭ, *Soliton Theory* [in Russian], Nauka, Moscow, 1980.

[5] T. R. Marchant and N. F. Smyth, J. Fluid Mech. **221**, 263 (1990).
[6] A. S. Fokas and Q. M. Liu, Phys. Rev. Lett. **77**, 2347 (1996).
[7] T. Kakutani and N. Yamasaki, J. Phys. Soc. Jpn. **45**, 674 (1978).
[8] J. W. Miles, Tellus **31**, 456 (1979).
[9] T. G. Talipova, E. N. Pelinovskiĭ, and R. Grimshaw, JETP Lett. **65**, 120 (1997).
[10] K. Lamb and L. Yan, J. Phys. Oceanogr. **26**, 2712 (1996).
[11] M. J. Ablowitz, D. J. Kaup, A. C. Newell, and H. Segur, Stud. Appl. Math. **53**, 249 (1974).
[12] J. W. Miles, Tellus **33**, 397 (1981).

Translated by M. E. Alferieff

Observation of extended poloidal structures in the turbulent edge plasma of the L-2M stellarator

G. M. Batanov, A. E. Petrov, K. A. Sarksyan, N. N. Skvortsova, O. I. Fedyanin, N. K. Kharchev, Yu. V. Khol'nov, and S. V. Shchepetov
Institute of General Physics, Russian Academy of Sciences, 117942 Moscow, Russia

C. Hidalgo, M. Pedrosa, B. van Milligen, and E. Sanchez
CIEMAT, 28040 Madrid, Spain

(Submitted 25 March 1998)
Pis'ma Zh. Éksp. Teor. Fiz. **67**, No. 9, 634–639 (10 May 1998)

Results are reported from an experimental study of the characteristics of the turbulent edge plasma in the L-2M stellarator. Extended coherent structures are observed to form in the poloidal direction. The poloidal coherence length of the fluctuations reaches 20 cm. The coherence of the fluctuations depends appreciably on the poloidal azimuth and is maximum along the outer edge, as is natural for unstable modes in a toroidal plasma. © *1998 American Institute of Physics.*
[S0021-3640(98)00509-X]

PACS numbers: 52.55.Hc, 52.25.Gj, 52.35.Ra

In the last few years the transport of particles under the influence of fluctuations in the edge plasma has been discussed as one of the processes that can affect global confinement in toroidal magnetic traps with different configurations of the magnetic fields.[1] It is important therefore to measure the characteristics of the plasma fluctuations. Both theoretical and experimental works devote special attention to the formation of correlated (or coherent[a)]) radial and poloidal structures, observed from measurements of the coherence lengths of the fluctuations detected.[2–4] The use of spectral analysis of fluctuation signals in terms of wave packets (wavelet analysis[b)]) has greatly extended the experimental possibilities,[5] making it possible to obtain information about the coherence of frequency wavelet components with high time resolution.[6] Such methods have been used to detect coherent radial and poloidal structures in the turbulent edge plasma in toroidal magnetic traps.[2,3] The structures do not exceed 1 cm in length. In the experiment whose results are reported in the present letter high coherence of plasma fluctuations at distances up to tens of centimeters in the poloidal direction was observed in the edge plasma of the L-2M stellarator. The observation of such extended coherent structures, encompassing a substantial portion of the minor perimeter of the plasma column, can in many ways change ideas about the processes occurring in the boundary plasma of stellarators and tokamaks.

The L-2M stellarator[7] is an $l=2$ machine. The major radius of the torus is $R=100$ cm and the average minor radius of the plasma is $\langle r\rangle=11.5$ cm. The plasma was produced and heated in a regime of electron-cyclotron resonance at the second harmonic

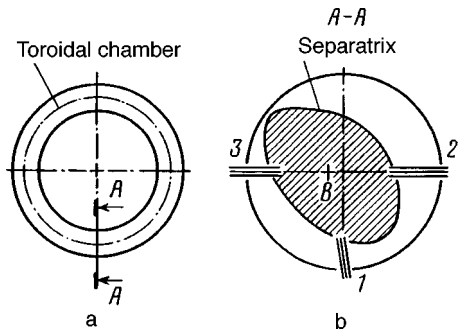

FIG. 1. Arrangement of the probe devices: a) top view of the toroidal chamber, b) poloidal section $A-A$; *1* — vertical probe, *2* — outer horizontal probe, *3* — inner horizontal probe; distances between probes $l_{12}\approx 20$ cm, $l_{13}\approx 15$ cm, $l_{23}\approx 35$ cm.

of the electron gyrofrequency (the magnetic field at the plasma center $B=1.3$–1.4 T) with gyrotronic-radiation power $P_0=150$–200 kW and heating pulse duration of up to 10 ms. The measurements were performed in plasma with average density $\langle n\rangle=(1.3$–$1.8)\times 10^{13}$ cm^{-3}, the electron temperature at center was $T_e(0)=400$–600 eV, and helium was used as the working gas. In the edge plasma at radius $r/r_s=0.9$ (r_s is the radius of the separatrix) the density is $n(r)=(1-2)\times 10^{12}$ cm^{-3}, the electron temperature is close to $T_e(r)=30$–40 eV, the relative level of the density fluctuations is $(\delta n/n)_{\text{out}}=0.2-0.25$ in the outer regions of the plasma and $(\delta n/n)_{\text{in}}=0.1$ in the inner regions.

The measurements were performed with three probe devices placed, as shown in Fig. 1, in the same poloidal plane of section (a minor section $A-A$ of the torus). Each probe device consisted of several individual cylindrical probes. The individual probes in a separate probe device were separated from one another by distances $l=4$–5 mm in the radial and poloidal directions, while the distance between the probe devices in the poloidal direction was equal to tens of centimeters (see Fig. 1). The probes detected plasma density fluctuations δn (ion saturation current I_s regime, $\delta I_s\sim\delta n$) and floating-potential fluctuations $\delta\phi$, and the radial fluctuation particle flux was calculated from these measurements.[3] Each probe device could be moved into the plasma by 1.5–2 cm from the separatrix.

Ordinarily, one probe device has been used in such experiments and only measurements of the coherence of the fluctuations at distances of several millimeters have been performed. For example, in Ref. 3 the coherence of plasma fluctuations at a distance $l=7$ mm in the radial and poloidal directions was recorded at frequencies ranging from several tens of kilohertz up to 300–400 kHz. It was also suggested there that unstable resistive magnetohydrodynamic (MHD) modes, associated with the presence of a magnetic bump in the system,[8] are responsible for the formation of such coherent structures.

The present experiment addressed a different problem: To determine whether or not coherence of fluctuations exists in the poloidal direction at large distances of up to tens of centimeters, covering a substantial portion of the minor perimeter of the plasma column. If so, then what is the difference in the coherence for the inner regions (close to the principal axis of the torus) and outer regions of the plasma? The latter question is im-

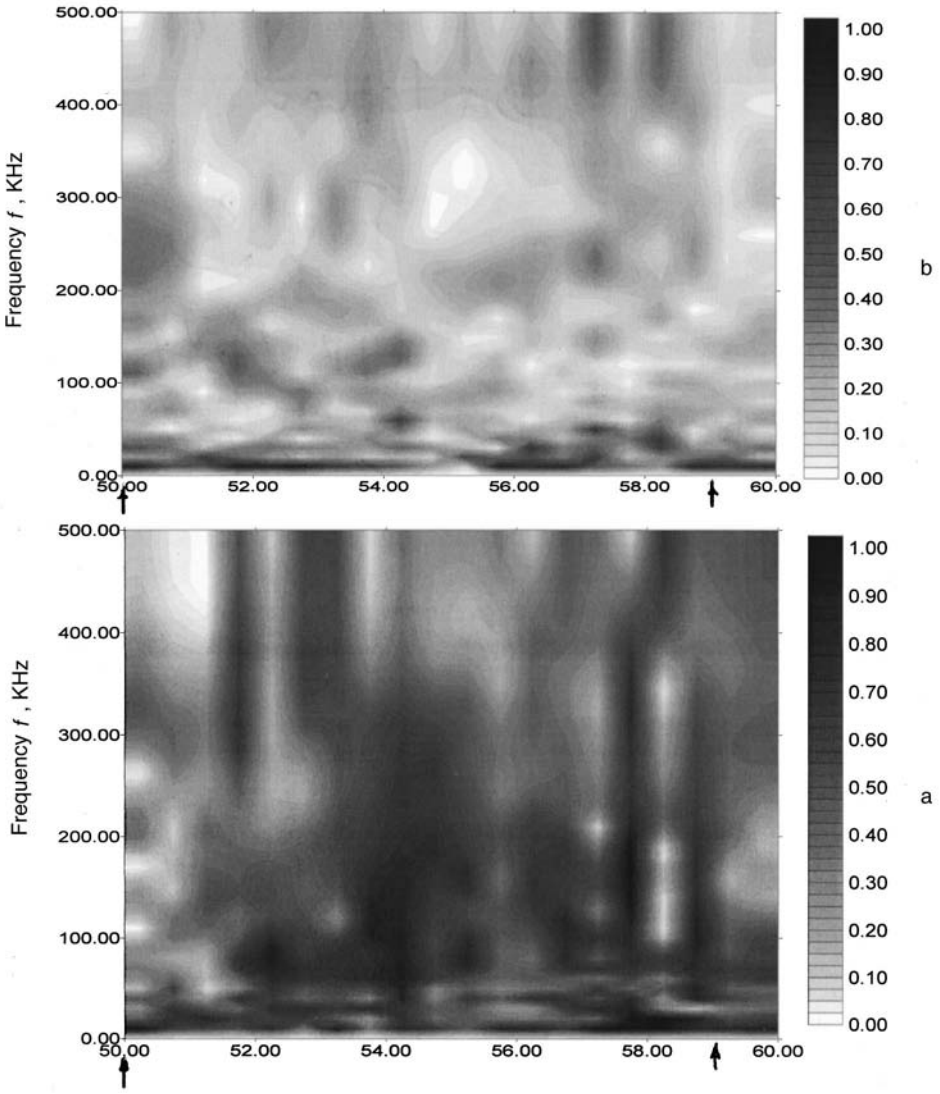

FIG. 2. Poloidal wavelet coherence of fluctuations of the ion saturation current between the vertical probe and the outer horizontal probe (a) and between the vertical probe and the inner horizontal probe (b). Position of the probes relative to the separatrix: $(r/r_s)_1 = 0.86$, $(r/r_s)_2 = 0.84$, $(r/r_s)_3 = 0.9$.

portant, since localization predominantly in outer regions of the plasma column is characteristic for unstable MHD modes in a toroidal geometry.[8]

We now turn to the measurement results. Figure 2 shows the mutual poloidal wavelet coherence of fluctuations of the ion saturation current between the vertical and outer horizontal probes (Fig. 2a) and between the vertical and inner horizontal probes (Fig. 2b). The real time in milliseconds is plotted along the abscissa (the arrows mark the start and end of the gyrotronic heating pulse) and the linear frequency in kilohertz is plotted along

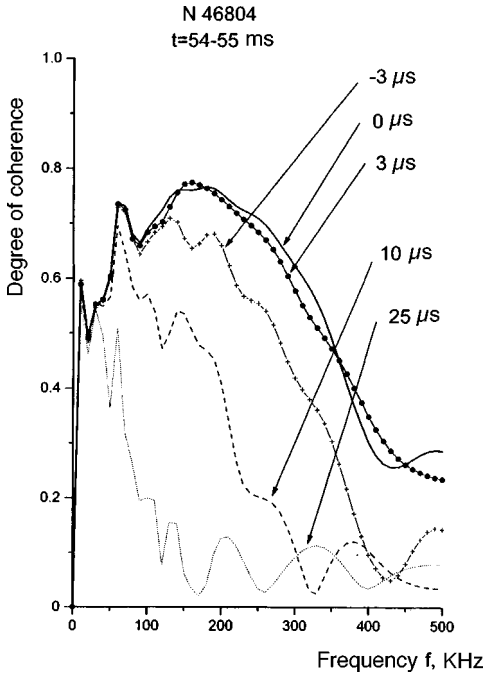

FIG. 3. Degree of wavelet coherence as a function of frequency at a fixed moment in real time. $t=54$–55 ms. Position of the probes relative to the separatrix: $(r/r_s)_1=0.86$, $(r/r_s)_2=0.84$.

the ordinate; the degree of mutual coherence of the frequency wavelet components of the fluctuation signals is designated by gray shading: from black (degree of coherence equal to 1) to white (degree of coherence equal to zero). We note that wavelet coherence was calculated for Fig. 2 with a time delay (Δ) between the signals of $t_\Delta=0$. The high poloidal coherence between fluctuations from the vertical and outer horizontal probes, separated by $l_{12}\approx 20$ cm, can be clearly traced in Fig. 2a. The degree of mutual coherence of the frequency wavelet components lies in the range from 0.4 to 0.9. At the same time the poloidal coherence of the fluctuation signals in the inner region of the plasma column (Fig. 2b) is several times lower. Therefore the coherence length of the fluctuation signals in the poloidal direction can be much greater than the lengths recorded thus far and can reach several tens of centimeters. The fact that coherence is localized predominantly in the outer regions of the plasma column is also obvious. This confirms indirectly the resistive ballooning nature of the observed unstable modes.

Helpful information about the direction of motion and velocity of fluctuations in coherent structures can be obtained by constructing a series of curves of the degree of mutual wavelet coherence as a function of frequency at fixed time but for different values of the delay time (or the correlation time) between the signals in both the positive and negative directions. Figure 3 displays such curves obtained for the real time interval from 54 to 55 ms with different delay (Δ) times $t_\Delta=0,\ \pm 3$, 10, and 25 μs. Wavelet coherence was calculated between the fluctuation signals from the vertical and outer horizontal probes. A comparison of the curves presented in Fig. 3 shows that for delay times up to $t_\Delta=10$ μs the degree of coherence decreases more strongly at relatively high frequencies

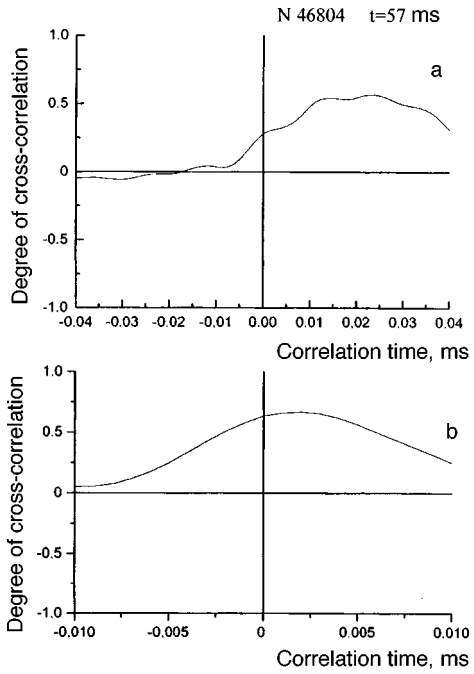

FIG. 4. Degree of cross-correlation versus correlation time between fluctuation signals of the floating potential: a — between the vertical and outer horizontal probes, $l_{12} \approx 20$ cm, b — between two individual probes of the vertical probe device, $l_{11} = 4-5$ mm, $t = 57-57.5$ ms. Position of the probes relative to the separatrix: $(r/r_s)_1 = 0.86$, $(r/r_s)_2 = 0.84$.

(>200 kHz), but for delay times $t_\Delta = 25$ μs the degree of coherence for all frequencies above the maximum resolvable frequency (i.e., $f > 50-70$ kHz) drops virtually to the background level ($\leqslant 0.2$). Hence it is not difficult to estimate the velocity of the coherent fluctuations in the poloidal direction. It is found to lie in the range $v_{\text{pol}} \approx (1-2) \times 10^6$ cm/s. From the fact that the degree of coherence decreases more strongly for negative delay times (see Fig. 3) it can be inferred that the poloidal velocity of the fluctuations is directed away from the vertical probe toward the outer probe, i.e., in the direction of the diamagnetic electron drift. Similar results also follow from the frequency-integrated spectrum of the dependences of the degree of cross-correlation on the correlation time between two fluctuation signals from probes which are spatially separated in the poloidal direction. Figure 4a shows such a dependence of the degree of cross-correlation obtained in the real time interval $t = 57-57.5$ ms between fluctuation signals of the floating potential from the vertical and outer horizontal probes ($l_{12} \approx 20$ cm). It is easy to verify from the position of the maximum of the degree of cross-correlation that the poloidal motion of correlated fluctuations is also directed away from the vertical probe to the outer horizontal probe, i.e., in the direction of the electronic diamagnetic drift, while the velocity lies in the interval $v_{\text{pol}} \approx (0.5-2) \times 10^6$ cm/s. For comparison Fig. 4b shows the degree of poloidal cross-correlation between the fluctuation signals of the floating potential but from two individual probes of only the vertical probe device, which, as indicated earlier, are separated by a short distance $l_{11} = 4-5$ mm. In this case the fluctuation motion is

directed in the direction of diamagnetic electron drift, while the velocity $v_{\rm pol} \approx 0.5 \times 10^6$ cm/s is close to the values presented above. Since the correlation dependences in Figs. 4a and 4b were obtained in the same shot, the fluctuations correlated in the poloidal direction are apparently identical at both the short distance $l_{11} = 4 - 5$ mm and the long distance $l_{12} \approx 20$ cm.

In summary, the experimental results reported in the present letter permit drawing the following conclusions:

1. A high degree of correlation of fluctuations at large distances in the poloidal direction was observed. This makes it possible to talk about the existence of a correlation length of up to $l_{\rm cor} = 20$ cm for fluctuations in the edge plasma of a stellarator.

2. The highly correlated fluctuations are localized predominantly in the outer region of the plasma column. This indirectly confirms that the fluctuations are of a resistive ballooning nature.

3. The poloidal velocity of the correlated fluctuations lies in the range $v_{\rm pol} \approx (0.5\text{–}2) \times 10^6$ cm/s.

4. The fluctuations correlated over short (4–5 mm) and long (20 cm) distances in the poloidal direction are identical.

In closing, we wish to express our sincere appreciation to the L-2M stellarator staff, who made this experiment possible.

This work was supported by the Russian Fund for Fundamental Research under Project No. 98-02-16345.

[a)]Coherence pertains to the frequency components of fluctuation signals, while correlation pertains to the signals themselves.

[b)]The direct transcription from the English term ''wavelet'' to the Russian was introduced as a scientific term in Ref. 5.

[1] C. Hidalgo, Plasma Phys. Controlled Fusion **37**, A53 (1995).
[2] C. Hidalgo, M. A. Pedrosa, B. van Milligen *et al.*, in *Proceedings of the 16th IAEA Fusion Energy Conference*, Montreal (1996), AP1-4.
[3] N. N. Skvortsova, G. Batanov, K. A. Sarksian *et al.*, J. Plasma Fusion Res. (JPFR Series, Vol. 1) (1998), in press.
[4] W. Horton, T. Tajima *et al.*, Comments Plasma Phys. Control. Fusion **17**, 205 (1996).
[5] N. M. Astaf'eva, Phys. Usp. **166**, 1145 (1996).
[6] C. Hidalgo, M. Pedrosa, B. Ph. van Milligen *et al.*, Phys. Plasmas **2**, 3017 (1996).
[7] V. V. Abrakov, D. K. Akulina, G. M. Batanov *et al.*, in *Proceedings of the 10th International Conference on Stellarators*; EUR-CIEMAT **30** (1995).
[8] L. M. Kovrizhnykh and S. V. Shchepetov, Fiz. Plazmy **7**, 419 (1981) [Sov. J. Plasma Phys. **7**, 229 (1981).

Translated by M. E. Alferieff

On nonquasineutrality and turbulent heat transfer in a tokamak

S. N. Gordienko

L. D. Landau Institute of Theoretical Physics, Russian Academy of Sciences, 142432 Chernogolovka, Moscow Region, Russia

É. I. Yurchenko

Kurchatov Institute Russian Science Center, 123182 Moscow, Russia

(Submitted 24 February 1998; resubmitted 1 April 1998)
Pis'ma Zh. Éksp. Teor. Fiz. **67**, No. 9, 640–645 (10 May 1998)

A new approach is proposed for describing a steady turbulent state formed far from thermodynamic equilibrium in the plasma column of a tokamak as a result of the development of microinstabilities. A fundamental feature of such a highly nonequilibrium plasma is its nonquasineutrality, i.e., the plasma properties are largely determined by electric fields localized on a scale of the order of the Debye radius. It is established that the transverse thermal diffusivity is determined by the expression

$$\chi_{\perp}(r)=\text{const}\,\frac{eU}{mc^2}\,\frac{q(r)}{2-S(r)}\,\frac{cT(r)}{eB},$$

where U is the voltage per orbit of the tokamak. The relation $n(r)q(r)=$ const and the increase in thermal diffusivity at the periphery of the plasma column can be explained on the basis of the proposed approach. © *1998 American Institute of Physics.*
[S0021-3640(98)00609-4]

PACS numbers: 52.55.Fa, 52.25.Kn, 52.35.Qz

The design of a tokamak-based thermonuclear reactor is now one of the most pressing applied problems in plasma physics. At the same time a number of very important physical processes occurring in a tokamak plasma are still not understood despite the progress that has been made. The difficulties in describing the plasma column stem from the fact that a tokamak plasma in the macroscopically stable state is not completely stable,[1] since a wide class of different kinetic instabilities can develop in it.

1. In the tokamak operating regimes of greatest interest conditions have been produced such that the plasma column is in a macroscopically stable state but microinstabilities can develop in the plasma column.[2]

The standard approach to describing microinstabilities is to linearize the kinetic equation about an equilibrium state and to investigate the linearized problem for the presence of perturbations that grow in time.[2] Unfortunately, this approach does not make it possible to describe the final result of the development of instabilities, i.e., to describe

the thermodynamically nonequilibrium turbulent steady state arising as a result of the stabilization of instabilities by nonlinear interactions. We note that to understand the physics of discharges in a tokamak it is not so much the linear instability that led to the steady nonequilibrium state that is of interest as it is to describe the actual state of the plasma with steady microturbulence.

In Ref. 3 a completely different approach was proposed to describe a turbulent steady state (developed microturbulence) of a plasma. Recall that plasma instabilities arise because the plasma is in a nonequilibrium state, i.e., because the entropy per particle differs by Δs from the entropy $s_{\max}$ in a thermodynamically equilibrium state. Since

$$s_{\max}=\int_0^T \frac{c_V}{T}dT,$$

the contribution to the integral from temperatures exceeding $e^2n^{1/3}$, where the specific heat of the plasma can be taken as $c_V=3/2$, can be estimated as $\ln N_D$, i.e., a large number of particles in the Debye sphere $N_D=(T/e^2n^{1/3})^{3/2}$ is a sufficient condition for nonequilibrium states to materialize in a high-temperature plasma with large Δs. In Ref. 3, to describe uniform isotropic steady microturbulence the long-time limit $t\to+\infty$ was studied after the limit $\exp(\Delta s)\to\infty$ was taken (the order in which the limits are taken is important!). Therefore it is supposed that a tokamak plasma is always in a state far from thermodynamic equilibrium. This does not contradict the *H* theorem, according to which the entropy increases monotonically with a characteristic time of the order of the collision time, since the *H* theorem is proved for a closed system, while in a tokamak power is fed to the plasma column and the energy flow can continually maintain the plasma in a highly nonequilibrium state. If the condition of strong plasma disequilibrium in one or another type of plasma installation does not match with the boundary conditions or the character of the heating, or if the theoretical predictions obtained from the condition contradict the experimental data, then the hypothesis that the turbulent steady state realized in the installation is a highly nonequilibrium state must be rejected and nonequilibrium steady states close to a thermodynamically equilibrium state must be considered.

Transport equations suitable for describing plasma far from equilibrium were obtained in Ref. 3, where it is shown that a nontrivial two-parameter Abelian group of transformations (group of turbulent dimensions[3]), transforming one solution of the equations into another, is associated with them. Analysis of the solutions that are invariant under a subgroup of this group identified by the condition $\lambda_2=\lambda_1^{D+1/2}$, where λ_1 and λ_2 are the parameters of the group of turbulent dimensions, shows that in a ''straight'' magnetic field in the presence of developed microturbulence

$$\exp(\Delta s)\gg 1 \tag{1}$$

there exists an entire one-parameter family of steady turbulent plasma states that can be parametrized by the parameter *D*. Dimensional considerations with respect to the standard physical dimensions (g, cm, s) and the new ''formal'' dimensions described by the group of turbulent dimensions[3,4] make it possible to show that for $D^2\ll 1$ the transverse thermal diffusivity and longitudinal conductivity are given by the expressions

$$\chi_\perp=C_1D^2\chi_{\text{Bohm}}+C_2\left(\frac{r_D}{\rho_e}\right)^2\chi_{\text{cl}}, \tag{2}$$

$$\frac{1}{\sigma_{\parallel}} = C_3 \frac{D^2}{\Omega_{ce}} + C_4 \frac{1}{\sigma_{\mathrm{Sp}}}, \tag{3}$$

and the energy density W of the fluctuation electric fields equals

$$\frac{W}{nT} = C_5 \frac{1}{N_D^{2/3}} + C_6 D^2 \left(\frac{r_D}{\rho_e} \right)^2, \tag{4}$$

where $\chi_{\mathrm{Bohm}} \sim T/B$ and $\chi_{\mathrm{cl}} \sim n/B^2\sqrt{T}$ are the Bohm and classical plasma thermal diffusivities, Ω_{ce} and $\sigma_{\mathrm{Sp}} \sim T^{3/2}$ are the cyclotron frequency and the Spitzer conductivity of the plasma, C_i, with $i = 1,2, \ldots 6$, are fixed numbers, and r_D and ρ_e are the Debye radius and the electron Larmor radius, respectively. Therefore, according to Eq. (4), the nonquasineutrality parameter D, which arises as a symmetry property, characterizes the magnitude of the electric-field fluctuations on a Debye scale, i.e., plasma nonquasineutrality effects (see details in Ref. 5).

2. In the analysis of homogeneous and isotropic developed microturbulence[3–5] the quantity D was treated as an independent parameter of the problem (as were n or T), and it indicated the type of turbulence materializing in the plasma. However, in a real tokamak D must be calculated on the basis of prescribed boundary and initial conditions and the regimes of energy supply and matter supply to the plasma column.

As will follow from the discussion below, only small D^2 are of interest in the case of a tokamak. In this case, however, the first term in Eqs. (2) and (3) is much larger than the second term, i.e.,

$$\frac{1}{N_D} \left(\frac{r_D}{\rho_e} \right)^2 \ll D^2 \ll 1. \tag{5}$$

Assuming that the entire plasma current flowing along the tokamak axis is of inductive origin, which is valid since $a/R \ll 1$, where a and R are the minor and major radii of the tokamak (and in all the equations below we retain only the terms that are of the first nonvanishing order in the parameter a/R, i.e., we neglect effects arising in higher orders), we obtain from Ohm's law

$$j = \sigma_{\parallel} E, \tag{6}$$

where E is the electric field that maintains the induced current in the tokamak.

Using Eqs. (3), (5), and (6) and the relation between the current density and the margin of stability $q(r)$, we find

$$D^2(r) = \frac{1}{C_3} \frac{eU}{mc^2} \frac{q(r)}{2 - S(r)}, \tag{7}$$

where $U = 2\pi RE$ is the voltage per orbit of the tokamak, while for the transverse thermal diffusivity we obtain, according to Eq. (2),

$$\chi_{\perp}(r) = \frac{C_1}{C_3} \frac{eU}{mc^2} \frac{q(r)}{2 - S(r)} \frac{cT(r)}{eB}, \tag{8}$$

where B is the toroidal magnetic field, $S(r)=rq'(r)/q(r)$ is the shear, $T(r)$ is the temperature at a distance r from the axis along the minor radius, $q(r)=rB/RB_\Theta(r)$, and $B_\Theta(r)$ is the poloidal magnetic field.

To obtain more detailed information about the radial dependence of the thermal diffusivity in the plasma column it is necessary to study the self-consistent distribution of the temperature and margin of stability. The following sections of this letter are devoted to this question.

3. First, we shall examine the question of finding $D(\mathbf{r})$ in a macroscopically stable plasma with prescribed $T(\mathbf{r})$ and $n(\mathbf{r})$. We note that the larger the value of the nonquasineutrality parameter D, the stronger will be the fluctuation electric fields developed in the plasma[5] and, hence, the stronger will be the correlations between the plasma particles, i.e., as D increases, the fraction of the phase volume accessible to the system decreases, as a result of which the entropy decreases, since D determines the amplitude of the collective (macroscopic) motions excited in the plasma, which are correlated on scales of the order of the Debye radius.

Thus, if the entire plasma is in a macroscopically stable state, then the requirement that the entropy density be maximum leads to the establishment of the smallest value of D that is compatible with the condition of macroscopic stability in a given volume. Therefore the requirement of hydrodynamic stability of the plasma makes it possible to calculate the nonquasineutrality parameter that arises because of the development of kinetic instabilities.

The principle of maximum energy density is not an arbitrary condition, but rather it follows from the dynamics of the plasma. If the system is ergodic, then the residence time τ_D of the system in a region $\Delta\Gamma_D$ of phase space with a fixed value of the nonquasineutrality parameter D is

$$\tau_D \sim \Delta\Gamma_D = \exp(Ns_D), \tag{9}$$

where s_D is the entropy per particle in the turbulent state of a plasma with nonquasineutrality parameter D, and N is the number of particles in the system.

The requirement that the entropy increase in the course of evolution makes it possible to describe in greater detail the process of transverse heat transfer in a plasma with a nonquasineutrality parameter satisfying Eq. (5). The smallness of D^2 makes it possible to neglect the dependence of the distribution functions on the nonquasineutrality parameter when calculating the entropy, taking the dependence on D^2 into account only in the transport coefficients. In this approximation, proceeding from Boltzmann's formula for the entropy of an ideal gas, which is applicable to a plasma with small D^2, we can write

$$S = \text{const} \int n(\mathbf{r}) \ln\left(\frac{T^{3/2}(\mathbf{r})}{n(\mathbf{r})}\right) dV, \tag{10}$$

and the requirement that for arbitrary initial conditions the system increases its entropy leads to the following expression for the transverse heat flux:

$$\mathbf{Q}_\perp = -C_1 D^2 \frac{nT}{B} \nabla_\perp T. \tag{11}$$

For the steady turbulent plasma states under study expression (11) does not contain a term proportional to $\nabla_\perp n$, since retaining such a term would result in a term proportional to $\nabla_\perp T \cdot \nabla_\perp n$ appearing in the expression for the entropy increase, which would also admit evolution with negative entropy production. The fact that $\nabla_\perp T$ and $\nabla_\perp n$ are perpendicular to the magnetic field was used in these last arguments, where it was assumed that $\nabla_\perp T$ and $\nabla_\perp n$ could be treated as independent quantities: In the absence of such a magnetic field, macroscopic motions will arise in the plasma to equalize the pressure, making ∇T and ∇n mutually dependent quantities. Moreover, for turbulent steady states there is no additional source of entropy production associated with the development of new instabilities that would be ''activated'' for any relationship between $\nabla_\perp T$ and $\nabla_\perp n$, since all possible electrostatic instabilities are already taken into account in the turbulent steady state.

4. The stability of the plasma column in a tokamak presumes, specifically, stability of the ballooning modes excited by the shear. It is well known that ballooning instabilities will dominate in experiments with large β and are therefore of special interest from the standpoint of obtaining a plasma with high energy content. The stability criterion for ballooning modes is[6,7]

$$\frac{1}{2}S^2+\alpha\epsilon\left(1-\frac{1}{q^2}\right)-\frac{1}{2}S\alpha^2>0, \tag{12}$$

where $\alpha=-8\pi p'(r)Rq^2(r)/B^2$ and $\epsilon=r/R$.

The maximum current density for which the inequality (12) is still satisfied corresponds to the minimum value of $D^2(r)$ ensuring stability of ballooning modes. Dropping the second term in Eq. (12) and analyzing all effects only in the first nonvanishing order in a/R, we easily see that the inequality (12) can be rewritten in the form

$$S=\alpha^2 \tag{13}$$

and can be regarded as a first-order differential equation by means of which $p(r)$ can be expressed in an elementary way in terms of $q(r)$. Using Eq. (2) but without the second term (because of Eqs. (5) and (11)) and taking into account the already established dependence of $p(r)$ on $q(r)$, for a fixed heat flux $Q(r)$ through a surface of radius r on account of the plasma heating mechanism, we obtain the temperature distribution over the plasma column in the form of a functional of $q(r)$. In this manner we obtain $n(r)$ and the entropy (see Eq. (10)) as functionals of $q(r)$. Varying the entropy for a fixed quantity of matter $2\pi\int_0^a n(r)r\,dr$ gives a nonlinear eigenvalue problem describing pinching of the plasma in a tokamak.

5. In the present letter we shall employ a simple variational method that leads to substantial simplifications and makes it possible to draw a correct picture of the structure of the discharge for a fortuitous choice of the trial function.

To describe discharges with a characteristic spatial scale r_0 ($r_0 \ll a$) we seek $q(r)$ in the form

$$q(r)=q_0(1+(r/r_0)^2), \tag{14}$$

i.e., as a function with the free parameters q_0 and r_0.

Moreover, to determine the structure of the discharge it is necessary to prescribe the function $Q(r)$. For definiteness, we take

$$Q(r)=Q_{\mathrm{Ohm}}(r)+Q_0, \quad Q_{\mathrm{Ohm}}(r)=4\pi^2 R\int_0^r Ej(r)r\,dr, \tag{15}$$

where $Q_0=\mathrm{const}$ is the radius-independent heat flux, which can be interpreted as the power introduced into the center of the plasma column by a neutral-injection beam, while $Q_{\mathrm{Ohm}}(r)$ is the Ohmic heating of the plasma.

Simple calculations following the scheme described at the end of the preceding section with the use of Eqs. (13)–(15) give for $r_0/a\ll 1$

$$p(r)\sim 1/r^3, \quad T(r)\sim 1/r, \quad n(r)\sim 1/r^2 \ \text{ for } r>r_0. \tag{16}$$

Moreover, for $Q_0=0$ and discharges described by expression (14)

$$n(r)q(r)=\mathrm{const}, \tag{17}$$

and for $Q_0\neq 0$ the relation (17) holds for $r>r_0$. Therefore, when the additional heating does not add too much to the Ohmic heating, the condition (17) can be expected to hold approximately for all r.

The finding that the product of the stability margin and the density is independent of the minor radius is actually in accord with experimental observations in the TEXT and TFTR tokamaks (see the review,[8] where an attempt is made to explain this on the basis of TPP-based theoretical arguments that are by no means uncontroversial, although the TPP formalism itself is entirely justified for a certain range of problems concerning magnetic traps[9]).

We find for the thermal diffusivity $\chi_\perp(r)$ at the periphery of the column, according to Eqs. (2) and (14),

$$\chi_\perp=C_1 D^2(r)\frac{cT(r)}{eB}\sim\left(\frac{r}{r_0}\right)^3, \quad r>r_0. \tag{18}$$

The increase in thermal diffusivity at the periphery of the plasma column is an experimentally reliably established and fundamentally important phenomenon[10] which still has no theoretical explanation. We note that earlier a thermal diffusivity that grows according to a cubic power law ($\chi\sim r^3$) at the periphery of the plasma was used successively to describe the experimental thermal diffusivities in the L regimes of the JET, D3-D, TFTR, JT-60U, PBX-M, and TORE SUPRA tokamaks.[11]

We express our sincere appreciation to V. D. Shafranov for calling our attention to the connection between turbulence and pinching and to S. I. Anisimov for his interest in this work and for a helpful discussion of the results.

This work was supported by the Russian Fund for Fundamental Research and the Council on Support for the Leading Scientific Schools under contracts 96-15-96448 and 96-15-96815.

[1] B. V. Kadomtsev, V. S. Mukhovatov, and V. D. Shafranov, Fiz. Plazmy **9**, 5 (1983) [Sov. J. Plasma Phys. **9**, 2 (1983)].
[2] A. B. Mikhaĭlovskiĭ, *Theory of Plasma Instabilities. Instabilities of Inhomogeneous Plasmas* [in Russian], Atomizdat, Moscow, 1977, Vol. 2.
[3] S. N. Gordienko, Fiz. Plazmy **23**, 754 (1997) [Plasma Phys. Rep. **23**, 698 (1997)].
[4] S. N. Gordienko, Fiz. Plazmy (1998), in press.
[5] S. N. Gordienko and É. I. Yurchenko, Fiz. Plazmy (1998), in press.
[6] O. P. Pogutse and É. I. Yurchenko, JETP Lett. **28**, 318 (1978).
[7] O. P. Pogutse and É. I. Yurchenko, *Reviews of Plasma Physics*, Vol. 11, edited by M. A. Leontovich, Consultants Bureau, New York, 1986 [Russian original, Atomizdat, Moscow, 1982].
[8] V. V. Yan'kov, Phys. Usp. **167**, 499 (1997).
[9] V. P. Pastukhov, Fiz. Plazmy **6**, 1003 (1980) [Sov. J. Plasma Phys. **6**, 549 (1980)].
[10] S. V. Mirnov, *Physical Processes in Tokamak Plasmas* [in Russian], Nauka, Moscow, 1983.
[11] Yu. V. Gott and É. I. Yurchenko, Fiz. Plazmy **20**, 853 (1996) [Plasma Phys. Rep. **20**, 769 (1996)].

Translated by M. E. Alferieff

New allotropic form of silicon

A. F. Khokhlov, A. I. Mashin,[a)] and D. A. Khokhlov
N. I. Lobachevskiĭ Nizhniĭ Novgorod State University, 603600 Nizhniĭ Novgorod, Russia

(Submitted 24 February 1998)
Pis'ma Zh. Éksp. Teor. Fiz. **67**, No. 9, 646–649 (10 May 1998)

A new allotropic form of amorphous silicon with sp hybridization of the valence electrons is discovered. The new material consists of linear chains of atoms. A small fraction of the atoms are in the sp^2 state. Acting as bridges, these atoms couple the linear chains into a single random network. This conclusion is based on an analysis of experimental data on the effect of annealing and ion implantation on the structure of the short-range order and the properties of amorphous-silicon films obtained by different methods. © *1998 American Institute of Physics.* [S0021-3640(98)00709-9]

PACS numbers: 81.05.Zx, 81.05.Cy, 81.40.Ef

It has long been known that carbon in the solid state can have three allotropic forms, differing in the hybridization of the valence electrons. One form is diamond, which can be regarded as a three-dimensional polymer of carbon with tetrahedral hybridization of the valence electrons (sp^3). Another form is the hexagonal graphite crystal, consisting of flat layers of carbon atoms in the sp^2 hybrid state. Finally, there is carbyne — a linear carbon polymer with sp hybridization of the valence electrons. The latter form has been observed in both the crystalline and amorphous states. The combination of carbon atoms with different valence modifications explains the entire diversity of carbon materials. Silicon atoms, just like carbon atoms, possess four valence electrons. However, the $3p$ orbitals are more prolate than the $2p$ orbitals, so that the difference of the sizes of the s and p valence orbitals in silicon is larger than in carbon, as a result of which when molecules are formed the overlap of the $3p$ orbitals in silicon is small, the π bond is weak, and therefore the probability of formation of bonds of the type Si=Si or Si≡Si is low. Despite this, silicon-containing gaseous compounds with stable multiple silicon–silicon bonds, such as tetramesityldisilene, disilene, and disilyne, are now known.[1,2] The main factor allowing for stabilization of these bonds is the large volume of the substitutents near the silicon. However, it has been believed that in the solid state crystalline and amorphous silicon both possess only sp^3-hybridized valence electrons.[3] Since 1991, we have been conducting an extensive study of the effect of annealing and ion implantation on the structure and properties of amorphous silicon obtained by different methods. Over this time we have accumulated quite a large amount of experimental data that cannot be explained by the presence of only the one tetrahedral form of silicon.

Amorphous silicon was obtained mainly by the decomposition of silane in a high-frequency glow discharge. Such amorphous silicon (*a*-Si:H) contains a high concentration of hydrogen. Depending on the production conditions, it varied from 12 to 40 at.%.

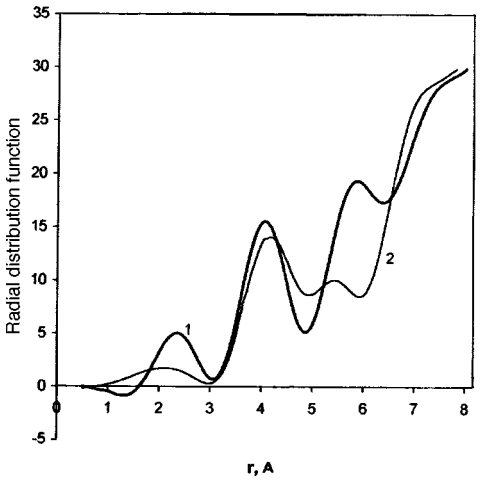

FIG. 1. Radial distribution function for *a*-Si:H films: Curve *1* — no annealing, *2* — annealing at 500 °C.

To obtain hydrogen-free amorphous silicon (*a*-Si) we employed vacuum sublimation of silicon and electron-beam evaporation.

Figure 1 shows electron diffraction data for *a*-Si:H films prepared at a substrate temperature of 250 °C. The film was deposited on a freshly cleaved face of a NaCl crystal. Thermal annealing was conducted at temperatures 350–700 °C. The annealing time was 30 min. Curves of the radial distribution of the electron density were calculated by the standard method proposed in Ref. 4, and information about the structure of the short-range order in amorphous silicon was obtained by analyzing the curves of the radial distribution, as was done in Ref. 5. According to curve *1*, the short-range order that is characteristic of crystalline silicon remains in the initial *a*-Si:H films. Disordering of the structure is manifested as a large change in the first and second coordination numbers ($k_1 = 3.8 \pm 0.2$, $k_2 = 11.3 \pm 0.9$), bond lengths (2.34 ± 0.04 Å), and the average angle between bonds ($\varphi = 112 \pm 6°$). The larger error in k_2 is due to the fact that the first coordination layer is isolated, while the second one combines two coordination spheres. As our investigations showed, the films remain amorphous up to annealing temperatures ~ 600 °C, while the strongest change in structure of the still amorphous film occurs at an annealing temperature of 500°C. The corresponding radial distribution function is also presented in Fig. 1 (curve *2*). Although, as we have said, the material remains amorphous after such treatment, its structure is completely different from that of the unannealed material or the material annealed at lower or higher temperature. The first coordination number in this case is close to 2 ($k_1 = 2.2 \pm 0.2$), while the average angle between bonds becomes close to 180° ($\varphi = 176 \pm 6°$). Another interesting fact is that the Si–Si interatomic distances here are shorter than in the crystal and are equal to 2.10 ± 0.04 Å, while the second coordination number $k_2 = 7.3 \pm 0.9$. We have also observed similar changes in the structure of the short-range order on annealing in *a*-Si:H films irradiated with neon and carbon ions as well as in films obtained at a substrate temperature of 50 °C. It is interesting to note that *a*-Si:H at 500 °C exhibits intense breaking of Si:H bonds and escape of hydrogen[6] from the film, giving rise to a sharp increase in the density of unpaired electrons. In the case of disordered amorphous silicon we observed this effect

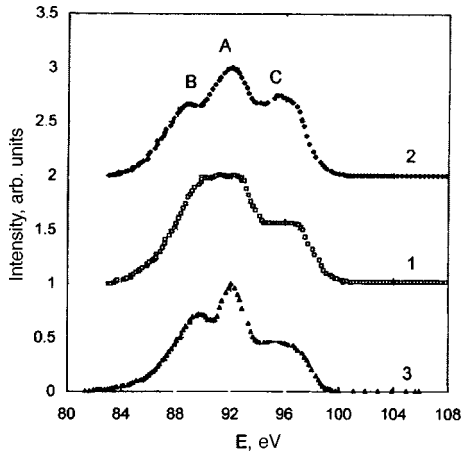

FIG. 2. Si $L_{2,3}$ emission spectra of *a*-Si:H (*1*, *2*) and crystalline silicon (*3*); curve *1* — annealing at 500 °C, curve *2* — no annealing.

only for films obtained by vacuum sublimation. According to Auger and ESR spectroscopy, such silicon contains a lower concentration of extraneous impurities[7] and a higher density of unpaired electrons[8] than do films of amorphous silicon deposited by other means.

The facts that k_1 decreases almost to 2 and the valence angle increases to 180 °C means that on the average each silicon atom now has not four but only two neighboring silicon atoms lying on the same straight line, i.e., the random network is formed from linear chains of atoms. The chain structure of silicon is also indicated by the almost halving of the second coordination number. Since the silicon atom is tetravalent, it should have multiple silicon–silicon bonds of the type Si–H or dangling bonds. In our view, the formation of linear cumulene $(=\mathrm{Si}=\mathrm{Si}=\mathrm{Si}=)_n$ or polyyne $(-\mathrm{Si}\equiv\mathrm{Si}-\mathrm{Si}\equiv\mathrm{Si}-)_n$ silicon chains is more likely. In the presence of a third Si–H bond or an unpaired (unshared) electron, according to the theory of repulsion of valence electron pairs,[3] the bond angle should be much less 180°. A value of k_1 somewhat greater than 2 indicates that some silicon atoms in the random network have three neighbors. These atoms, acting as bridges, connect linear chains into a single random network. Such a situation was observed in carbon in Ref. 9. Since silicon remains amorphous, we believe that the two forms of linear silicon chains coexist. An increase in the interaction forces between silicon atoms with a transition from a simple bond to a double and triple bond is accompanied, as in carbon,[3] by a decrease in the interatomic distance for all three types of silicon–silicon bonds. This can be judged according to the substantial shift and broadening of the first peak on the radial distribution curve (curve *2* in Fig. 1).

The experimental data which we obtained by ultrasoft x-ray spectroscopy[10,11] attest directly to a substantial difference in the electronic structure of amorphous silicon annealed at 500 °C from crystalline and unannealed amorphous silicon. Figure 2 displays the Si $L_{2,3}$ spectra on an energy scale relative to the $2p$ level. The valence band top lies approximately at 99.2 eV. As one can see from the figure (curve *2*), the distribution of valence electrons in the initial *a*-Si:H film obtained at 50 °C is similar to that observed by

other authors.[12] A wide principal maximum *A* corresponding to the 3*s* states of Si is observed in the energy region 90–92 eV, while in the direction of E_ν from this maximum a ''shoulder'' characterizing the protraction of the electron density of states is observed. After annealing at 500 °C (curve *1*) the main maximum in the density of states becomes more pronounced, while a second maximum *B* appears at low energies. A second maximum can also be seen in the spectrum of crystalline silicon (curve *3*), but its position and the relative intensity are different. Moreover, besides the ''shoulder'' there also appears a maximum *C* at 95.7 eV. A qualitatively similar situation is also characteristic for films which we obtained under other deposition conditions. Such a distribution of valence electrons has not been observed earlier either for silicon or its solid-phase compounds. The presence of a fine structure of the 3*s* states of Si in the form of two maxima *A* and *B* is due to the partial ordering of the atoms, while the energy gap between *A* and *B* is determined by the interatomic distance. For this reason, the increase in the gap by 0.4 eV compared with crystalline silicon is caused, according to Ref. 13, by a decrease in the interatomic distance by 0.2 Å. The maximum *C* which is uncharacteristic for Si attests to the presence of π bonds in this material and a change in the type of chemical bond between the atoms.

In summary, our experimental results attest to the existence of a new allotropic form of silicon with atoms in the *sp*-hybridized state. It can be called ''silicyne'' by analogy to carbyne. The transition of silicon into silicyne occurs in vacuum at temperatures of the order of 500 °C and is possible only under some additional conditions. In our view, there can be several such conditions.

The initial silicon must have a sufficiently low concentration of foreign impurities, such as oxygen and carbon. This can explain why silicyne is not formed from amorphous silicon obtained by electron-beam evaporation and a number of other methods.

Another condition is that at 500 °C there must be a high density of dangling bonds, which lead to a substantial change in the shape of the molecular orbitals.

There must exist a pressure which intensifies π bonds by increasing the degree of overlap of the 3*p* wave functions as the distance between the silicon atoms decreases. The pressure can be local. In our case it could be caused both by strong mechanical stresses, characteristic for thin deposited amorphous films of silicon, and by the presence of nonequilibrium densities of impurities or inert gases embedded by ion implantation. Cases when the structure of tetrahedral semiconductors changes under pressure are well known in the literature. For example, in Ref. 14 it is reported that silicon under a pressure of 200 kbar slowly assumes the structure of white tin.

[a)]e-mail: mashin@phys.unn.runnet.ru

[1]G. A. Razuvaev, T. N. Brevnova, and V. V. Semenov, Usp. Khim. **LV**, 1096 (1986).
[2]R. West, M. J. Fink, and J. Michl, Science **214**, 1343 (1981).
[3]A. F. Skryshevskiĭ, *Structural Analysis of Liquids and Amorphous Solids* [in Russian], Vysshaya shkola, Moscow, 1980, p. 328.
[4]B. K. Vaĭnshteĭn, Kristallografiya **2**, 29 (1957) [Sov. Phys. Crystallogr. **2**, 24 (1957)].
[5]V. N. Gordeev, A. I. Popov, and V. I. Filikov, Izv. Ross. Akad. Nauk Mater. **16**, 1733 (1980).
[6]W. Beyer, in *Tetrahedrally-Bonded Amorphous Semiconductors*, edited by D. Adler and H. Fritzsche, Plenum Press, New York, 1985, p. 129.

[7] A. F. Khokhlov, V. A. Sidorov, and A. I. Mashin, in *Proceedings of the 2nd Departmental Scientific-Technical Conference of Young Specialists* [in Russian], Moscow, 1980, p. 125.
[8] A. I. Mashin, Candidate's Dissertation, Gorki State University, Gorki, 1982, p. 214.
[9] F. Diederich, Nature **369**, 169 (1994).
[10] V. A. Terekhov, A. F. Khokhlov, N. S. Kovaleva *et al.*, Fiz. Tverd. Tela (St. Petersburg) **39**, 243 (1997) [Phys. Solid State **39**, 213 (1997)].
[11] A. F. Khokhlov, A. I. Mashin, and D. A. Khokhlov, *Sixteenth Scientific Lectures in Honor of Academician N. V. Belov* [in Russian], Nizhniĭ Novgorod, December 15–16, 1997, p. 17.
[12] É. P. Domashevskaya, I. Ya. Mittova, N. I. Ponomareva *et al.*, Poverkhnost', No. 6, 138 (1985).
[13] L. Ley, R. A. Pollak, S. P. Kowalzyk *et al.*, Phys. Rev. B **8**, 641 (1973).
[14] J. C. Jamieson, Science **139**, 762 (1963).

Translated by M. E. Alferieff

Nonlinear Seebeck effect in a model granular superconductor

S. A. Sergeenkov

Bogoliubov Laboratory of Theoretical Physics, Joint Institute for Nuclear Research, 141980 Dubna, Moscow Region, Russia

(Submitted 28 January 1998; resubmitted 20 March 1998)
Pis'ma Zh. Éksp. Teor. Fiz. **67**, No. 9, 650–654 (10 May 1998)

The change of the Josephson supercurrent density j_s of a weakly connected granular superconductor in response to externally applied arbitrary thermal gradient ∇T (nonlinear Seebeck effect) is considered within a model of 3D Josephson junction arrays. For $\nabla T > (\nabla T)_c$, where $(\nabla T)_c$ is estimated to be of the order of $\simeq 10^4$ K/m for YBCO ceramics with an average grain size $d \simeq 10$ μm, the weak-links-dominated thermopower S is predicted to become strongly ∇T-dependent. © *1998 American Institute of Physics.* [S0021-3640(98)00809-3]

PACS numbers: 74.80.Bj, 74.25.Bt

A linear Seebeck effect, observed in conventional and high-T_c ceramic superconductors (HTS) and attributed to their weak-link structure (see, e.g., Refs. 1–7 and further references therein), is based on the well-known fact that in a Josephson junction (JJ) the superconducting phase difference $\Delta\phi$ depends only on the supercurrent density j_s (according to the Josephson relation $j_s = j_c \sin \Delta\phi$, where j_c is the critical current density). When a rather small temperature gradient ∇T is applied to such a JJ (with a normal resistivity ρ_n), an entropy-carrying normal current with density $j_n = S_0 \nabla T/\rho_n$ is generated through the junction, where S_0 is the thermopower (the *linear* Seebeck coefficient). This normal current density is locally cancelled by a counterflow of supercurrent with density j_s, so that the total current density through the junction $j = j_n + j_s = 0$. As a result,[3] the supercurrent density $j_s = -j_n$ generates a nonzero phase difference $\Delta\phi$ via a transient Seebeck thermoelectric field $E_T = \rho_n j_n = S_0 \nabla T$ induced by the temperature gradient ∇T. If in addition, an external current of density j_e also passes through the weak link, a nonzero voltage will appear when the total current density exceeds j_c, i.e., for $j_e = j_c \pm S_0 \nabla T/\rho_n$.

In the present Letter, using a zero-temperature 3D model of Josephson junction arrays, a nonlinear analog of the thermoelectric effect (characterized by a nontrivial ∇T dependence of the Seebeck coefficient S) in granular superconductors is considered. The experimental conditions under which the predicted behavior of the thermopower can be observed in YBCO ceramics are discussed.

The so-called 3D model of Josephson junction arrays (which is often used for

simulating the thermodynamic behavior of a real granular superconductor) is based on the well-known tunneling Hamiltonian (see, e.g., Refs. 8–13)

$$\mathcal{H}(t)=\sum_{ij}^{N} J_{ij}[1-\cos\,\phi_{ij}(t)], \tag{1}$$

and describes a short-range interaction between N superconducting grains (with the gauge invariant phase difference $\phi_{ij}(t)$, see below), arranged in a 3D lattice with coordinates $\mathbf{r}_i=(x_i,y_i,z_i)$. The grains are separated by insulating boundaries producing a Josephson coupling J_{ij} which is assumed[8] to vary exponentially with the distance $\mathbf{r}_{ij}$ between neighboring grains, i.e., $J_{ij}(\mathbf{r}_{ij})=J(T)e^{-\boldsymbol{\kappa}\cdot\mathbf{r}_{ij}}$. For a periodic and isotropic arrangement of identical grains (with spacing d between the centers of adjacent grains), we have $\boldsymbol{\kappa}=(1/d,1/d,1/d)$. Thus d is of the order of an average grain (or junction) size.

In general, the gauge-invariant phase difference is defined as

$$\phi_{ij}(t)=\phi_{ij}(0)-A_{ij}(t), \tag{2}$$

where $\phi_{ij}(0)=\phi_i-\phi_j$, with ϕ_i being the phase of the superconducting order parameter, and $A_{ij}(t)$ is the so-called frustration parameter, defined as

$$A_{ij}(t)=\frac{2\pi}{\Phi_0}\int_i^j \mathbf{A}(\mathbf{r},t)\cdot d\mathbf{l}, \tag{3}$$

where $\mathbf{A}(\mathbf{r},t)$ is the (space–time dependent) electromagnetic vector potential; $\Phi_0=h/2e$ is the quantum of flux, with h Planck's constant, and e the electron charge.

As is known,[10,13] a constant electric field $\mathbf{E}$ applied to a single JJ causes a time evolution of the phase difference. In this particular case Eq. (2) reads $\phi_{ij}(t)=\phi_{ij}(0)+\omega_{ij}(\mathbf{E})t$, where $\omega_{ij}(\mathbf{E})=2e\mathbf{E}\cdot\mathbf{r}_{ij}/\hbar$, with $\mathbf{r}_{ij}=\mathbf{r}_i-\mathbf{r}_j$ being the distance between grains. If, in addition to the external electric field $\mathbf{E}$, the network of superconducting grains is under the influence of an applied magnetic field $\mathbf{H}$, the frustration parameter $A_{ij}(t)$ in Eq. (3) takes the form

$$A_{ij}(t)=\frac{\pi}{\Phi_0}(\mathbf{H}\wedge\mathbf{R}_{ij})\cdot\mathbf{r}_{ij}-\frac{2\pi}{\Phi_0}\mathbf{E}\cdot\mathbf{r}_{ij}t. \tag{4}$$

Here, $\mathbf{R}_{ij}=(\mathbf{r}_i+\mathbf{r}_j)/2$, and we have used the conventional relationship between the vector potential $\mathbf{A}$ and (i) a constant magnetic field $\mathbf{H}=\mathrm{curl}\,\mathbf{A}$ (with $\partial\mathbf{H}/\partial t=0$) and (ii) a uniform electric field $\mathbf{E}=-\partial\mathbf{A}/\partial t$ (with curl $\mathbf{E}=0$).

There are at least two ways to incorporate a thermal gradient (∇T) dependence into the above model. Namely, we can either invoke an analogy with the above-discussed influence of an applied electric field on the system of weakly coupled superconducting grains or assume a direct ∇T dependence of the phase difference (as was recently suggested by Guttman *et al.*[14]). For simplicity, in what follows we choose the first possibility and assume an analogy with the conventional Seebeck effect. Recall that application of a temperature gradient ∇T to a granular sample is known to produce a thermoelectric field[1,2] $\mathbf{E}_T=S_0\nabla T$, where S_0 is the so-called *linear* (∇T-*independent*) Seebeck coefficient. Assuming that $\mathbf{E}\equiv\mathbf{E}_T$ in Eq. (4), we arrive at the following change of the junction phase difference under the influence of an applied thermal gradient ∇T:

$$\phi_{ij}(t)=\phi_{ij}(0)-A_{ij}(t), \tag{5}$$

with the frustration parameter

$$A_{ij}(t)=\frac{\pi}{\Phi_0}(\mathbf{H}\wedge\mathbf{R}_{ij})\cdot\mathbf{r}_{ij}-\frac{2eS_0}{\hbar}\nabla T\cdot\mathbf{r}_{ij}t. \tag{6}$$

As we see, the above equation explicitly introduces a direct ∇T dependence into the phase difference, expressing thus the main feature of the so-called thermophase effect suggested by Guttman *et al.*[14] Physically, it means that the macroscopic normal thermoelectric voltage V couples to the phase difference across the junction through the quantum-mechanical Josephson relation $V\propto d\Delta\phi/dt$. Later on we shall obtain a rather simple connection between the thermophase coefficient $S_T\equiv d\Delta\phi/d\Delta T$ and the conventional linear Seebeck coefficient S_0.

To consider a nonlinear analog of the Seebeck effect (characterized by a ∇T-dependent thermopower S), we recall[10,13] that within the model under consideration the supercurrent density operator $\mathbf{j}_s$ is related to the pair polarization operator $\mathbf{p}$ as follows (V is the volume of the sample)

$$\mathbf{j}_s=\frac{1}{V}\frac{d\mathbf{p}}{dt}=\frac{1}{i\hbar V}[\mathbf{p},\mathcal{H}], \tag{7}$$

where the polarization operator itself reads

$$\mathbf{p}=\sum_i^N q_i\mathbf{r}_i\,. \tag{8}$$

Here $q_i=-2en_i$, with n_i the pair number operator, and r_i is the coordinate of the center of the grain.

Finally, in view of Eqs. (1)–(8), and taking into account the usual ''phase–number'' commutation relation $[\phi_i,n_j]=i\delta_{ij}$, we find

$$\langle\mathbf{j}_s(\nabla T)\rangle=\frac{2e}{\hbar d^3}\sum_{ij}^N\int_0^\tau\frac{dt}{\tau}\int_0^\infty\frac{d\mathbf{r}_{ij}}{V}J_{ij}(\mathbf{r}_{ij})\sin\,\phi_{ij}(t)\mathbf{r}_{ij} \tag{9}$$

for the thermal-gradient-induced value of the averaged supercurrent density. Here a temporal averaging (with a characteristic time τ) allows for a change of the phase coherence during tunneling of Cooper pairs through the barrier, and the integration over the relative grain positions $\mathbf{r}_{ij}$ is performed with allowance for the short-range character of the Josephson coupling energy, viz., $J_{ij}(\mathbf{r}_{ij})=J(T)f(x_{ij})f(y_{ij})f(z_{ij})$ with $f(u)=e^{-u/d}$.

To discuss the true ∇T-induced thermophase effect only, in what follows we completely ignore the effects due to a nonzero applied magnetic field (by putting $\mathbf{H}=0$ in Eq. (6)) as well as the ''self-field'' effects (which are rather important in granular superconductors; see Refs. 12 and 13 for a discussion of this problem) and we assume that in the equilibrium (initial) state (with $\nabla T=0$) $\langle\mathbf{j}_s\rangle\equiv 0$, which implies that $\phi_{ij}(0)\equiv 0$. The latter condition in fact coincides with the current density conservation requirement at zero temperature.[9] As a result, we find that an *arbitrary* temperature gradient $\nabla_x T\equiv\Delta T/\Delta x$ applied along the x axis to a Josephson junction network induces the appearance of the corresponding (nonlinear) longitudinal supercurrent with density

$$j_s(\Delta T)\equiv\langle j_s^x(\nabla_x T)\rangle = j_0 G(\Delta T/\Delta T_0), \tag{10}$$

where

$$G(z)=\frac{z}{(1+z^2)}. \tag{11}$$

Here, $j_0=2eJNd/\hbar V$, $(\nabla_x T)_0\equiv\Delta T_0/\Delta x=\hbar/2ed\tau S_0$, and $z=\Delta T/\Delta T_0$.

Notice that for a small enough temperature gradient (when $\nabla_x T\ll\nabla_x T_0$), we recover the conventional *linear* Seebeck dependence $j_s(\nabla_x T)=\alpha(T)S_0\nabla_x T$ with $\alpha(T)=(2ed/\hbar)^2 J(T)N\tau/V$. On the other hand, for this result to be consistent with the above-discussed conventional expression $j_s=S_0\nabla_x T/\rho_n$, the zero-temperature coefficient $\alpha(0)$ must be simply related to the resistivity ρ_n. Let us show that this is indeed the case. Using $J(0)=\hbar\Delta_0/4e^2R_n$ for the zero-temperature Josephson energy (where Δ_0 is the zero-temperature gap parameter), $V\simeq Nld^2$ for the sample volume (with l being a relevant dimension of the sample), and taking into account that the normal state resistance between grains R_n is related to ρ_n as $\rho_n\simeq(d^2/l)R_n$, the self-consistency condition $\alpha(0)=1/\rho_n$ yields $\tau\simeq(l/d)^2(\hbar/\Delta_0)$ for the characteristic Josephson time.

It follows from Eq. (10) that above some threshold value $(\nabla_x T)_c\simeq 0.25(\nabla_x T)_0$ the supercurrent density starts to deviate substantially from a linear law, thus suggesting the appearance of nonlinear Seebeck effect with a ∇T-dependent coefficient $S(\nabla_x T)=S_0/(1+z^2)$, where $z=\nabla_x T/(\nabla_x T)_0$ and $S_0\equiv S(0)$. Let us estimate the order of magnitude of this threshold value of the thermal gradient needed to observe the predicted nonlinear behavior of the thermopower in weak-links-containing HTS. Using $S_0\simeq 0.5\ \mu$V/K and $\Delta_0/k_B\simeq 90$ K for the thermopower and zero-temperature gap parameter in YBCO, and $l\simeq 0.5$ mm for a typical sample size,[2,4] we get $\tau\simeq 10^{-9}$ s for the characteristic Josephson tunneling time (cf. Ref. 13), and $(\nabla_x T)_c\simeq 10^4$ K/m for the threshold thermal gradient in a granular sample with an average grain (or junction) size $d\simeq 10\ \mu$m. Further, taking $J(0)\simeq\Delta_0$ for the zero-temperature Josephson energy (in samples with $R_n\simeq\hbar/4e^2$), we arrive at the following reasonable estimate of the weak-links-dominated critical current density in YBCO ceramics: $j_0=2eJ/\hbar ld\simeq 10^3$ A/m^2. We believe that the above estimates suggest quite an optimistic possibility of observing the discussed nonlinear behavior of the thermoelectric power in (real or artificially prepared) granular HTS materials and hope that the effects predicted in the present paper will be put to the test by experimentalists.

Let us conclude by obtaining a relation between the conventional (linear) Seebeck effect and the above-mentioned thermophase effect (which is linear by definition). According to Guttman *et al.*,[14] the latter effect is characterized by a nonzero transport coefficient $S_T=d\Delta\phi/d\Delta T$. In our particular case (with $\phi_{ij}(0)=0$ and $\mathbf{H}=0$), it follows from Eqs. (5) and (6) that

$$\Delta\phi\equiv\frac{1}{\tau}\int_0^\tau dt\sum_{ij}\frac{\phi_{ij}(t)}{N}\simeq\frac{e\tau S_0}{\hbar}\Delta T. \tag{12}$$

Hence, within our approach the above two ∇T-induced *linear* effects (characterized by the transport coefficients S_T and S_0, respectively) are related to each other as

$$S_T \simeq \left(\frac{e\tau}{\hbar}\right) S_0 \simeq \left(\frac{e}{\Delta_0}\right)\left(\frac{l}{d}\right)^2 S_0 . \tag{13}$$

To summarize, the change of the Josephson supercurrent density of a granular superconductor under the influence of an arbitrary thermal gradient (a nonlinear Seebeck effect) was considered within a model of 3D Josephson junction arrays. The possibility of experimental observation of the predicted effect in HTS ceramics was discussed.

[1] R. P. Huebener, A. V. Ustinov, and V. K. Kaplunenko, Phys. Rev. B **42**, 4831 (1990).
[2] A. V. Ustinov, M. Hartman, and R. P. Huebener, Europhys. Lett. **13**, 175 (1990).
[3] A. V. Ustinov, M. Hartman, R. P. Huebener *et al.*, Supercond. Sci. Technol. **4**, S400 (1991).
[4] R. Doyle and V. Gridin, Phys. Rev. B **45**, 10797 (1992).
[5] R. Doyle and V. Gridin, Europhys. Lett. **19**, 423 (1992).
[6] D. J. van Harlingen, Physica B **109–110**, 1710 (1982).
[7] G. I. Panaitov, V. V. Ryazanov, A. V. Ustinov *et al.*, Phys. Lett. A **100**, 301 (1984).
[8] B. Mühlschlegel and D. L. Mills, Phys. Rev. B **29**, 159 (1984).
[9] C. Ebner and D. Stroud, Phys. Rev. B **31**, 165 (1985).
[10] C. Lebeau, J. Rosenblatt, A. Robotou *et al.*, Europhys. Lett. **1**, 313 (1986).
[11] V. M. Vinokur, L. B. Ioffe, A. I. Larkin, and M. V. Feĭgel'man, Zh. Éksp. Teor. Fiz. **93**, 343 (1987) [Sov. Phys. JETP **66**, 198 (1987)].
[12] L. Leylekian, M. Ocio, L. A. Gurevich, and M. V. Feĭgel'man, Zh. Éksp. Teor. Fiz. **112**, 2079 (1997) [JETP **85**, 1138 (1997)].
[13] S. Sergeenkov, J. Phys. I France **7**, 1175 (1997).
[14] G. D. Guttman, B. Nathanson, E. Ben-Jacob *et al.*, Phys. Rev. B **55**, 12691 (1997).

Published in English in the original Russian journal. Edited by Steve Torstveit.

Giant burst of photoconductivity in semiconductors upon an increase in the concentration of recombination centers

V. A. Kholodnov[a)]
Theoretical Division, Orion Russian Science Center, 111123 Moscow, Russia

(Submitted 24 October 1997; resubmitted 23 March 1998)
Pis'ma Zh. Éksp. Teor. Fiz. **67**, No. 9, 655–660 (10 May 1998)

It is shown in the approximation of a single recombination level that the intrinsic photoconductivity of semiconductors with extrinsic recombination of carriers can increase by several orders of magnitude upon an increase in the concentration of recombination centers in the presence of weak optical radiation. © *1998 American Institute of Physics.* [S0021-3640(98)00909-8]

PACS numbers: 72.40.+w, 72.20.Jv

The copious information now available on the intrinsic photoconductivity of semiconductors with extrinsic recombination does not contain a clear picture of the nature of the dependence of the photocurrent density $I_{\rm ph}$ on the concentration N of recombination centers. This could be because of its apparent obviousness: $I_{\rm ph}$ should decrease with increasing N. Indeed, at first glance it does appear obvious that as N increases, the resulting increase in the rate of trapping of nonequilibrium electrons and holes will cause their lifetimes τ_n and τ_p to be shorter, and therefore $I_{\rm ph}$ will decrease. In this letter it is shown that this seemingly physically reasonable idea is not always correct: The curve $I_{\rm ph}(N)$, which on the whole descends with increasing N, can also contain an ascending region and can even increase by several orders of magnitude (Fig. 1a). The effect is due, first and foremost, to the fact that the times τ_n and τ_p grow extremely strongly (by orders of magnitude) in some range of values as N increases (Fig. 1b), if[1,2]

$$\xi_1 \equiv \frac{3}{\theta B} \ll 1, \quad \xi_2 \equiv \frac{4B}{A^2} \ll 1, \quad \xi_3 \equiv \frac{1}{\sqrt{A}} \ll 1, \quad \xi_4 \equiv \frac{\sqrt{B}}{A} \ll 1, \tag{1}$$

where

$$A = 2\frac{N_D}{n_t}, \quad B = 4\frac{p_t}{n_t}, \quad \theta = \frac{w_p}{w_n}, \tag{2}$$

w_n and w_p are the probabilities of trapping of electrons and holes in a deep level and n_t and p_t are equilibrium electron and hole densities when the energies of the Fermi level and the recombination level are equal to one another. References 1 and 2 employed a model based on the presence of completely ionized shallow donors with a concentration N_D and of neutral and singly charged negative deep acceptors with densities N_0 and $N_- = N - N_0$ with a small deviation (for example, due to weak illumination) of the pa-

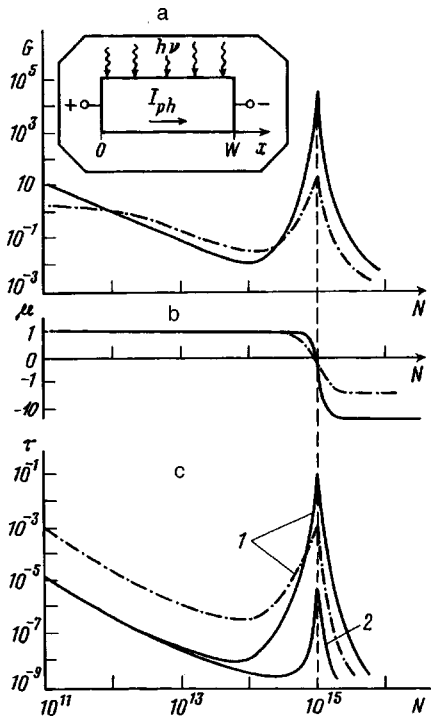

FIG. 1. The dependence on N (in cm^{-3}) of: a — $G \equiv I_{\mathrm{ph}}/qgW$; b — μ (in units of μ_p); c — τ_n (curve *1*) and τ_p (curve *2*) (in s). Room temperature, $W = 10^{-1}$ cm, $\theta \equiv w_p/w_n = 10^2$, $w_n = 10^{-8}$ cm^3/s, $n_i/n_t = 10^4$, $N_D = 10^{15}$ cm^{-3}, $E_0 = 10$ V/cm; the solid curve is for GaAs, the dot-dash curve for Si. The inset shows a diagram of the photoconductor.

rameters of the semiconductor from the equilibrium values. It has also been assumed[3,4] that the spin-degeneracy factor of an acceptor state equals 1/2. The same model is used in the present letter.

It follows from Refs. 5 and 6 that under the conditions of interband recombination of nonequilibrium carriers I_{ph} grows with increasing lifetime if the ambipolar mobility $\mu = 0$ or if there is no recombination at the current contacts ($x = 0$ and $x = W$, inset in Fig. 1a). In reality, however, recombination always occurs to one degree or another.[7] For this reason, under ordinary conditions ($\mu \neq 0$) an increase in the lifetimes, starting from certain values, does not result in a higher photocurrent.[5–7] Saturation of I_{ph} is most pronounced in the case of strong recombination at the contacts, in which case[5–7]

$$\Delta n(0) = \Delta p(0) = \Delta n(W) = \Delta p(W) = 0, \tag{3}$$

where $\Delta n(x)$ and $\Delta p(x)$ are, respectively, the deviations of the electron and hole densities from the equilibrium values n_e and p_e. Under extrinsic recombination conditions, as is shown below, the function $\mu(N)$ can vanish at the same value $N \cong N_D$ at which the functions $\tau_n(N)$ and $\tau_p(N)$ reach a maximum (Figs. 1b and 1c).[1,2] Therefore when N approaches N_D, I_{ph} increases to the extent that τ_n and τ_p increase, provided, of course, that the increase in the effective ambipolar diffusion length L_{eff} (see below) does not

result in a strong increase in the loss of photoexcited carriers due to diffusion toward the current contacts and recombination there. This is the physical reason for the effect.

The effect is most easily described mathematically if the neutrality equation for a nondegenerate semiconductor in a state of thermodynamic equilibrium is represented in the form

$$N = n_t \frac{1+\delta}{2\delta^2} f(\delta), \quad \delta = \frac{N_-^e}{N_0^e}, \quad f(\delta) = B + A\delta - \delta^2, \tag{4}$$

and the small parameter

$$\xi \equiv \frac{a_n + a_p}{\mu_n n_e + \mu_p p_e} = \frac{2(a_n + a_p)\delta}{(\delta^2 \mu_n + B\mu_p) n_t} \ll 1, \tag{5}$$

which can be used to characterize the degree to which the semiconductor deviates from local neutrality under illumination, is used. Here N_-^e and N_0^e are the equilibrium values of N_- and N_0, μ_n and μ_p are the electron and hole mobilities,

$$a_n = \frac{\varepsilon}{8\pi q} \frac{(1+\delta)\cdot f(\delta) w_p n_t}{\theta \cdot f(\delta) + (1+\delta)(\theta B + \delta)}, \quad a_p = \frac{\varepsilon}{8\pi q} \frac{(1+\delta^{-1})\cdot f(\delta) w_p n_t}{B + (A+\theta B)\delta + (\theta B + \delta)\delta^2}, \tag{6}$$

ε is the permittivity, and q is the electron charge. For weak illumination the linear approximation in g, where g is the density of the carrier photogeneration rate, is valid. From the linearized Poisson equations, the expressions for the dark hole and electron recombination–generation rates[2] R_p and R_n, respectively, and the condition of a steady state ($R_n = R_p$) it follows that in this approximation

$$R_n = \frac{\Delta n}{\tau_n} + a_n \frac{d\Delta E}{dx}, \quad R_p = \frac{\Delta p}{\tau_p} - a_p \frac{d\Delta E}{dx}, \quad \Delta p = \frac{\tau_p}{\tau_n}\Delta n + (a_n + a_p)\tau_p \frac{d\Delta E}{dx}, \tag{7}$$

where

$$\tau_n = \frac{2\delta^2}{f(\delta)} \frac{\theta \cdot f(\delta) + (1+\delta)(\theta B + \delta)}{[\delta A + (2+\delta)B + \delta^3] w_p n_t}, \quad \tau_p = \frac{2\delta}{f(\delta)} \frac{B + (A+\theta B)\delta + (\theta B + \delta)\delta^2}{[\delta A + (2+\delta)B + \delta^3] w_p n_t}, \tag{8}$$

ΔE is the deviation of the electric field from its value E_0 in the absence of illumination. Using the linearized expressions for the electron ΔI_n and hole ΔI_p components of I_{ph}, one can represent relations (7) as

$$R_n = \frac{\Delta n}{\tau_n} - \xi_n \frac{dj}{dx}, \quad R_p = \frac{\Delta p}{\tau_p} + \xi_p \frac{dj}{dx}, \quad \Delta p = \frac{\tau_p}{\tau_n}\Delta n - \xi \tau_p \frac{dj}{dx}, \tag{9}$$

where

$$j = (\mu_n \Delta n + \mu_p \Delta p) E_0 + D_n \frac{d\Delta n}{dx} - D_p \frac{d\Delta p}{dx}, \tag{10}$$

$$\xi_n = \frac{a_n}{\mu_n n_e + \mu_p p_e} < \xi, \quad \xi_p = \xi - \xi_n < \xi, \tag{11}$$

D_n and D_p are the electron and hole diffusion coefficients. In the absence of an external load (inset in Fig. 1a) illumination does not change the voltage across the sample. Therefore the expressions for ΔI_n and ΔI_p and Eqs. (9)–(11) with the boundary conditions (3) make it possible to write the photocurrent density as

$$I_{\rm ph}=\left\{\left(b+\frac{\tau_p}{\tau_n}\right)\cdot\langle\Delta n\rangle+\xi\frac{L_p^2}{W}\left(\frac{d\Delta p}{dx}-b\frac{d\Delta n}{dx}\right)\right|_{x=0}^{x=W}\Bigg\}q\mu_pE_0, \tag{12}$$

where $\langle\Delta n\rangle$ is the arithmetic-mean value with respect to x (inset in Fig. 1a) of the nonequilibrium electron density, $b=\mu_n/\mu_p$, and $L_p=(D_p\tau_p)^{1/2}$ is the hole diffusion length. The distribution $\Delta n(x)$ with $g(x)=$ const is itself determined by the equation

$$Q\frac{\partial^4\Delta n}{dx^4}-(D+D_E+D_\xi)\frac{d^2\Delta n}{dx^2}+(\mu+\mu_\xi)E_0\frac{d\Delta n}{dx}+\frac{\Delta n}{\tau_n}=g, \tag{13}$$

which can be obtained by using in addition the continuity equation for ΔI_n. Here

$$D_E=\xi\tau_p\mu_p\mu_nE_0^2,\quad D=\frac{\delta^2\tau_p+B\tau_n}{(B+b\delta^2)\tau_n}D_n,\quad \mu=\frac{n_e\tau_p-p_e\tau_n}{(p_e+bn_e)\tau_n}\mu_n=\frac{\delta^2\tau_p-B\tau_n}{(B+b\delta^2)\tau_n}\mu_n, \tag{14}$$

$$Q=\xi D_nL_p^2,\quad D_\xi=\xi_p\frac{\tau_p}{\tau_n}D_p+\xi_nD_n,\quad \mu_\xi=\xi_p\frac{\tau_p}{\tau_n}\mu_p-\xi_n\mu_n. \tag{15}$$

The quantities D and μ are the ambipolar diffusion coefficient and carrier mobility, respectively, in the quasineutral semiconductor plasma[3,5–9] (for sufficiently small ξ, as one can see from Eqs. (9) and (13)–(15)). The quantities Q, D_ξ, μ_ξ, and D_E are due to the photoexcitation of the space charge. Analysis shows that the condition (5), which usually holds with a large margin, makes it possible to drop in Eq. (13) terms with Q, D_ξ, and μ_ξ. However, the term with D_E must be retained, because even in moderate fields D_E can exceed D on account of the quadratic dependence on E_0. In the same way, the terms containing the small parameter ξ can be dropped in Eq. (12). Thus we arrive at the relations

$$(D+D_E)\frac{d^2\Delta n}{dx^2}-\mu E_0\frac{d\Delta n}{dx}-\frac{\Delta n}{\tau_n}+g=0,\quad I_{\rm ph}=q\left(\mu_n+\frac{\tau_p}{\tau_n}\mu_p\right)\cdot\langle\Delta n\rangle E_0. \tag{16}$$

Together with expressions (4)–(6), (8), and (14) they make it possible to obtain easily the function $I_{\rm ph}(N)$ in a parametric form (Fig. 1a).

Analyzing expressions (4), (8), and (14), one can show that the equation $\mu(N)=0$ has a solution when the inequalities (1) hold. To zeroth order in the small parameter (1) the root of this equation is identical to the positions of the maxima[1,2] of the functions $\tau_n(N)$ and $\tau_p(N)$ and equals N_D, a finding which we reported at an international symposium.[10] Let us explain the dependences of τ_n, τ_p, and μ on N, shown in Figs. 1b,c.

The reciprocals of the lifetimes of the nonequilibrium electrons and holes

$$\tau_n^{-1}=\tau_{n1}^{-1}+\tau_{n2}^{-1}+\tau_{n3}^{-1},\quad \tau_p^{-1}=\tau_{p1}^{-1}+\tau_{p2}^{-1}+\tau_{p3}^{-1} \tag{17}$$

consist of three partial components.[1,2] The first components, τ_{n1}^{-1} and τ_{p1}^{-1}, are responsible for the change in the electron and hole trapping rates $\Delta n \cdot w_n N_0^e$ and $\Delta p \cdot w_p N_-^e$, respectively, as a result of only a deviation of the carrier density from equilibrium values. The second components, τ_{n2}^{-1} and τ_{p2}^{-1}, are responsible for the change in the electron and hole trapping rates $n_e w_n \cdot \Delta N_0$ and $p_e w_p \cdot \Delta N_-$, respectively, as a result of only a deviation of the densities of the trapping centers $\Delta N_0 = N_0 - N_0^e$ and $\Delta N_1 = N_- - N_-^e = -\Delta N_0$ for electrons and holes, respectively, from the equilibrium values N_0^e and N_-^e. The third components, $\tau_{n3}^{-1} = \delta^{-1}\tau_{n2}^{-1}$ and $\tau_{p3}^{-1} = \delta\tau_{p2}^{-1}$, are responsible for the change in the rates of thermal excitation of electrons from an impurity level into the conduction band $\frac{1}{2}n_t w_n \Delta N_-$ and holes into the valence band $2p_t w_p \Delta N_0$ as a result of deviations ΔN_- and ΔN_0 of the densities of centers of thermal generation of electrons and holes, respectively, from the equilibrium values. The times τ_{n1} and τ_{p1} can be regarded as the trapping times of excess electrons and holes on equilibrium traps, the times τ_{n2} and τ_{p2} can be regarded as relaxation times of a nonequilibrium state as a result of trapping of equilibrium carriers on nonequilibrium traps, and the times $-\tau_{n3}$ and $-\tau_{p3}$ can be interpreted as the electron and hole thermal generation times of the corresponding nonequilibrium centers ΔN_- and ΔN_0.

When $N < N_D$, the ratio $N_-^e/N_0^e \gg 1$ and therefore $\tau_{p1} \ll \tau_{n1}$. Therefore the appearance of excess free carriers results in the appearance of additional (nonequilibrium) traps for electrons and centers for thermal generation of holes ($\Delta N_0 = -\Delta N_- > 0$). For such a change in the charge state of recombination centers the components τ_{p2}^{-1} and τ_{p3}^{-1} become negative with $|\tau_{p2}^{-1}| \ll |\tau_{p3}^{-1}|$, while $\tau_{n2}^{-1} \gg \tau_{n3}^{-1} > 0$. This means that $\tau_p > \tau_{p1}$ as a result of the thermal generation of holes from nonequilibrium centers ΔN_0, while $\tau_n \ll \tau_{n1}$ as a result of trapping of equilibrium electrons by these centers. As long as $N < N_D$, the concentration N_-^e increases with N, while N_0^e remains much less than N_-^e. Therefore ΔN_0 also increases. As a result of this growth, $|\tau_{p3}|$ decreases more rapidly than does τ_{p1}. As a result, at a certain value $N < N_D$ (Refs. 1, 2), the rate of thermal generation of holes from nonequilibrium centers and the rate of trapping of nonequilibrium holes on equilibrium traps become very close to each other. For this reason, τ_p starts to grow. Starting at some value of $N < N_D$ (Ref. 2), the growth of τ_n is due to the decrease of n_e with increasing N.

For $N > N_D$ the concentration N_-^e increases much more slowly than N_0^e with increasing N, and as a result the ratio τ_{n1}/τ_{p1} decreases. This in turn causes ΔN_0 to decrease as N increases. Moreover, n_e continues to decrease. Therefore the component τ_{n1}^{-1} starts to dominate in τ_n^{-1}. As a result, $\tau_n(N)$ and $\tau_p(N)$ decrease as N increases.

The ambipolar mobility (14) determines the drift velocity in the electric field of a concentration disturbance — a quasineutral cloud of positive and negative charges,[3,8] including charges bound on a deep impurity. The latter explains the fact that under extrinsic recombination conditions μ also depends on the ratio τ_p/τ_n. It is obvious that the carriers present in larger numbers more easily screen the space charge, i.e., they adjust to the drift of the other carriers. This is why under interband recombination conditions the cloud drifts in a field with the same velocity and in the same direction as the minority carriers, while in the intrinsic material it is not controlled by the field at all[3,8] ($\mu \cong \mu_p > 0$ for $n_e \gg p_e$, $\mu \cong -\mu_n < 0$ for $n_e \ll p_e$, and $\mu = 0$ for $n_e = p_e$). A similar but not exactly identical situation also obtains in the case of extrinsic recombination. Under the conditions studied, because $\tau_p < \tau_n$ (Fig. 1c) the mobility μ vanishes in the n-type

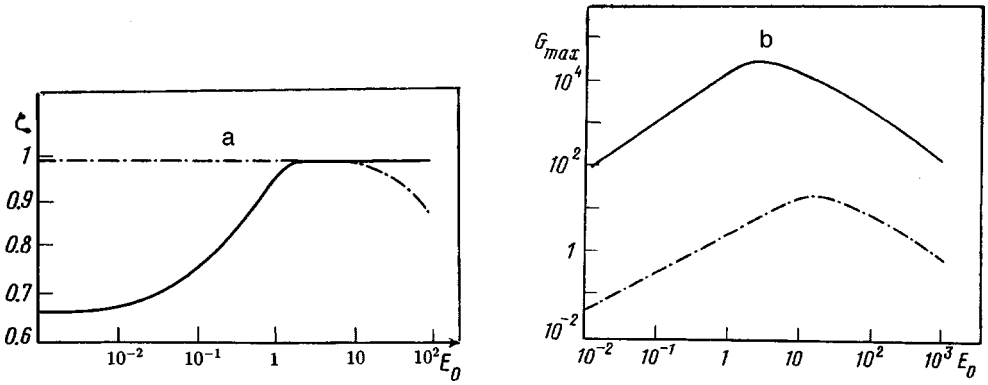

FIG. 2. The dependence on E_0 (in V/cm) of: a — the ratio $\zeta \equiv G_{\max}^{\text{app}}/G_{\max}^{\text{exact}}$, where $G_{\max}^{\text{app}}$ and $G_{\max}^{\text{exact}}$ are the approximate and exact values of $G \equiv I_{\text{ph}}/qgW$ at the maximum of the function $I_{\text{ph}}(N)$ (Fig. 1a); b — $G_{\max}$. The parameters of the semiconductors (the solid curve for GaAs, the dot-dash curve for Si) are the same as in Fig. 1.

material (for the parameters adopted in Fig. 1 this occurs for $n_e \cong 10p_e$ in silicon and $n_e \cong 10^4 p_e$ in gallium arsenide). Physically, this is due to the positive sign of the disturbance of the charge bound on a deep impurity ($\Delta N_- < 0$). The ratio p_e/n_e starts to grow substantially, and very rapidly, only when $N \cong N_D$. At the same time the ratio τ_p/τ_n cannot be of the same order of smallness as p_e/n_e. For this reason μ vanishes for $N \cong N_D$, if according to the conditions (1) the deep level is located in the bottom half of the band gap. If the same level lies in the top half of the band gap, however, then once again, because τ_p/τ_n cannot be of the same order of smallness as p_e/n_e, the function $\mu(N)$ is always positive for real values of N, and the lifetimes τ_p and τ_n always decrease as N increases.[1,2]

An increase (though small) in the carrier lifetime, apparently as a result of an increase in N, has been observed experimentally in Refs. 11 and 12.

We shall call the solution based on the relations (16) approximate. The parameter $\xi(N)$, here again remaining small, reaches its largest value near the point $N = N_{\max}$ where the function $I_{\text{ph}}(N)$ reaches its maximum value $I_{\text{ph}}^{\max}$. The deviation of the approximate value of $I_{\text{ph}}^{\max}$ from the exact value (calculated with all the terms in (12) and (13) taken into account) is presented in Fig. 2a. For $N = N_{\max}$ the exact solution is not so difficult to find, because $\mu + \mu_\xi = 0$ at this point. It is evident from Fig. 2b that $I_{\text{ph}}^{\max}$ is a nonmonotonic function of E_0. This is due to the increase in $L_{\text{eff}} = \sqrt{(D + D_E)\tau_n}$ with increasing E_0, as a result of which the losses of photoexcited carriers due to diffusion toward the current contacts and subsequent recombination there increase.

In conclusion, we note that effects similar in their physical essence to those studied above should also be observed in other media with dissociation and ion–ion recombination, e.g., in multicomponent plasmas.[13]

I wish to thank Corresponding Member of the Russian Academy of Sciences R. A. Suris for a positive assessment of the subject of this work, Corresponding Member of the Russian Academy of Sciences L. N. Kurbatov for a discussion of the results, and the Russian Fund for Fundamental Research for support under Grant 96-02-17196.

[a)]e-mail: orex@aha.ru; ost@mastak.sitek.ru

---

[1] A. A. Drugova and V. A. Kholodnov, Solid-State Electron. **38**, 1247 (1995).
[2] V. A. Kholodnov, Fiz. Tekh. Poluprovodn. **30**, 1011 (1996) [Semiconductors **30**, 538 (1996)].
[3] R. A. Smith, *Semiconductors*, Cambridge University Press, New York, 1978 [Russian translation, Mir, Moscow, 1982].
[4] J. S. Blakemore, *Solid State Physics*, Cambridge University Press, New York, 1985 [Russian translation, Mir, Moscow, 1988].
[5] E. S. Rittner, *Photoconductivity Conference*, New York, 1956, p. 215.
[6] Y. J. Shacham-Diamand and I. Kidron, Infrared Phys. **21**, 105 (1981).
[7] A. Rogalski with a contribution by M. Kimata, V. F. Kocherov, J. Piotrovski *et al.*, *Infrared Photon Detectors*, SPIE Opt. Engin. Press, Bellingham–Washington USA, 1995.
[8] V. L. Bonch-Bruevich and S. G. Kalashnikov, *Semiconductor Physics* [in Russian], Nauka, Moscow, 1990.
[9] S. M. Ryvkin, *Photoelectric Effects in Semiconductors*, Consultants Bureau, New York, 1964 [Russian original, Fizmatgiz, Moscow, 1963].
[10] A. A. Drugova and V. A. Kholodnov, in *Proceedings of ISDRS*, USA, December 1995, Vol. 1, p. 197.
[11] G. K. Wertheim, Phys. Rev. **109**, 1086 (1958).
[12] Z. V. Basheleishvili, V. S. Garnyk, S. N. Gorin, and T. A. Pagaeva, Fiz. Tekh. Poluprovodn. **18**, 1714 (1984) [Sov. Phys. Semicond. **18**, 1074 (1984)].
[13] Yu. P. Raĭzer, *Physics of Gas Discharges* [in Russian], Nauka, Moscow, 1992.

Translated by M. E. Alferieff

Observation of spin-reduction anisotropy in the quasi-one-dimensional antiferromagnet $CsMnI_3$

B. S. Dumesh

P. L. Kapitsa Institute of Physical Problems, Russian Academy of Sciences, 117334 Moscow, Russia

S. V. Petrov and A. M. Tikhonov

Institute of Spectroscopy, Russian Academy of Sciences, 142092 Troitsk, Moscow Region, Russia

(Submitted 25 March 1998)
Pis'ma Zh. Éksp. Teor. Fiz. **67**, No. 9, 661–665 (10 May 1998)

The NMR of ^{55}Mn in the quasi-one-dimensional noncollinear antiferromagnet $CsMnI_3$ at $T=1.3$ K is investigated in magnetic fields up to ~ 40 kOe. Six NMR branches corresponding to six manganese spins per magnetic unit cell are observed. The NMR spectra correspond satisfactorily to the well-known magnetic structure of $CsMnI_3$, taking into account the dynamic frequency shift due to the interaction with the low-lying AFMR modes. The average spins $\langle S_A\rangle=1.86$ and $\langle S_B\rangle=1.74$ of the magnetically nonequivalent Mn^{2+} ions are determined from the measured values of the hyperfine fields. The results obtained agree qualitatively with the calculations of spin reduction in quasi-one-dimensional antiferromagnets [Y. Watabe, T. Suzuki, and Y. Natsume, Phys. Rev. B **52**, 3400 (1995)]. © *1998 American Institute of Physics.* [S0021-3640(98)01009-3]

PACS numbers: 76.60.Es, 75.50.Ee

The properties of the crystal lattices of certain binary salts ABX_3 (A is an alkali metal, B is a 3*d* metal, and X is a halogen) make for a low dimensionality of the exchange structures formed by the B^{2+} ions. A large reduction of the average spins of the moments of magnetic ions is observed in the quasi-one-dimensional antiferromagnets (quasi-1D AFs) ABX_3 with a triangular magnetic structure. Thus, for compounds with Mn^{2+} magnetic ions ($^6S_{5/2}$ state) the average spin per ion is $\langle S\rangle\approx 1.8$, which makes it possible to study more subtle effects, for example, a change in reduction in strong magnetic fields as a result of the suppression of quantum fluctuations. In recent years a number of theoretical and experimental works have been devoted to this question.[1–3] It has been found that magnetically nonequivalent AF chains in easy-plane ''triangular'' quasi-1D AFs in strong magnetic fields have different average spins per ion.[4] According to the calculations in Ref. 5, the average spins of Mn^{2+} in magnetically nonequivalent AF chains in easy-axis triangular AFs (including $CsMnI_3$) can be different even in a zero magnetic field. The present work is devoted to verifying this assertion.

$CsMnI_3$ is a hexagonal crystal with symmetry space group D_{6h}^4. *All positions of*

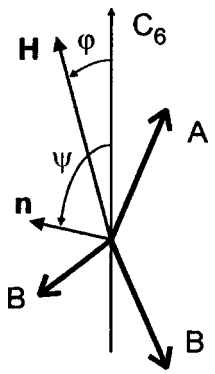

FIG. 1. Schematic diagram of the magnetic structure of $CsMnI_3$. Each AF chain is represented by one spin.

Mn^{2+} ions are crystallographically equivalent. The magnetic properties of $CsMnI_3$ can be described, to a first approximation, by a model Heisenberg Hamiltonian of a system of equivalent spins, taking into account the single-ion anisotropy and Zeeman energy of the magnetic moments in an external field **H**:

$$\mathcal{H}=2J\sum_i \mathbf{S}_i\cdot\mathbf{S}_{i+\Delta_z}+2J'\sum_i \mathbf{S}_i\cdot\mathbf{S}_{i+\Delta_\perp}+D\sum_i (S_i^z)^2-g\mu_B\mathbf{H}\cdot\sum_i \mathbf{S}_i, \tag{1}$$

where g is the g factor, μ_B is the Bohr magneton, $S=5/2$ for the Mn^{2+} ion; $J>0$, $J'>0$ are the antiferromagnetic exchange interaction integrals; and, $D<0$ is the anisotropy constant. The first term describes the exchange interaction along the C_6 axis; the second term describes the exchange interaction in a plane perpendicular to C_6. The distance between the Mn^{2+} ions along the axis is approximately half that in the plane and accordingly the exchange constants are $J=198$ GHz (Ref. 6) and $J'=1$ GHz (Refs. 6 and 7).

Below $T_{N2}=8.2$ K the magnetic structure consists of antiferromagnetic chains along the C_6 axis. In weak magnetic fields the spins of one third of the chains are directed along the axis (A spins), while in the remaining chains they make an angle $\Theta=51°\pm1°$ with the axis (B spins).[8,6] All Mn^{2+} spins are coplanar with one spin plane, if their small canting in an external field is neglected. There is no anisotropy in the hexagonal plane, so that when the magnetic field possesses a component oriented perpendicular to the C_6 axis, the normal to the spin plane is established parallel to this component. If a field is applied in the hexagonal plane, then such a structure is stable right up to a transition to the ferromagnetic state. For $\mathbf{H}\parallel C_6$ a spin-flop transition is observed in the field H_{sf} ($H_{sf}=54$ kOe at $T=2$ K); above the transition the spin of the neighboring chains apparently form a regular triangular structure oriented in a hexagonal plane. For an arbitrary orientation of the external field the spin plane rotates continuously so that[7]

$$\tan(2\psi)=\frac{H^2\sin(2\varphi)}{H^2\cos(2\varphi)-H_{sf}^2}, \tag{2}$$

where ψ is the angle between the normal **n** to the spin plane and the C_6 axis and φ is the angle between **H** and C_6 (see Fig. 1).

In accordance with the magnetic structure the ^{55}Mn NMR spectrum must consist of four branches, which in an approximation linear in H/H_n have the form

$$\frac{\omega_{n1,n2}}{\gamma_n} = H_{nA} \pm H\sin(\psi-\varphi), \quad \frac{\omega_{n3,n4}}{\gamma_n} = H_{nB} \pm H\sin(\psi-\varphi)\cos\Theta, \tag{3}$$

where $\gamma_n/2\pi = 1.06$ MHz/kOe is the gyromagnetic ratio for ^{55}Mn, $H_{nA,nB} = -A_0\langle S_{A,B}\rangle/\hbar\gamma_n$ are the hyperfine fields, and A_0 is the hyperfine interaction constant. We took into account that according to calculations[5] $\langle S_A\rangle \neq \langle S_B\rangle$. For $\varphi = \pi/2$ the terms linear in the field vanish and the twofold ($\omega_A \approx \gamma_n H_{nA}$) and fourfold ($\omega_B \approx \gamma_n H_{nB}$) degenerate branches remain.

The real NMR spectrum is much more complicated because of the dynamic frequency shift (DFS) due to the interaction with low-lying AFMR modes.[a)] In $CsMnI_3$ this phenomenon was detected from the appearance of a temperature-dependence gap in the spectrum ω_{e2} of the AFMR mode[10] and according to the strong field dependence of the NMR mode associated with it[4] in the case $\mathbf{H} \perp C_6$. In these works it is shown that the spectrum of coupled electron–nuclear oscillations can be described well by the solutions of the equation[9]

$$(\omega_{e2}^2 - \omega^2)(\omega_B^2 - \omega_2) - \omega^2\omega_T^2 = 0, \tag{4}$$

and the coupling frequencies $\omega_T \sim T^{-1/2}$ and $\omega_B(0)/2\pi \approx 390$ MHz at $T = 1.3$ K are determined. Unfortunately, in this geometry it was not possible to find the NMR mode corresponding to the spins of the A chains. For this reason, we performed an experiment with $\mathbf{H} \parallel C_6$, where the mode composition of the NMR spectrum should be substantially richer.

All experiments were performed with a wide-band cw NMR spectrometer with a reentrant resonator and frequency modulation, described in detail in Ref. 11. The spectra were obtained by passing through resonance in the magnetic field at $T = 1.3$ K. The samples were single-crystalline and were grown by the Bridgman method. The samples were oriented according to natural cleavage surfaces along binary planes. To prevent hydration the samples were coated with a protective film of rubber cement and stored in a helium atmosphere. The intensity of the magnetic field of the superconducting solenoid was measured with a Hall sensor, which was calibrated according to the NMR signal on ^{1}H protons contained in the cement.

The ^{55}Mn NMR signal was observed in a wide frequency range 250–450 MHz in magnetic fields 15–40 kOe. It consisted of several lines of width $\sim$1–5 MHz, corresponding to six possible NMR modes. The signal spectra for $\varphi < 0.5°$ and $\varphi \approx 7°$ are presented in Figs. 2 and 3. One can see that five branches are observed. We have enumerated the branches in order of decreasing frequency. In weak fields the branches *3* and *5* converge to ω_B, while branches *1* and *4* converge to $\omega'/2\pi \approx 417$ MHz. Their spectrum is close to $\omega_{1,4} = \omega' \pm \gamma_n H$ (dashed lines in the figures), making it possible to attribute these branches to oscillations of the *A* spins.

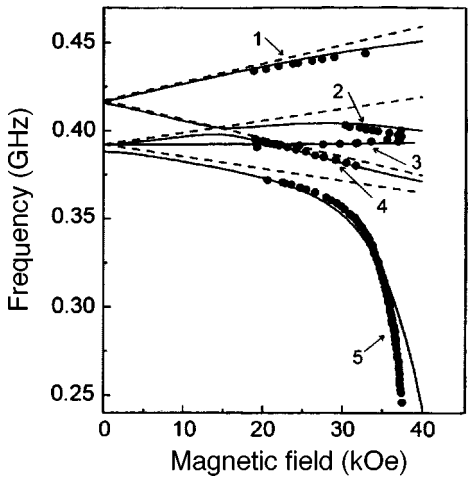

FIG. 2. ^{55}Mn NMR spectrum in $CsMnI_3$ at $T=1.3$ K and $\varphi<0.5°$: Dots — experiment, dashed lines — unshifted spectrum (3), solid lines — calculation using Eqs. (7) and (8).

For a quantitative description of the spectra it is necessary to take into account the dynamic frequency shift due to the interaction with the low-frequency AFMR modes ω_{e2} and ω_{e3}. Their spectrum in the range of fields of interest to us can be described, to a first approximation in $\varphi \ll 1$, by the formulas[7]

$$\omega_{e2}=\frac{\gamma_e\sqrt{\eta}H_{sf}H\varphi}{\sqrt{H_{sf}^2-H^2}}, \quad \omega_{e3}=\frac{\omega_{e3}(0)H_{sf}\sqrt{\eta}}{\sqrt{\eta H_{sf}^2+H^2}}\left(1-\frac{H^2}{H_{sf}^2}\right)^2\left[1+O\left(\frac{H^2}{H_{sf}^2}\varphi^2\right)\right], \tag{5}$$

where γ_e is the electron gyromagnetic ratio, $\eta=0.89$ is a phenomenological parameter,

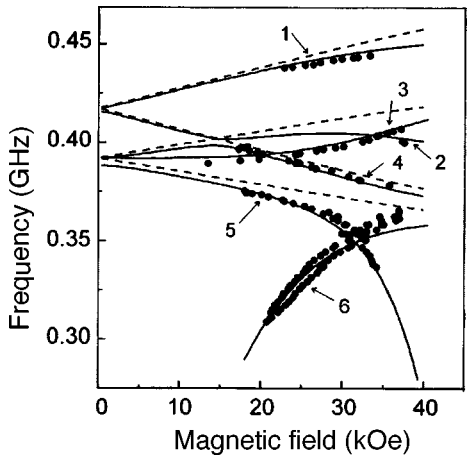

FIG. 3. ^{55}Mn NMR spectrum in $CsMnI_3$ at $T=1.3$ K and $\varphi\approx0.7°$: Dots — experiment, dashed lines — unshifted spectrum (3), solid lines — calculation using Eqs. (7) and (8).

and $\omega_{e3}(0)/2\pi = 35$ GHz is the gap in the spectrum of this mode at $H=0$. It is easy to see that a strong dependence on the angle φ occurs only for ω_{e2}. This makes it possible to distinguish the nuclear modes associated with ω_{e2}.

Comparing Figs. 2 and 3 shows that branches *1*, *4*, and *5* remain practically unchanged, while mode *3* increases appreciably in high fields and mode *2* practically vanishes, but there appears a low-frequency branch *6* which decreases with decreasing field. We attribute the vanishing of the mode *2* to a purely instrumental effect, since the weak signal from this mode is difficult to observe against the background of a strong signal from the adjacent mode *3*. The NMR signal of mode *6* consists of two overlapping lines. We attribute this to the twinned nature of the crystal with a weak disorientation of the C_6 axis and we also believe that it attests to a strong angular dependence of the spectrum of this mode. Therefore the NMR branches *3* and *6* of nuclear spins in the B positions are related with the electronic mode ω_{e2}. This corresponds to the polarization of this mode.[12] Hence it can be concluded that the modes ω_{e2} and ω_{e3} interact independently with NMR.[b)]

To describe the DFS of the NMR we employed the equation

$$(\omega_e^2-\omega^2)=\omega^2\omega_T^2\sum_i \frac{\rho_i}{\omega_{ni}^2-\omega^2}, \tag{6}$$

where the summation extends over the ''unshifted'' ω_{ni} NMR branches interacting with ω_e, while ρ_i is the fraction of nuclear spins in the ith unshifted NMR branch among the total number of nuclei involved in the interaction. Although this equation was proposed for describing the DFS in ''triangular'' AFs with easy-plane anisotropy,[11,13] it is much more general. First, it is a natural extension of Eq. (4). Second, it describes well the DFS of NMR not only in triangular $CsMnBr_3$[11] but also in all cases of multiple-sublattice AFs known to us (four-sublattice 3D AFs $CsMnF_3$ and $CsMnCl_3$).

On this basis we obtain the NMR spectra for the branches *1*, *2*, *4*, and *5* from the equation

$$(\omega_{e3}^2-\omega^2)=\frac{\omega^2\omega_T^2}{6}\left(\frac{1}{\omega_{n1}^2-\omega^2}+\frac{1}{\omega_{n2}^2-\omega^2}+\frac{2}{\omega_{n3}^2-\omega^2}+\frac{2}{\omega_{n4}^2-\omega^2}\right), \tag{7}$$

and we obtain the NMR spectra for the branches *3* and *6* from the equation

$$(\omega_{e2}^2-\omega^2)=\frac{\omega^2\omega_T^2}{2}\left(\frac{1}{\omega_{n3}^2-\omega^2}+\frac{1}{\omega_{n4}^2-\omega^2}\right), \tag{8}$$

where ω_{e2} and ω_{e3} are the unshifted AFMR frequencies from Ref. 7, the coupling frequency $\omega_T/2\pi \approx 6$ GHz at $T=1.3$ K (it is also the temperature-dependent gap in the AFMR spectrum) was obtained in Ref. 10, and ω_{ni} are the unshifted NMR frequencies from Eq. (4). The computational results are presented in Figs. 2 and 3. One can see that they describe well all modes of the NMR spectrum,[c)] for both $\varphi < 0.5°$ and $\varphi = 7°$. We have introduced the new constant $\omega_A/2\pi = 417$ MHz. Therefore we have completely described the NMR spectrum in $CsMnI_3$ with the DFS of the NMR taken into account.

From the hyperfine fields which we have obtained and the hyperfine constant $A_0 = (-1.49 \pm 0.04) \times 10^{-18}$ erg (Ref. 14), known from ESR data on Mn^{2+} in $CsMgI_3$, we

find $\langle S_A \rangle = 1.86$ and $\langle S_B \rangle = 1.74$, which is close to the value obtained from neutron scattering[8,6,15] $\langle S \rangle \approx 1.8$. The calculation in Ref. 5 gives $\langle S_A \rangle = 1.8$ and $\langle S_B \rangle = 2.0$. The difference compared with our results appears to be due to the inadequacy of the description of the magnetic properties of $CsMnI_3$ in the single-ion anisotropy model with a Hamiltonian of the form (1). The problem is that according to Ref. 5 the difference $\langle S_A \rangle - \langle S_B \rangle$ depends strongly on the ratio $|D|/J'$, changing sign at $|D|/J' \approx 1$. According to the data[15] on which this calculation was based one has $|D|/J' = 1.2$, while the AFMR data[7] imply a value $|D|/J' = 0.81 \pm 0.06$. Thus our experiment has demonstrated different spin reduction in magnetically nonequivalent Mn^{2+} chains in $CsMnI_3$, as predicted in Ref. 5; for a quantitative comparison it is necessary to improve the description of the anisotropy in substances belonging to this class.

In closing, we wish to express our sincere appreciation to N. M. Kreĭnes, M. I. Kurkin, L. A. Prozorova, A. I. Smirnov, I. A. Fomin, and D. I. Kholin for fruitful discussions.

This work was supported in part by the Russian Fund for Fundamental Research under Grant 98-02-16572 and by the U.S. Civilian Research and Development Foundation for the Independent States of the Former Soviet Union (CRDF) under Grant RP1-207. A. M. Tikhonov wishes to thank Forschungszentrum Julish GmbH.

[a)]See Ref. 9 for a more detailed discussion of this phenomenon.
[b)]As follows from Ref. 7, these modes do not interact with one another.
[c)]In our range of fields $\omega_6/2\pi \ll 200$ MHz for $\varphi < 0.5°$.

[1] T. Ohyama and H. Shiba, J. Phys. Soc. Jpn. **63**, 3454 (1994).
[2] M. E. Zhitomirsky and I. A. Zaliznyak, Phys. Rev. B **53**, 3428 (1995).
[3] A. G. Abanov and O. A. Petrenko, Phys. Rev. B **50**, 6271 (1994); P. Santini, G. Fath, Z. Domanski, and P. Erdos, Phys. Rev. B **56**, 5373 (1997).
[4] A. S. Borovik-Romanov, B. S. Dumesh, S. V. Petrov, and A. M. Tikhonov, JETP Lett. **66**, 759 (1997).
[5] Y. Watabe, T. Suzuki, and Y. Natsume, Phys. Rev. B **52**, 3400 (1995).
[6] A. Harrison, M. F. Collins, J. Abu-Dayyeh, and C. V. Stager, Phys. Rev. B **43**, 679 (1991).
[7] S. I. Abarzhi, M. E. Zhitomirskiĭ, O. A. Petrenko *et al.*, Zh. Éksp. Teor. Fiz. **104**, 3232 (1993) [JETP **77**, 521 (1993)].
[8] H. W. Zandbergen, J. Solid State Chem. **35**, 367 (1980).
[9] E. A. Turov and M. P. Petrov, *NMR in Ferro- and Antiferromagnets* [in Russian], Nauka, Moscow, 1969.
[10] L. A. Prozorova, S. S. Sosin, D. V. Efremov, and S. V. Petrov, Zh. Éksp. Teor. Fiz. **112**, 1893 (1997) [JETP **85**, 1035 (1997)].
[11] A. S. Borovik-Romanov, B. S. Dumesh, S. V. Petrov, and A. M. Tikhonov, Zh. Éksp. Teor. Fiz. **113**, 352 (1998) [JETP **86**, 197 (1998)].
[12] H. Tanaka, S. Teraoka, E. Kakehashi *et al.*, J. Phys. Soc. Jpn. **57**, 3979 (1988).
[13] I. A. Zaliznyak and N. N. Zorin, JETP Lett. **64**, 473 (1996).
[14] G. L. McPherson, R. C. Koch, G. D. Stucky, J. Chem. Phys. **60**, 1424 (1974).
[15] T. Inami, K. Kakurai, H. Tanaka, M. Enderle *et al.*, J. Phys. Soc. Jpn. **63**, 1530 (1994).

Translated by M. E. Alferieff

Gravity of monopole and string and the gravitational constant in ^{3}He-A

G. E. Volovik

Low Temperature Laboratory, Helsinki University of Technology, 02150 Espoo, Finland; L. D. Landau Institute of Theoretical Physics, Russian Academy of Sciences, 117334 Moscow, Russia

(Submitted 27 March 1998)
Pis'ma Zh. Éksp. Teor. Fiz. **67**, No. 9, 666–671 (10 May 1998)

We discuss the effective metric produced in superfluid ^{3}He-A by such topological objects as the radial disgyration and monopole. In relativistic theories these metrics are similar to that of the local string and global monopole, respectively. But in ^{3}He-A they have a negative angle deficit, which corresponds to a negative mass of the topological objects. The effective gravitational constant in superfluid ^{3}He-A, deduced from a comparison with relativistic theories, is $G \sim \Delta^{-2}$, where the gap amplitude Δ plays the part of the Planck energy. G depends on temperature roughly as $(1-T^2/T_c^2)^{-2}$ and corresponds to a screening of Newton's constant. © *1998 American Institute of Physics.*
[S0021-3640(98)01109-8]

PACS numbers: 04.80.−y, 06.20.Jr, 67.57.−z

INTRODUCTION

Effective gravity arises in many condensed matter systems. Typical examples are a crystal with dislocations and disclinations, which models an effective space with curvature and torsion (see the references cited in the latest papers[1,2] on this subject), and the normal (or superfluid) liquid, where sound waves (or phonons) propagate in the effective Lorentzian space generated by the background (super)flow.[3,4] However, it appears that superfluid ^{3}He-A provides the most fitting analogies for relativistic models of effective gravity, which can be used to simulate many different properties of the quantum vacuum.[5–8]

The quasiparticles in ^{3}He-A are chiral and massless fermions. Their spectrum is determined by 3 parameters. One of them is the gap amplitude $\Delta(T)$ which plays the part of the Planck cutoff energy. Below this cutoff, which depends on temperature T, the fermions are ''relativistic'' with the spectrum

$$E^2(\mathbf{k}) + g^{ik}(k_i - eA_i)(k_k - eA_k) = 0. \tag{1}$$

Here $\mathbf{A}$ is the dynamical vector potential of the induced ''electromagnetic field,'' $\mathbf{A} = k_F \hat{\mathbf{l}}$, where $\hat{\mathbf{l}}$ is a unit vector in the direction of the gap nodes in momentum space. The same vector determines the uniaxial anisotropy of the metric tensor of the effective space which governs the motion of fermions. In equilibrium this metric is

$$g^{ik} = -c_\perp^2(\delta^{ik} - l^i l^k) - c_\parallel^2 l^i l^k, \quad g^{00} = 1. \tag{2}$$

Here $c_\perp = \Delta(T)/p_F$ and $c_\parallel = v_F$ (with $c_\perp \ll c_\parallel$) are the ''speeds of light'' propagating transverse to $\hat{l}$ and along $\hat{l}$, respectively. The Fermi momentum k_F and the Fermi velocity v_F are practically independent of T, while $\Delta(T)$ depends strongly on T: $\Delta^2(T) \sim \Delta^2(0)(1 - T^2/T_c^2)$, where $T_c \sim \Delta(0)$ is the temperature of the superfluid transition.

If the $\hat{l}$ field is uniform, say, $\hat{l} = \hat{z}$, the anisotropy of the metric in Eq. (2) can be removed by rescaling: $z = c_\parallel Z$, $x = c_\perp X$, and $y = c_\perp Y$. However, if $\hat{l}$ field is nonuniform, the effective metric acquires a curvature, and the rescaling can be done locally but not globally. This influences the dynamics of fermions propagating in the texture in a manner similar to the gravitational field.

The question arises, what are the nature and size of the analog of the gravitational constant G in ^{3}He-A, and what is its temperature dependence? Since in ^{3}He-A the analog of the Planck energy scale is played by the gap amplitude $\Delta(T)$ (see review[8]), the gravitational constant is of order $G \sim 1/\Delta^2(T)$. However, the quantitative evaluation of G is not straightforward: because of the double role of the $\hat{l}$ field, which produces both the ''electromagnetic'' and ''gravitational'' effective fields, it is not easy to separate the ''electromagnetic'' and ''gravitational'' terms in the ^{3}He-A Lagrangian. The separation can be done only in specific situations. For example, in the analysis of the effect of an axial anomaly on the transformation of the fermionic charge into magnetic field and back, only the electromagnetic part of the $\hat{l}$ action was involved.[8] Here we discuss the opposite case, when the ''electromagnetic'' effects of the $\hat{l}$ field are absent and one has a pure ''gravitational'' field. This happens if the ''magnetic'' field $\mathbf{B} = \nabla \times \mathbf{A}$ is absent. The radial disgyration (string) with $\hat{l} = \hat{\rho}$ and the point monopole with $\hat{l} = \hat{r}$ are such textures, since both have $\nabla \times \hat{l} = 0$. Here $\hat{z}, \hat{\rho}, \hat{\phi}$ and $\hat{r}, \hat{\theta}, \hat{\phi}$ are the unit vectors of the cylindrical and spherical coordinate systems, respectively. Considering the energy of the radial disgyration and the metric produced by this topological singularity, one can deduce the effective gravitational constant G that couples these two quantities. Another estimate of G follows from a consideration of the so-called clapping mode of the order parameter, which is the analog of the graviton.

CONICAL SINGULARITY WITH NEGATIVE ANGLE DEFICIT

The radial disgyration is one of the topologically stable linear defects in ^{3}He-A. This is an axisymmetric distribution of the $\hat{\mathbf{l}}$ vector,

$$\hat{l}(\mathbf{r}) = \hat{\rho}, \tag{3}$$

with the axis of the defect line along $\hat{z}$. The interval corresponding to the metric in Eq. (2) is

$$ds^2 = dt^2 - \frac{1}{c_\perp^2} dz^2 - \frac{1}{c_\parallel^2}\left(dr^2 + \frac{c_\parallel^2}{c_\perp^2} r^2 d\phi^2 \right). \tag{4}$$

Rescaling the radial and axial coordinates, $\rho = c_\parallel R$, $z = c_\perp Z$, one obtains

$$ds^2 = dt^2 - dZ^2 - dR^2 - a^2 R^2 d\phi^2, \quad a^2 = c_\parallel^2/c_\perp^2 > 1. \tag{5}$$

In relativistic theories such a metric, but with $a^2<1$, arises outside a local string. The space outside the string core is flat, but if $a<1$ the proper length $2\pi Ra$ of a circumference of radius R around the axis is smaller than $2\pi R$. In our case we have $a^2>1$, i.e., a ''negative angle deficit.'' The conical singularity gives rise to a curvature which is concentrated at the axis of disgyration ($R=0$):[9,10]

$$\mathcal{R}^{R\phi}_{R\phi}=2\pi\frac{a-1}{a}\,\delta_2(\mathbf{R}),\quad \delta_2(\mathbf{R})=\delta(X)\,\delta(Y). \tag{6}$$

Such a metric can arise from the Einstein equations for a local cosmic string with a singular energy density concentrated in the string core,

$$\mathcal{T}^0_0=\frac{1-a}{4Ga}\,\delta_2(\mathbf{R}), \tag{7}$$

where G is the gravitational constant. Since $a=c_\parallel/c_\perp\gg 1$, this should be a rather unusual cosmic string with a large negative mass, of Planck scale. If one finds such a singular contribution to the energy density of ^{3}He-A in the presence of radial disgyration, one can identify the effective gravitational constant in ^{3}He-A.

Let us consider the distribution of the (orbital) order parameter — the complex vector $\mathbf{e}$ — in the radial disgyration:

$$\mathbf{e}(\mathbf{r})=f(\rho)\,\hat{\phi}+i\hat{z},\quad f(\rho=0)=0,\quad f(\rho=\infty)=1. \tag{8}$$

This order parameter influences the energy spectrum of the fermions in such a way that it is equivalent to the effective metric

$$ds^2=dt^2-dZ^2-dR^2-a^2f^{-2}(Rc_\parallel)R^2d\phi^2. \tag{9}$$

The function $f(\rho)$ can be obtained from the Ginzburg–Landau free energy functional, Eq. (5.4) + Eq. (7.17) in Ref. 11, which, for the chosen ansatz (8), has the form

$$F=K\frac{v_Fk_F^2}{96\pi^2}\int_0^{z_0}dz\left\{\int_{\rho<\rho_0}d^2\rho\left[\Lambda(1-f^2)^2+\frac{f^2}{\rho^2}+\left(\frac{df}{d\rho}\right)^2\right]-2\pi\int_0^{\rho_0}d\rho\,\frac{df^2}{d\rho}\right\}. \tag{10}$$

Here ρ_0 and z_0 are the radius and the height of the cylindrical vessel with the disgyration on the axis; $\Lambda\sim\Delta^2/v_F^2$; the overall dimensionless factor K in the Ginzburg–Landau region close to the transition temperature T_c is

$$K(T)=1-T^2/T_c^2,\quad T\to T_c. \tag{11}$$

One can see that the first term in the curly brackets in Eq. (10) is some kind of dilaton field, while the second term is just what we need: it is a pure divergence and thus can be represented as a singular term which does not depend on the exact structure of the disgyration core but nevertheless contributes the core energy:

$$\mathcal{F}_{\rm div}=-2\pi K\frac{v_Fk_F^2}{96\pi^2}\,\delta_2(\rho),\quad F_{\rm div}=\int d^3x\mathcal{F}_{\rm div}=-K\frac{v_Fk_F^2}{48\pi}. \tag{12}$$

Now let us extract the constant G by comparing this core energy with the string mass M obtained by integration of $\mathcal{T}^0_0$:

$$M=\int d^3X\sqrt{-g}T^0_0=\frac{1-a}{4G}Z_0. \tag{13}$$

Translating this to the ^{3}He-A language, where the ''proper'' length is $Z_0=z_0/c_\perp$, and taking into account that $a=c_\parallel/c_\perp\gg 1$, one has

$$M=-\frac{c_\parallel}{4Gc_\perp^2}z_0. \tag{14}$$

Then from equation $F_{\rm div}=M$, one obtains the gravitational constant

$$G(T)=12\pi/K(T)\Delta^2(T). \tag{15}$$

Though we cannot extrapolate the temperature dependence of $K(T)$ in Eq. (11) to low T, we can expect that the overall temperature dependence can be approximated by

$$G(T)\sim G(0)\left(1-\frac{T^2}{T_c^2}\right)^{-2},\quad G(0)\sim\frac{1}{T_c^2}\sim\frac{1}{\Delta^2(0)}, \tag{16}$$

where $G(0)$ is the value of G at $T=0$.

The negative mass M does not mean that the vacuum is unstable with respect to string formation: the energy of the radial disgyration is dominated by the first (dilatonic) term in the curly brackets in Eq. (10),

$$E_{\rm disg}(\rho_0)=K\frac{v_F k_F^2}{48\pi}z_0\ \ln\frac{\rho_0\Delta}{c_\parallel}. \tag{17}$$

Translating this to the relativistic language, one obtains

$$E_{\rm disg}(R_0)=\frac{a}{4G}Z_0\ \ln\frac{R_0}{R_{\rm Planck}}, \tag{18}$$

where $R_{\rm Planck}=1/\Delta$ is the Planck radius. This energy is larger by the logarithmic factor than the negative ''mass of matter'' $F_{\rm div}=M$ in Eq. (13), which is related to the string core. So the situation in this example of ^{3}He-A gravity is as follows: The energy in Eq. (17) is not gravitating, but it determines the metric. This metric, through the Einstein equation, gives rise to a negative mass M, which then contributes to the core energy of disgyration. This is an example of how in the effective theory the vacuum is not gravitating but determines the metric.

GRAVITATIONAL CONSTANT FROM GRAVITON ENERGY–MOMENTUM

An independent estimation of G in ^{3}He-A is obtained using the energy of the graviton field. In the relativistic theory the energy density of a graviton propagating along Z is

$$T^0_0=\frac{1}{16\pi G}\left[(\partial_Z h_{XY})^2+\frac{1}{4}(\partial_Z(h_{XX}-h_{YY}))^2\right]. \tag{19}$$

Let us consider the corresponding energy density in ^{3}He-A. For this purpose we choose the complex order parameter vector **e** in the form

$$\mathbf{e}(z)=\left[\left(1+\frac{1}{2}h_{XX}(z)\right)\hat{x}+\frac{1}{2}h_{XY}(z)\hat{y}\right]+i\left[\left(1+\frac{1}{2}h_{YY}(z)\right)\hat{y}+\frac{1}{2}h_{XY}(z)\hat{x}\right]. \tag{20}$$

It corresponds to the following effective metric for the quasiparticles propagating against the background of this order parameter:

$$ds^2=dt^2-dZ^2-(1+h_{XX}(Z))dX^2-(1+h_{YY}(Z))dY^2-2h_{XY}(Z)dXdY. \tag{21}$$

The gradient part of the Ginzburg–Landau free energy functional for this ansatz (20) has the form

$$\mathcal{F}=K\frac{v_F k_F^2}{96\pi^2}(\nabla_i\mathbf{e}\nabla_i\mathbf{e}^*+\nabla_i e_j\nabla_j e_i^*+\nabla_i e_i\nabla_j e_j^*), \tag{22}$$

$$\mathcal{F}=K\frac{v_F k_F^2}{192\pi^2}\left[\frac{1}{4}(\partial_z(h_{XX}+h_{YY}))^2+(\partial_Z h_{XY})^2+\frac{1}{4}(\partial_z(h_{XX}-h_{YY}))^2\right]. \tag{23}$$

The first term in Eq. (23) describes the so-called pair-breaking mode of the order parameter, which is the analog of the (spin 0) dilaton energy. The other two terms describe the so-called clapping mode, which corresponds to the (spin 2) graviton.[7] From a comparison of the clapping mode energy in Eq. (23) and the graviton energy in Eq. (19), one obtains the same value for the gravitational constant as in Eq. (15).

MONOPOLE

In ^{3}He-A the monopole is the hedgehog in the $\hat{l}$ field, $\hat{l}=\hat{r}$, which is the termination point of the quantized vortex (the vortex is analogous to the spinning or torsion string). The effective metric far from the string is

$$ds^2=\left(dt+\frac{\hbar}{2m_3c_\perp^2}(1-\cos\,\theta)d\phi\right)^2-\frac{1}{c_\parallel^2}dr^2-\frac{1}{c_\perp^2}r^2(d\theta^2+\sin^2\,\theta d\phi^2). \tag{24}$$

The spinning string terminating on the monopole can be removed by the following trick. Let us introduce electrically charged ^{3}He-A, i.e., a superconductor with the ^{3}He-A order parameter. Then put the t'Hooft–Polyakov magnetic monopole to the hedgehog. In this case the Abrikosov string will be cancelled and thus one obtains only the point singularity in the $\hat{l}$ field—the hedgehog—with pinned magnetic monopole.[12] After rescaling of the radial coordinate $R=r/c_\parallel$ one obtains the metric

$$ds^2=dt^2-dR^2-a^2R^2(d\theta^2+\sin^2\theta d\phi^2),\quad a^2=c_\parallel^2/c_\perp^2\,. \tag{25}$$

This metric describes the 3D conical singularity.[9] In relativistic theories such a metric, but with $a^2<1$, arises for global monopoles.[13,14] In our case we have $a^2>1$, i.e., a ''negative deficit'' of the solid angle. This situation is also different from the solid angle deficit $>4\pi$ discussed in Ref. 15, where $a^2<0$, giving rise to instability of the stationary monopole and to inflation. The nonzero curvature elements and the corresponding energy density of matter are[9]

$$\mathcal{R}^{\theta\phi}_{\theta\phi}=-\frac{1-a^2}{a^2R^2},\quad \mathcal{R}=2\mathcal{R}^{\theta\phi}_{\theta\phi},\quad \mathcal{T}_0^0=\frac{1-a^2}{a^2 8\pi GR^2}. \tag{26}$$

Integrating the energy density, one obtains a negative contribution to the monopole energy (at $a \gg 1$):

$$M(R_0) = \int_{R<R_0} d^3R \sqrt{-g} T_0^0 = -\frac{a^2}{2G} R_0. \tag{27}$$

Translating to the language of ^{3}He-A with the value of G from Eq. (15) and with $r_0 = R_0 c_\parallel$ being the radius of spherical vessel, one obtains

$$M(r_0) = -\frac{c_\parallel}{2c_\perp^2 G} r_0 = -\frac{K(T)}{24\pi} v_F k_F^2 r_0 . \tag{28}$$

The real energy of the radial $\hat{l}$-texture (without the attached spinning string) is $2|M(r_0)|$, as follows from Eq. (22). However, we cannot unambiguously identify the obtained negative mass with some specific term in ^{3}He-A: all the terms have the same $1/r^2$ dependence. This is distinct from the case of disgyration, where the negative contribution has a δ-function singularity and we could easily identify it with the similar negative-energy δ-function contribution to the ^{3}He-A action. One possibility, that this negative mass can be identified as the interaction of the magnetic field of the monopole with the orbital momentum of the $\hat{l}$ field in the charged ^{3}He-A, will be discussed elsewhere.

CONCLUSION

We have considered two metrics with nonzero curvature arising in the ^{3}He-A textures. The same metrics occur outside the local cosmic string and the global cosmic monopole, both with the negative mass. In the case of the local cosmic string the negative energy comes from the δ-function singularity of the curvature. For the ^{3}He-A disgyration the negative energy contribution to the textural energy also comes from a δ-function term in the action. Identifying these two negative energy terms with each other, we obtained the value of the effective gravitational constant $G(T)$ in ^{3}He-A. The same value is obtained from the energy–momentum tensor for the analog of the graviton in ^{3}He-A. $G(T)$ is inversely proportional to the square of the ''Planck'' energy and increases with T, which corresponds to vacuum screening of the gravity. The temperature dependence of the gravitational constant leads to its time dependence during the evolution of the Universe. The latter has been extensively discussed starting with the Dirac proposal (see review[16]).

From consideration of ^{3}He-A it was found that there are two contributions to the temperature dependence of G in Eq. (15). (i) The dependence coming from the factor $K(T)$ is the traditional one. Since the effective gravity is obtained from an integration over the fermionic (or bosonic) degrees of freedom,[17] it is influenced by the thermal distribution of fermions. In relativistic theories, even at low T the renormalization of G is model-dependent: it depends not only on the fermionic and bosonic fields, but also on the cutoff function if the gravitons are included.[18] (ii) Another source of the temperature dependence of $G(T)$ in Eq. (15) is that the ''Planck'' energy cutoff $\Delta(T)$ depends on temperature. Even at low T this dependence is determined by trans-Planckian physics.

I thank Matt Visser, who pointed out that the metric induced by the radial disgyration in ^{3}He-A corresponds to a negative mass of the string in the relativistic theory, and Alexei Starobinsky for illuminating discussions.

[1] M. O. Katanaev and I. V Volovich, ''Scattering on dislocations and cosmic strings in the geometric theory of defects,'' http://xxx.lanl.gov/abs/gr-qc/9801081.
[2] R. Bausch and R. Schmitz, Phys. Rev. Lett. **80**, 2257 (1998).
[3] W. G. Unruh, Phys. Rev. Lett. **46**, 1351 (1981).
[4] M. Visser, ''Acoustic black holes: horizons, ergospheres, and Hawking radiation,'' http://xxx.lanl.gov/abs/gr-qc/9712010.
[5] G. E. Volovik and T. Vachaspati, Int. J. Mod. Phys. B **10**, 471 (1996).
[6] T. Jacobson and G. E. Volovik, ''Event horizons and ergoregions in ^{3}He,'' http://xxx.lanl.gov/abs/cond-mat/9801308.
[7] G. E. Volovik, *Exotic properties of superfluid ^{3}He*, World Scientific, Singapore, 1992.
[8] G. E. Volovik, ''Axial anomaly in 3He-A,'' http://xxx.lanl.gov/abs/cond-mat/9802091.
[9] D. D. Sokolov, A. A. Starobinsky, Dokl. AN SSSR, **234**, 1043 (1977) [Sov. Phys. Dokl. **22**, 312 (1977)].
[10] M. Banados, C. Teitelboim, and J. Zanelli, Phys. Rev. Lett. **69**, 1849 (1992).
[11] D. Vollhardt and P. Wölfle, *The superfluid phases of helium 3*, Taylor & Francis, London, 1990.
[12] G. E. Volovik, Usp. Fiz. Nauk. **143**, 73 (1984) [Sov. Phys. Usp. **27**, 363 (1984)].
[13] M. Barriola and A. Vilenkin, Phys. Rev. Lett. **63**, 341 (1989).
[14] D. Harari and C. Lousto, Phys. Rev. D **42**, 2626 (1990).
[15] I. Cho and A. Vilenkin, Phys. Rev. D **56**, 7621 (1997).
[16] J. D. Barrow, ''Varying G and other constants,'' http://xxx.lanl.gov/abs/gr-qc/9711084.
[17] A. D. Sakharov, Dokl. Akad. Nauk **177**, 70 (1968) [Sov. Phys. Dokl. **12**, 1040 (1968)].
[18] M. Reuter, Phys. Rev. D **57**, 971 (1998).

Published in English in the original Russian journal. Edited by Steve Torstveit.

Behavior of the atomic and magnetic structure of $La_{0.35}Pr_{0.35}Ca_{0.30}MnO_3$ at a metal–insulator phase transition

A. M. Balagurov, V. Yu. Pomyakushin, V. L. Aksenov, and N. M. Plakida
Joint Institute for Nuclear Research, 141980 Dubna, Russia

N. A. Babushkina and L. M. Belova
Kurchatov Institute Russian Science Center, 123182 Moscow, Russia

O. Yu. Gorbenko and A. R. Kaul'
M. V. Lomonosov Moscow State University, 119899 Moscow, Russia

P. Fischer, M. Gutmann, and L. Keller
Paul Scherrer Institute, CH-5232 Villigen, Switzerland

(Submitted 30 March 1998)
Pis'ma Zh. Éksp. Teor. Fiz. **67**, No. 9, 672–677 (10 May 1998)

The evolution of the structural and magnetic properties of the CMR (colossal-magnetoresistance) compound $La_{0.35}Pr_{0.35}Ca_{0.30}MnO_3$ as the temperature changes from 10 to 293 K is investigated by means of neutron diffraction. It is shown that the changes in the transport and magnetic properties are directly related with the rearrangement of the atomic structure. A phase transition to the metallic state occurs together with simultaneous ferromagnetic ordering of the manganese moments and is accompanied by a jump in volume. The static distortions of the oxygen octahedra which are observed to occur prior to the magnetic phase transition and which are practically absent at room temperature and in the FM phase attest to the orbital ordering of oxygen atoms on the bonds, with freezing-in of the Jahn–Teller modes. © *1998 American Institute of Physics.* [S0021-3640(98)01209-2]

PACS numbers: 75.70.Pa, 72.60.+g, 61.12.Ld

The perovskites $La_{1-x}A_xMnO_3$, where A = Ca, Sr, and Ba, have been under intensive study in recent years, since the discovery of negative colossal magnetoresistance (CMR) in them at the beginning of the 1990s.[1] Depending on the doping level, temperature, or magnetic field strength, these crystals are found in two basic states — antiferromagnetic or paramagnetic insulator or ferromagnetic metal with ordered magnetic moments of manganese. Numerous investigations (see, for example, the reviews Refs. 2 and 3) have shown that the insulator–metal and paramagnet–ferromagnet transitions are interrelated and the transition temperatures T_{I-M} and T_c are close or equal to each other. Both the properties of the metallic phase and this interrelationship are ordinarily described on the basis of the ''double exchange'' model, which was introduced at the beginning of the 1950s.[4] However, recently discovered features of the phase transitions

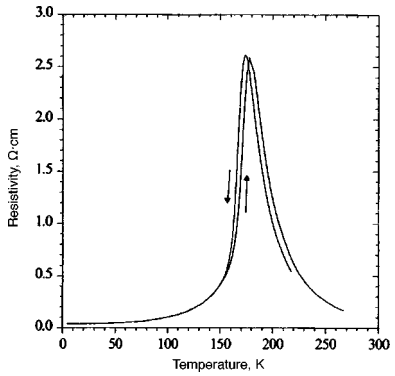

FIG. 1. Electrical resistivity of the ceramic $La_{0.35}Pr_{0.35}Ca_{0.30}MnO_3$ as a function of temperature.

occurring in CMR compounds and the ground state of these compounds have shown that the complete picture cannot be described solely by this model; it is necessary to enlist the interaction of electrons with the crystal lattice.

It is well known that, just as external fields, complete or partial substitution of rare-earth elements with a short ionic radius for La makes it possible to change the charge and magnetic state of a CMR compound. Of special interest are compositions in which lanthanum is replaced by praseodymium, since the narrow-gap CMR compounds obtained in so doing possess a rich phase diagram, as is shown, for example, by detailed neutron diffraction investigations of the magnetic states of $Pr_{1-x}Ca_xMnO_3$ (Ref. 5) and precise structural investigations of the compositions $(La–Pr)_{1-x}(Ca–Sr–Ba)_xMnO_3$ (Ref. 6).

In the present letter we report new experimental data obtained for the CMR compound $La_{0.35}Pr_{0.35}Ca_{0.30}MnO_3$ (referred to below as LPCM) mainly by neutron diffraction. This composition is of interest because of its unusual transport properties, manifested in the dependence of the resistivity at liquid-helium temperatures on the time and on the method of cooling.[7] In the compound $(La_{0.25}Pr_{0.75})_{0.7}Ca_{0.30}MnO_3$ a ''giant'' isotope effect is also observed — complete suppression of a transition to the ferromagnetic metallic phase accompanying the substitution of ^{16}O for ^{18}O (Ref. 8), indicating the important role of lattice dynamics in this transition.

An experimental sample with the composition $(La_{0.5}Pr_{0.5})_{0.7}Ca_{0.3}MnO_3$ was prepared in the form of a powder by means of the so-called ''paper synthesis.'' For this, an aqueous solution of a mixture of La, Pr, Ca, and Mn nitrates taken in the required ratios was deposited on ash-free paper filters, which were dried (120 °C) and then burned. The oxide products thus obtained was roasted in air at 700 °C for 2 h. The final heat treatment consisted of annealing pressed tablets in air at 1200 °C for 12 h. The tablets obtained were ground into a powder prior to the neutron diffraction experiment. Preliminary x-ray analysis showed the sample to be uniform and orthorhombic.

Figure 1 shows the electrical resistivity of a ceramic sample of LPCM, measured by the standard four-contact method, versus temperature. At a temperature $T_C \approx 175$ K a transition occurs to a metallic state with a small hysteresis. We note that the comparatively small decrease in the resistivity with a further decrease of temperature (only a

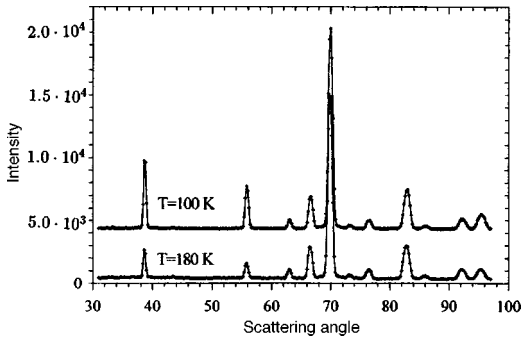

FIG. 2. Diffraction spectrum of $La_{0.35}Pr_{0.35}Ca_{0.30}MnO_3$ measured with the DMC diffractometer at $T=100$ K and 180 K. A sharp increase in the intensity of the diffraction peaks at $2\theta=38.6°$ ($d=3.86$ Å) and $2\theta=55.8°$ ($d=2.73$ Å) in the FM phase is clearly seen.

severalfold decrease, whereas in single crystals the resistivity ordinarily decreases by several orders of magnitude) is due to the ceramic character of the sample.

The neutron diffraction experiments were performed on two neutron diffractometers: HRFD at the Laboratory of Neutron Physics at JINR (Dubna, Russia) using the IBR-2 reactor, and DMC at the Paul Scherrer Institute (Villigen, Switzerland) using the SINQ source. HRFD has a resolution of 10^{-3} in $\Delta d/d$, making it possible to obtain precise structural information; DMC is located on a cold neutron source and is well adapted for measuring weak magnetic peaks near large values of d_{hkl}. The HRFD diffraction spectra were measured in a regime with the sample cooled at room temperature and in ranges from 200 to 140 K and from 40 to 10 K. The DMC spectra were measured primarily in the heating regime and, moreover, in different cooling regimes; in addition, several measurements were performed at $T=10$ K at 1-hour intervals. However, no nonstationary effects falling outside the random error limits were found in the diffraction experiments.

Analysis of the magnetic structure of LPCM, performed on the basis of the DMC data (Fig. 2), showed the compound to be a collinear ferromagnet at $T<T_C\approx 175$ K with the magnetic moment of the manganese atoms lying in a plane perpendicular to the long axis of the unit cell. The temperature dependence of the ordered magnetic moment of Mn is shown in Fig. 3. In the saturated state ($T\ll T_m\approx 150$ K) the ordered magnetic moment equals 3.4 μ_B, which is close to the expected average value calculated on the assumption that the structure contains 70% Mn^{3+} and 30% Mn^{4+}. In $Pr_{0.7}Ca_{0.3}MnO_3$, as was shown in Ref. 9, in addition to the antiferromagnetic ($T<T_N\approx 150$ K) and ferromagnetic ($T<T_C\approx 120$ K) ordering of the Mn moments, the magnetic moments of Pr also become ordered (at $T\approx 50$ K). However, analysis of the intensities of the magnetic diffraction peaks in LPCM did not reveal AFM ordering or any significant indications of ordering of the magnetic moments of Pr.

Data on the temperature dependence of the unit-cell parameters and the coordinates of the atoms in LPCM were obtained in the HRFD diffractometer. A typical HRFD neutron diffraction pattern analyzed by the Rietveld method is shown in Fig. 4. The room-temperature parameters of the structure are given in Table I. LPCM crystallizes in the orthorhombic space group *Pnma*, the standard group for perovskite CMR compounds.

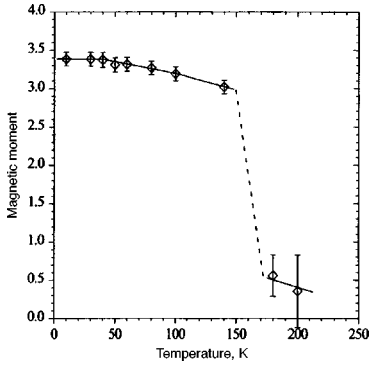

FIG. 3. Ordered magnetic moment (in Bohr magnetons) of Mn versus temperature, determined from the DMC spectra.

In this arrangement the unit cell parameters are related to the parameters a_p of cubic perovskites as $a \approx c \approx \sqrt{2}a_p$, $b \approx 2a_p$. The lowering of the symmetry from cubic to the orthorhombic group *Pnma* is due to rotation of the MnO_6 octahedra. The appearance of Jahn–Teller distortions of the oxygen octahedra around Mn^{3+}, which can give three independent Mn–O bonds, do not further lower the symmetry in the *Pnma* group.

The room-temperature unit-cell parameters and coordinates of the atoms in LPCM (see Table I) are almost identical to the recently published values for $La_{0.525}Pr_{0.175}Ca_{0.30}MnO_3$ (Ref. 6). A distinctive feature of LPCM is that, while having a structure described in the orthorhombic space group, which is maintained over the entire experimental temperature range from 8 to 290 K, this compound is metrically pseudo-tetragonal, i.e., the basal cell parameters are close or even identical (Fig. 5). The orthorhombic distortion, $r = 2(c-a)/(c+a)$, for LPCM does not exceed 5×10^{-4} at $T = 180$ K, while ordinarily this quantity equals $\sim 2 \times 10^{-3}$. Moreover, the LPCM lattice is

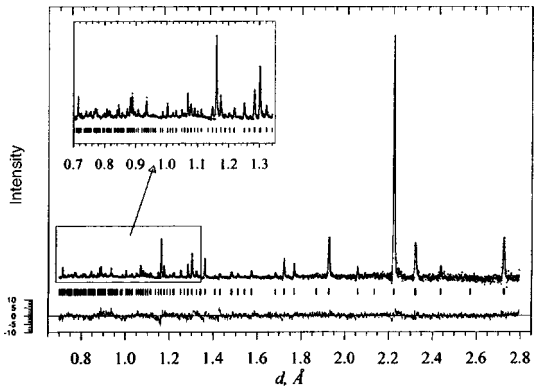

FIG. 4. Diffraction spectrum of $La_{0.35}Pr_{0.35}Ca_{0.30}MnO_3$ measured with the HRFD diffractometer at $T = 40$ K. The experimental points, the curve calculated by the Rietveld method, and the difference curve normalized to the standard deviation are shown.

TABLE I. Lattice parameters and coordinates of atoms in $La_{0.35}Pr_{0.35}Ca_{0.30}MnO_3$ at $T=293$ K, determined with the HRFD diffractometer, and $La_{0.525}Pr_{0.175}Ca_{0.30}MnO_3$ ($T=300$ K), taken from Ref. 6.

A/A' site		$La_{0.35}Pr_{0.35}Ca_{0.30}$	$La_{0.525}Pr_{0.175}Ca_{0.30}$
a	(Å)	5.4606 (1)	5.4585 (2)
b	(Å)	7.7067 (1)	7.7146 (2)
c	(Å)	5.4603 (1)	5.4674 (2)
V	(Å^3)	229.79	230.23
A/A'	x	0.0271 (4)	0.0236 (4)
	y	0.25	0.25
	z	–0.0054 (6)	–0.0057 (7)
$O1$	x	0.4934 (6)	0.4893 (7)
	y	0.25	0.25
	z	0.0682 (5)	0.0668 (5)
$O2$	x	0.2818 (3)	0.2782 (5)
	y	0.0355 (2)	0.0342 (2)
	z	0.7168 (4)	0.7198 (4)
$R_{wp}^{*)}$	%	6.88	5.75
χ^2		1.46	1.66

*) R_{wp} is the weighting R factor.

pseudocubic, since $b/\sqrt{2}$ is close to a and c. It is possible that this property facilitates the appearance of dynamical spatial fluctuations of fragments of the LPCM structure, which is what determines the unusual properties of this compound.

Figure 5b shows the temperature dependence of the unit-cell volume of the crystal. It is clear that at the transition to the metallic state in a region where a saturated ferromagnetic phase has already appeared, a volume jump of the order of 0.15% occurs at $T_m \approx 150$ K. Such a strong volume change can hardly be due to the establishment of ferromagnetic order, since in 3d compounds the volume jump is typically $\sim 10^3$ times smaller, and must be due to a structural rearrangement. It is interesting that a cell volume jump of a similar magnitude (0.13%) has been observed in the compound

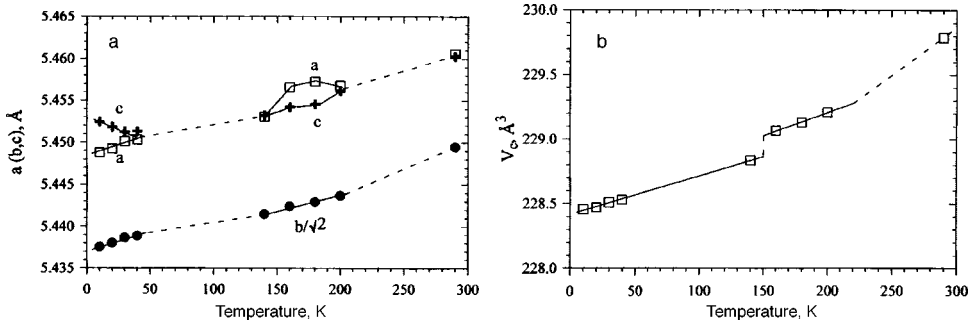

FIG. 5. a) Lattice parameters of $La_{0.35}Pr_{0.35}Ca_{0.30}MnO_3$ (space group $Pnma$, $a \approx c$), and b) unit cell volume, all determined from the HRFD spectra. At $T_c=175$ K the compound undergoes a transition to a ferromagnetic phase. The errors of the experimental points are smaller than the size of the symbols.

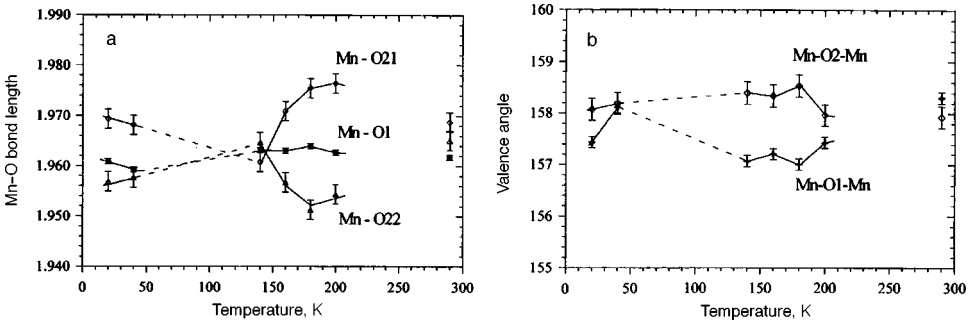

FIG. 6. Interatomic distances Mn–O (a) and angles Mn–O–Mn (b) versus temperature. The Mn–O1 bond is directed along the b axis and the Mn–O21 and Mn–O22 bonds lie in the (a,c) plane.

$La_{0.75}Ca_{0.25}MnO_3$ at a transition to the FM state, while in $La_{0.5}Ca_{0.5}MnO_3$, where the arrangement of the Mn^{3+} and Mn^{4+} ions is presumed to be ordered, there is no volume jump.[10]

Analysis of the characteristic interatomic bond lengths (Fig. 6a) shows that the coherent distortion of the oxygen octahedra is very small at room temperature and in the ferromagnetic state. The axial distance, Mn–O1, decreases slightly as temperature decreases from room temperature to 40 K. At the same time the equatorial bonds Mn–O21 and Mn–O22 change appreciably and synchronously (at least, starting at the temperature 200 K, which is designated below as T_0), attesting to ordering of the static Jahn–Teller distortions in the equatorial plane of the octahedra. The coherent (static) part of the Jahn–Teller distortions at T_0 can be estimated using the formulas for local modes:[11]

$$Q_2=\frac{l-s}{\sqrt{2}}\approx 0.011(2)\text{Å}, \quad Q_3=\frac{2(2m-l-s)}{\sqrt{6}}\approx -0.004(4)\text{Å},$$

where l, s, and m are the Mn–O2 (long and short) and Mn–O1 (average) bond lengths. It is obvious that in LPCM the governing mode is Q_2, which responsible for the distortions of the octahedra in the equatorial plane. After the saturated ferromagnetic phase is reached at $T_m\approx 150$ K the Mn–O21 and Mn–O22 bond lengths become equal and remain close down to low temperatures. The Mn–O2–Mn angles behave differently (Fig. 6b): The equatorial angle Mn–O2–Mn remains practically constant, while the axial angle Mn–O1–Mn decreases appreciably near T_C.

It is interesting to note that below $T=40$ K the behavior of the lattice parameters and, to some degree, the lengths of the interatomic bonds once again become nonlinear. This could be due to ordering of the magnetic moments of Pr (just as in Ref. 9). However, the ordering effect is too weak and is not manifested in the intensities of the diffraction peaks.

In conclusion, we shall give a qualitative theoretical interpretation of the results obtained. As was noted in Ref. 5, in (Pr–Ca)MnO_3 with Ca ion concentrations close to $x=0.30$, one can expect ordering of the Mn charges and orbitals of the type $d(z^2)$ in the equatorial plane. Apparently, this is what happens as the temperature is decreased below room temperature. As discussed above, for $T_0\approx 200$ K the difference between the

Mn–O21 and Mn–O22 bond lengths becomes substantial, attesting to ordering of oxygen in bonds through a freezing-in of the Jahn–Teller modes Q_2 and Q_3. However, ''melting'' of the orbital ordering occurs at a transition to the saturated high-conductivity ferromagnetic phase at $T_m \approx 150$ K, resulting in equalization of the lengths of the Mn–O21 and Mn–O22 bonds in the equatorial plane. Together with the volume jump a substantial change in the lattice parameter a also occurs.

In summary, the present investigation confirms the sequence of phase transitions observed in narrow-gap CMR materials:[9] orbital (and possibly charge) ordering at a temperature T_0 preceding a ferromagnetic transition at T_C. Orbital ordering completely breaks down only at T_m in the saturated ferromagnetism phase with high conductivity ($T_m < T_C < T_0$). The band gap for e_g electrons in our compound $(La_{0.5}Pr_{0.5})_{0.7}Ca_{0.3}MnO_3$, which is somewhat larger than in the compound $Pr_{0.7}Ca_{0.3}MnO_3$ (Ref. 9) on account of the large-radius La ions, makes it possible also to observe a transition to the metallic state at the ferromagnetic transition at $T_C \approx 175$ K. We note that an identical sequence of phase transitions has been observed[12] in the compound $Pr_{0.65}(Ca_{1-y}Sr_y)_{0.35}MnO_3$, where the band gap for e_g electrons was changed by substituting large-radius Sr ions for Ca ions. In that study charge ordering was observed, for example, for $y = 0.3$, in the region $T_m < T < T_{c0}$, where $T_m \approx 50$ K is the saturation temperature of the ferromagnetism, which arises at $T_C \approx 100$ K, and $T_{c0} \approx 200$ K is the charge-ordering temperature. On the whole our investigation confirms that the Jahn–Teller effect (see, for example, Ref. 13) and the double-exchange mechanism together play a large role in the insulator–metal transition, accompanied by colossal magnetoresistance, in manganates.

We thank V. G. Simkin and A. V. Pol' for assisting in the HRFD neutron diffraction experiment and N. B. Perkins for assisting in the preparation of the manuscript. This work was supported under a program of the Russian Fund for Fundamental Research (Projects 96-02-17823, 97-0216655, 97-02-17103, and 97-03-32979a) and by the INTAS-RFFI fund (Project 95-639).

[1] V. Helmot, J. Wecker, B. Holzapfel *et al.*, Phys. Rev. Lett. **71**, 2331 (1993).
[2] É. L. Nagaev, Phys. Usp. **166**, 833 (1996).
[3] C. N. R. Rao, A. K. Cheetham, and R. Mahesh, Chem. Mater. **8**, 2421 (1996).
[4] C. Zener, Phys. Rev. **82**, 403 (1951).
[5] Z. Jirak, S. Krupicka, Z. Simsa *et al.*, J. Magn. Magn. Mater. **53**, 153 (1985).
[6] P. G. Radaelli, G. Iannone, M. Marezio *et al.*, Phys. Rev. B **56**, 8265 (1997).
[7] N. A. Babushkina, L. M. Belova, O. Yu. Gorbenko *et al.*, to be published.
[8] N. A. Babushkina, L. M. Belova, O. Yu. Gorbenko *et al.*, Nature **391**, 159 (1998).
[9] D. E. Cox, P. G. Radaelli, M. Marezio *et al.*, Phys. Rev. B **57**, 3305 (1998).
[10] P. G. Radaelli, D. E. Cox, M. Marezio *et al.*, Phys. Rev. Lett. **75**, 4488 (1995).
[11] J. Kanamori, J. Appl. Phys. Suppl. **31**, 14S (1960).
[12] Y. Tomioka, A. Asamitsu, H. Kuwahara, and Y. Tokura, J. Phys. Soc. Jpn. **66**, 302 (1997).
[13] A. J. Millis, B. I. Shraiman, and R. Mueller, Phys. Rev. Lett. **77**, 175 (1996).

Translated by M. E. Alferieff

Polymers from C_{60} barrelenes

L. A. Chernozatonskiĭ[a)]
Institute of Biochemical Physics, Russian Academy of Sciences, 117334 Moscow, Russia

E. G. Gal'pern and I. V. Stankevich
Institute of Heteroorganic Compounds, Russian Academy of Sciences, 117813 Moscow, Russia

(Submitted 2 April 1998)
Pis'ma Zh. Éksp. Teor. Fiz. **67**, No. 9, 678–683 (10 May 1998)

Dimer, trimer, and chain structures consisting of covalently joined barrel-shaped C_{60} monomers (barrelenes) with different types of bonds are modeled. The computed distances between the centers of the molecules within a barrelene chain (0.70–0.74 nm) and between the symmetry axes of the chains (0.63–0.77 nm) are comparable to the analogous distances on the surface of fullerites synthesized by Davydov's group [V. A. Davydov, L. S. Koshevarova, A. V. Rakhmanina *et al.*, JETP Lett. **63**, 818 (1996)] and subjected to high pressures ($\sim$10 GPa) and heating ($\sim$700 K). The formation of special two-dimensional structures (triangles, squares, chains with a kink, stars), which are observed experimentally, is explained on the basis of the model, and 3D polymer structures consisting of C_{60} barrelenes with density close to that of samples obtained earlier are constructed. © *1998 American Institute of Physics.* [S0021-3640(98)01309-7]

PACS numbers: 81.05.Zx, 81.05.Lg, 81.05.Tp

Under high pressures $P\sim 10$ GPa and temperatures $T\sim 1000$ K fullerite C_{60} forms very hard multiphase structures — a molecular polycrystal transforms into different phases of covalently bonded C_{60} molecules.[1–3]

Molecular chains and associations with unusual distances between the centers of the molecules within a chain — 0.65 ± 0.04 nm and between the symmetry axes of the chains — 0.77 ± 0.06 nm have been recently observed[3] by atomic force microscopy (AFM) on the surface of a C_{60} sample synthesized at 9.5 GPa and 673 K. Since the centers of monomers in polymer chains consisting of icosahedral (I_h) fullerenes C_{60}, joined to one another by four-member $2+2$ cycles, are separated by 0.91–92 nm,[4,5] to explain their results the authors of Ref. 3 proposed the following model of polycondensation: When two C_{60} fullerenes interact, one loses five (or six) atoms from a cycle, while the fragment formed $C_{55(54)}$ attaches to the atoms of a five-member (or six-member) cycle of another C_{60}, so that these atoms become saturated — sp^3 hybridized. In Ref. 3 it was conjectured that the interunit distances in such a linear chain will equal 0.67 or 0.65 nm. However, these estimates were made using the well-known geometry of C_{60} fullerenes,[4] neglecting distortions of the angles and the lengths of the carbon bonds in the fullerene unit $C_{55(54)}$.

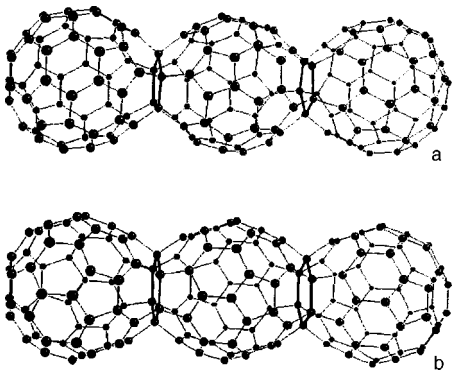

FIG. 1. Structure of ''polycondensed'' pseudotrimers C_{170} (a) and C_{168} (b). The thick lines distinguish five- and six-member cycles of sp^3 atoms.

We calculated the pseudotrimers C_{168} and C_{170} by the MM2 method (Fig. 1) and discovered that the inner $C_{55(54)}$ fragment is elongated along the chain axis x and its size is $D_x = 0.76$ (and 0.74) nm, respectively. Since the transverse diameter of this fragment equals $D_y = 0.66$ (and 0.67) nm, in the presence of a van der Waals (vdW) interaction the centers of the monomers standing opposite one another in neighboring polycondensed chains should be separated by at least 1 nm (we assume that the distance between the nearest-neighbor atoms in neighboring molecules equals 0.3 nm in the presence of a vdW interaction, i.e., the same as in ordinary C_{60} fullerite[4]), while in the case of 2+2 cycloaddition the separation is ≈ 0.9 nm, which likewise does not agree with experiment.[3] Moreover, by rotating two chains $(C_{55(54)})n$ with parallel symmetry axes it is impossible to find a position for which the pentagonal (or hexagonal) faces in the units of neighboring chains are parallel. For this reason, it is impossible to obtain a two-dimensional (2D) structure by ''polycondensation'' of these chains with the removal of another five or six atoms from the $C_{55(54)}$ unit. For the same reason, it is difficult to model a three-dimensional (3D) ''polycondensed'' structure with the removal of another five or six atoms from the $C_{50(48)}$ unit. We also note that mass-spectrometric data for the samples[3] show that the C_{60} carbon core remains as their structural unit. The arguments listed above show the inadequacy of the polycondensation model for the interpretation of the observations made in Ref. 3.

In the present letter we propose a different description of the unusual C_{60} structures,[3] based on a transformation of the spherical C_{60} molecules into ''barrels'' and the polymerization of the latter. Structures consisting of fullerenes (Fig. 1) and barrelenes (Figs. 2, 3, and 4) were calculated by the method of molecular mechanics (MM2) using the ALCHEMY code.

We note that C_{60} molecules elastically deform at room temperature and pressures $P \cong 10$ GPa. They undergo polymerization only when a sample is heated ($T > 400$ K) and held under such critical conditions.[1–3] On account of the polycrystalline nature of the sample the pressure acting on each fullerite microcrystal is most likely nonhydrostatic. Under further heating and rapid cooling the C_{60} molecules themselves undergo reorientation and isomerization and new metastable structures are formed.

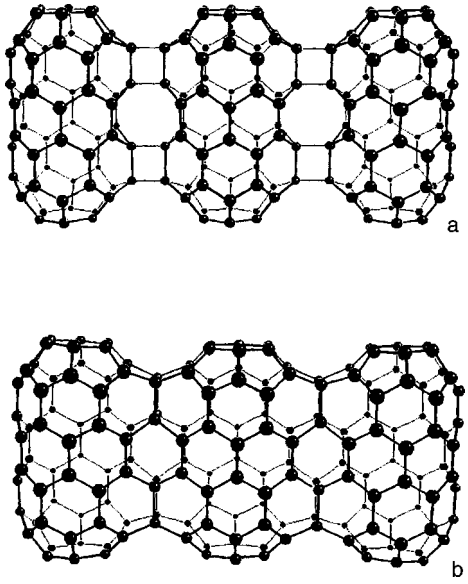

FIG. 2. Structures of linear trimers consisting of C_{60} barrelenes with type-*A* bonding (a) and type-*O* bonding (b).

BARRELENE CHAINS

We assume that in the process of predominantly ''ring'' compression of a cylindrical sample[3] and subsequent annealing an icosahedral fullerene transforms into a barrelene:[6,7] a rearrangement of only six atoms in the C_{60} framework, in which process six pentagons surround one vertex hexagon and six other pentagons surround the opposite hexagon, forming in the gap a cylindrical graphene fragment 0.47 nm in diameter. On account of the large curvature, which results in valence angles close to the case of sp^3 atoms, barrelenes undergo polymerization under the same conditions.[3] In what follows we shall calculate several characteristic types of joinings of barrelenes that give geometric parameters for the structures that are acceptable for explaining the results obtained in Ref. 3. We shall model mainly the polymerization of C_{60} in a layer where the barrelenes lie on the same level next to one another with the same orientation of their axes along the normal **z**, as the experiment of Ref. 3 indicates.

The simplest method of joining barrelenes into a chain — a type *A* bond — can be achieved with two 2+2 cycloadditions with the participation of two C–C bonds on the generatrices of the graphene fragment of each barrelene (Fig. 2a). Linear trimers, tetramers, and polymers can be constructed in this manner. The following parameters of the central part of a trimer correspond to a type *A* bond: $D_y = 0.421$ nm — transverse diameter, $D_x = 0.593$ nm — longitudinal diameter, $h = 0.906$ nm — height of the framework (in the direction of the **z** axis), $p = 0.745$ nm — longitudinal size of a unit that can be used to estimate the period of the polymer chain; the bond lengths in four-member cycles $d_z = 0.158$ nm and $d_{x1(x2)} = 0.152$ (0.155) are close to the analogous values in a dimer consisting of 2+2 joined fullerenes.[4,5] Here a barrelene flattens under polymerization conditions. When the vdW interaction is taken into account, the symmetry axes of iden-

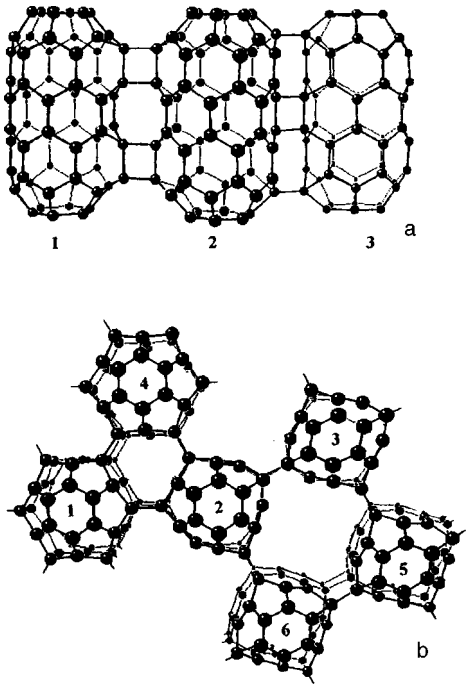

FIG. 3. Structures consisting of barrelenes with two types of bonding between monomers: (a) front view of trimer 1–2–3 with a ''kink''; (b) top view of a cluster of barrelenes: the trimer 1–2–3 with a ~30° ''kink,'' the triangle consisting of the molecules 1–2–4 is part of a triangular 2D lattice, the rectangle consisting of the barrelenes 2–3–5–6 is the unit cell of a rectangular structure, the cluster of barrelenes 1–2–3–6 is a three-ray ''star.''

tically oriented neighboring *A* chains are separated by a distance of 0.72 nm.

Under additional compression isomerization can occur in type-*A* oligomer structures. As a result, four-member cycles lying in the *xz* plane transfer into a perpendicular plane (Fig. 2b). Such isomerization is accompanied by a local rearrangement of the structure of a cluster, as a result of which the centers of neighboring monomers move closer to one another. A bond of a similar type (type *O*), studied by Osawa *et al.*[8] for a dimer consisting of C_{60} fullerenes, turned out to be energetically more favorable than the type-*A* bond. A calculation gives the following parameters of the central part *O* of a barrelene trimer (in nm): $D_y = 0.474$, $h = 0.894$, $p = 0.702$; the edge lengths in the rectangle — $d_z = 0.159$ and $d_y = 0.161$ — are close to the dimensions of the sp^3 rectangle in an *O* dimer consisting of fullerene ''balls.''[8] When the vdW interaction is taken into account, the distance between the symmetry axes of neighboring type-*O* chains will equal 0.77 nm.

As we have pointed out previously,[7] barrelenes can also join covalently through the atoms lying on the generatrix of a cylindrical fragment, including the vertex shared by a hexagon and two pentagons (joining of the barrelenes *2* and *3* in Fig. 3). Modeling and optimization of the geometry of a trimer consisting of barrelenes polymerized with such a type-*B* bond gives the following parameters of the central part (in nm): $D_y = 0.442$, $D_x = 0.560$, $h = 0.912$, and $p = 0.717$. The symmetry axes of the *B* chains consisting of

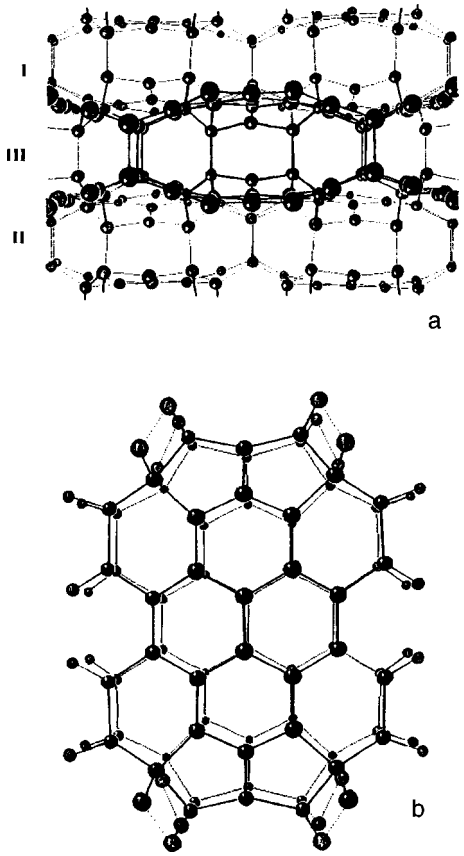

FIG. 4. Structure of 3D polymerized C_{60} barrelenes with a type-*O* bond within chains and a 2+2 bond between the lids of barrelenes in neighboring layers: (a) top view — chains I and II lie in the same layer while chain III lies in a neighboring layer; for clarity the barrelenes are represented in a cut-away view; (b) front view of the central barrelene in the chain III.

barrelenes standing opposite to one another, with the vdW interaction taken into account, will be separated by a distance of 0.74 nm.

Thus models of linear barrelene polymer chains of the types *A*, *O*, and *B* give geometric parameters that are very close to the observed distances (0.7–0.8 nm) between the centers of molecules in C_{60} polymer samples.[3]

We shall now consider models of the unusual formations, consisting of two, three, and more molecules, which are presented in Figs. 3 and 4 of Ref. 3 but which the authors unfortunately did not discuss.

BARRELENE DIMERS

A calculation of dimers consisting of barrelenes with type *A, B* and *O* bonds shows that in the last case the distance between the centers (0.63 nm) is shorter than in the *A* and *B* dimers (0.69 and 0.67 nm). We also calculated the geometry of an O' dimer in which one of the monomers is displaced in the **z** direction by $0.5h$. In such a dimer a type-*O*

bonding with the formation of one saturated four-member cycle, connecting the lower half of one barrelene with the upper half of another, is realized. Here the distance 0.57 nm between the centers of the projections of the barrelenes on the xy plane was found to be even shorter. We explain the presence of paired molecules whose centers are separated by a distance $\leqslant 0.6$ nm in Figs. 3 (at the center) and 4 (in the corner regions) of Ref. 3 by the presence of O and O' dimers.

TWO-DIMENSIONAL FORMATIONS

One can see in the same figures in Ref. 3 that at some locations the molecular chains change direction by an angle 17–35°, while at other locations the chains branch or break, and star- or triangular-shaped formations consisting of molecules whose centers are separated by $\leqslant 0.8$ nm are observed to form at the ends of some chains. A $\sim 30°$ kink in a linear chain could be due to a different type of bonding (A and B) between three successive monomers (units) in a chain — see the cluster with the molecules 1–2–3 in Fig. 3. The appearance of a $\sim 90°$ kink in a chain can also be explained similarly — a cluster consisting of the barrelenes 2–3–5 in Fig. 3a, where the distance between the centers of the molecules 3 and 5 equals 0.69 nm. Rotation of a chain by $\sim 60°$ can occur when the molecules join by a bond of the same type as in the main linear chain — see, for example, the type-A joining of barrelenes 1–2–6 in Fig. 3a. All this shows that a barrelene can join with covalently bonded neighbors into a molecular cluster, forming, for example, a ''star'' with three rays. We note that a three-ray ''star,'' geometrically very close to the cluster of molecules 1–2–3–6 in Fig. 3b, can be seen at the upper left corner of the AFM image of a C_{60} sample in Fig. 3 of Ref. 3.

Three barrelenes can join to form a right triangle with the same type of bond, for example, the molecules 1–2–4 with a type-A bond in Fig. 3b, where the distance a between the centers of these barrelenes equals 0.69 nm (0.63 nm with a type-O bond, 0.67 nm with a type-B bond). Similar triangular joinings of molecules with $a \approx 0.7$ nm can be seen at the lower right in Fig. 4 of Ref. 3 — the authors did not call attention to this fact, apparently because it is impossible to construct such a triangle on the basis of their model of fullerene bonds ''according to a general hexagon or pentagon.'' In our model it is possible to form a 2D layer with a triangular (or orthorhombic) unit cell, similar to the orthorhombic 2D polymer structure consisting of C_{60} fullerenes,[5] but with a higher density: one molecule per ≈ 0.42 nm^2.

Covalent joining of four barrelenes at an angle of 90° (the cluster consisting of the molecules 2–3–5–6 in Fig. 3a) results in the formation of a rectangle consisting of molecules whose centers are separated by distances a, $b = 0.69$, 0.73 (nm), and therefore it is possible to form a 2D rectangular lattice with one molecule per 0.50 nm^2.

3D BARRELENE STRUCTURES

Under the action of pressure and temperature C_{60} molecules can form under the conditions of Ref. 3 the following structures consisting of 1D, 2D, and 3D polymers:

a) Van der Waals coupling of layers of an orthorhombic 2D polymer lattice (consisting of triangularly joined barrelenes with parameter ≈ 0.7 nm) forms a crystal with a body-centered (BC) orthorhombic cell with parameter $c \equiv 2h' = 2.22$ nm. The density ρ of such a material, 2.6 g/cm^3, is close to that of the samples in Ref. 3. When the same layers join by sp^3 bonds (with three 2+2 bonds per barrelene ''lid''; see Ref. 9 for a

more detailed discussion) with a corresponding change in the parameter $c \equiv 2h'' = 2.06$ nm, the volume per molecule will equal 0.386 nm^3. The density of such a material, 3.1 g/cm^3, is close to that very hard fullerites.[1,2]

b) The molecular interaction between layers of polymer barrelenes with a 2D rectangular lattice produces a structure with a body-centered orthorhombic cell (parameters: a, b, $c = 0.69$, 0.73, 2.06 nm), $\rho = 2.3$ g/cm^3.

c) In the case when barrelenes polymerize in linear chains of the type A (or B) with a vdW interaction between the chains in both the layer and between the layers themselves, a structure with a body-centered orthorhombic cell (parameters: a,b, $c = 0.74(0.72)$, 0.72(0.74), 2.2 nm) forms. Such a structure, formed from fcc fullerite cells, will have a density of 2.3 g/cm^3.

d) We assume that if the pressure and temperature gradients are small in a distinguished volume of a microcrystal, then under the conditions of Ref. 3 the layers consisting of barrelene chains can bond covalently with one another and form a structure consisting of 3D C_{60} polymers. Figure 4 shows one possible scheme for such joining — a model of three type-O chains calculated by the MM2 method (compare Fig. 2b). Here each barrelene in one layer is coupled by 2+2 bonds with the ''lids'' of four molecules from a neighboring layer with the same type-O chains, so that 24 of the 60 atoms in it have diamond-like sp^3 bonds (Fig. 4b). The appearance of such bonds at the vertices of barrelenes in neighboring layers results in a reduction of the distance between the chains within a layer and in greater flattening of the barrelene ($D_y = 0.33$ nm) than in a separate type-O chain of the structure (c). The structure consisting of repeating layers has a body-centered orthorhombic cell (a, b, $c = 0.72$, 0.63, 1.98) with density 2.6 g/cm^3, close to the value 2.6 ± 0.2 g/cm^3 for the samples in Ref. 3. It contains purely graphite fragments, periodically arranged and connected with one another by sp^3 bonds. For this reason, such a structure can be interpreted as a pseudographite structure with period $b = 0.63$ nm, observed in the x-ray crystallographic analysis of the samples.[3]

In the present work structures of polymerized C_{60} barrelenes were modeled in order to explain the unusual C_{60} samples[3] subjected to high pressures and temperatures. A wide diversity of sp^3 joinings of barrelenes, including 2D and 3D polymer structures of high density, was presented (tables of the positions of the atoms in the structure studied can be obtained from the authors). Not only the formation of the characteristic linear chains of C_{60} but also clusters of two, three, and four molecules with dimensions that are not compatible with the geometric parameters of known models of fullerene polymers[1–5] were explained on the basis of the model.

This work was supported by the Russian Fund for Fundamental Research under Grant 96-02-18445 and the Japanese Society for Assistance to Science and the Russian State Program ''Fullerenes and Atomic Clusters'' under Project 98-061.

[a)]e-mail: cherno@sky.chph.ras.ru

[1] V. D. Blank, S. G. Buga, N. R. Serebryanaya *et al.*, Phys. Lett. A **205**, 208 (1995).
[2] V. V. Brazhkin, A. G. Lyapin, Yu. V. Antonov *et al.*, JETP Lett. **62**, 350 (1995).
[3] V. A. Davydov, L. S. Kashevarova, A. V. Rakhmanina *et al.*, JETP Lett. **63**, 818 (1996).
[4] M. S. Dresselhaus, G. Dresselhaus, and P. C. Eklund, *Science of Fullerenes and Carbon Nanotubes*, Academic Press, San Diego, 1996.

[5] A. M. Rao, P. S. Eklund, U. D. Venkateswaran *et al.*, Appl. Phys. A **64**, 231 (1997).
[6] L. A. Chernozatonskii, Phys. Lett. A **160**, 392 (1991).
[7] L. A. Chernozatonskii, Chem. Phys. Lett. **209**, 229 (1993).
[8] Sh. Osawa, E. Osawa, and Yu. Hirose, Fullerene Sci. Technol. **3**, 565 (1995).
[9] L. A. Chernozatonskii, E. G. Galpern, and I. V. Stankevich, Chem. Phys. Lett. (1998) in press.

Translated by M. E. Alferieff

Fractal structure of fullerite

I. V. Zolotukhin,[a)] L. I. Yanchenko, and E. K. Belonogov
Voronezh State Technical University, 394026 Voronezh, Russia

(Submitted 7 April 1998)
Pis'ma Zh. Éksp. Teor. Fiz. **67**, No. 9, 684–685 (10 May 1998)

We have obtained macroscopic fractal aggregates of fullerite ranging in size from 100 to 400 μm. The fractal structure of fullerite is formed by microscopic (30–100 nm) fullerite crystals in the presence of a temperature gradient under conditions of diffusion-limited aggregation.
 [S0021-3640(98)01409-1]

PACS numbers: 81.05.Tp, 61.43.Hv, 61.48.+c

Fractal structures of different substances have attracted universal interest in recent years as objects with unusual physical properties. From this point of view a new modification of carbon is attracting attention — fullerite, whose crystal structure (fcc) consists of C_{60} carbon molecules. Ordinarily, polycrystalline fullerite is produced by evaporating nonpolar solvents (benzene, toluene, CS_2, and so on) containing C_{60} molecules. To form a fractal structure of fullerite it is necessary to create nonequilibrium conditions and make it possible for the particles formed to execute a random walk. To this end a saturated solution of an 85:15 mixture of C_{60} and C_{70} in toluene (solubility 2.8 mg/cm^3) was heated to 100 °C. A polished silicon wafer with asperities not exceeding 10 nm in height was submerged in the heated solution. The formation of fractal structures of fullerite occurred as the solution of fullerenes in toluene cooled for 1–1.5 h. Next the silicon wafer was removed from the solution, and after the toluene evaporated the structure of the residue was examined under an MIM-7 optical microscope.

The pictures of the residues are presented in Fig. 1. Well-formed macroscopic fractal aggregates, ranging in size from 100 to 400 μm with height $\sim$20 μm at the center and decreasing toward the edges, can be clearly seen. The fractal dimension D determined by the grid method was found to be $D=1.5$–1.75 for different fractal aggregates. Fractal aggregates of fullerite of a similar type and size were also obtained on a freshly cleaved surface of phlogopite, single-crystal graphite, and polished aluminum foil.

To determine the microscopic structure of the fractal aggregates obtained, fractals were grown by the method described above on a copper mesh, serving as the object-holder in an electron microscope. The results of the electron-microscopic investigation of fractal structures of fullerite in transmission and in diffraction are displayed in Fig. 2.

The point electron diffraction pattern corresponds to a material with an fcc lattice and parameter $a=1.4\pm0.1$ nm, i.e., C_{60} fullerite. The presence of C_{70} fullerite was not observed. This could be due to the fact that the solution reaches saturation with respect to the C_{60} component much earlier than with respect to C_{70}. For this reason, crystallization of C_{60} in the form of a separate phase occurs in the initial stages. One can see from the

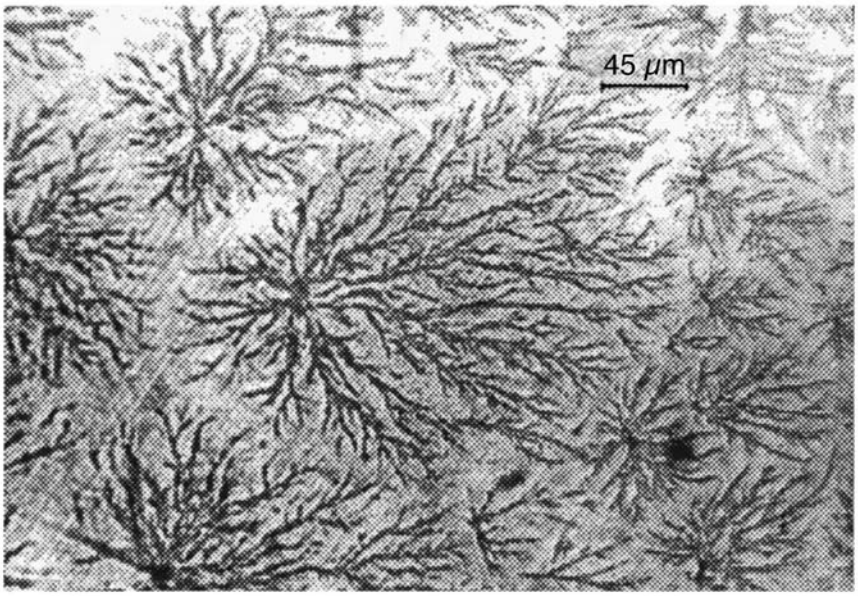

FIG. 1. Fractal structure of fullerite.

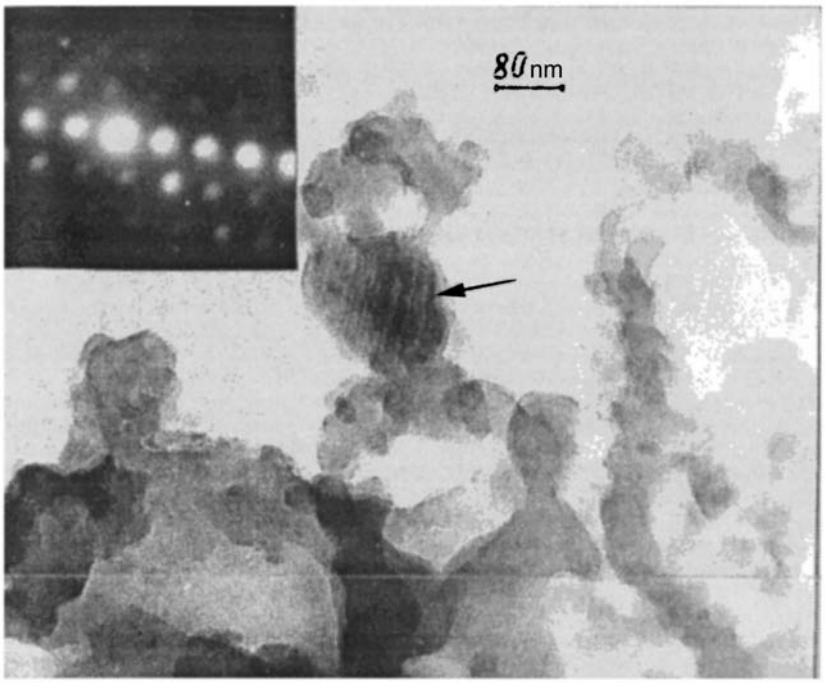

FIG. 2. Microstructure and electron diffraction pattern of C_{60}.

picture obtained in transmission that the fractal structure of fullerite is a spatial structure and consists of small crystals ranging in size from 30 to 100 nm. Twins with a [111] twinning boundary are resolved on the large crystal formation marked by the arrow. Pores ranging in size from 30 to 120 nm are also seen. Therefore the fractal aggregates are formed from fullerite crystals. We can say the following about the mechanism leading to the formation of a fractal structure of fullerite. It is well known[1,2] that the solubility of C_{60} in toluene decreases severalfold as temperature increases to 100 °C. For this reason fullerite crystals precipitate from the supersaturated solution of fullerenes in toluene and undergo Brownian motion in the volume of the liquid, i.e., a colloidal suspension, where solid particles suspended in the liquid do not settle under the action of gravity, forms. When the substrate or vessel wall is reached in the presence of a temperature gradient, the diffusion-limited aggregation mechanism is realized,[3] leading to the formation of fractal structures of fullerite on the surface of smooth substrates.

In closing, we thank V. N. Bezmel'nitsyn for providing the fullerenes.

[a)]e-mail: paul@zolot.vrn.ru

---

[1] R. S. Ruoff *et al.*, J. Phys. Chem. **97**, 379 (1993).
[2] V. N. Bezmel'nitsyn, A. V. Eletskiĭ, M. V. Okun', and E. V. Stepanov, Izv. Ross. Akad. Nauk, Ser. Khim. **60**, No. 9, 18 (1996).
[3] S. R. Forrest and T. A. Witten, J. Phys. A: Math. Gen. **12**, L109 (1979).

Translated by M. E. Alferieff

Ferromagnetic liquid droplets

A. N. Grigorenko, P. I. Nikitin, V. I. Konov, and A. M. Ghorbanzadeh
General Physics Institute, Russian Academy of Sciences, 117942 Moscow, Russia

M.-L. Degiorgi, A. Perrone, and A. Zocco
Universitá di Lecce, Dipartimento di Fisica, Istituto Nazionale Fisica della Materia, CP 193, 73100 Lecce, Italy

(Submitted 7 April 1998)
Pis'ma Zh. Éksp. Teor. Fiz. **67**, No. 9, 686–689 (10 May 1998)

Experimental evidence for ferromagnetic behavior of liquid droplets produced by laser ablation from amorphous alloys is presented for the first time. Thin films of amorphous magnetic materials are fabricated by a laser deposition technique in the presence and in the absence of magnetic field. The differences in the parameters of deposited films are attributed to the ferromagnetic properties of small liquid droplets. [S0021-3640(98)01509-6]

PACS numbers: 75.50.Kj, 75.50.Mm

The exchange energy is typically smaller than the energy of direct Coulomb interactions of ions, and for this reason the liquid state of a ferromagnetic material cannot be ferromagnetic. A metastable ferromagnetic liquid can be produced by supercooling of a ferromagnetic material to a temperature lower than the Curie temperature.[1] More interesting is another possibility which comes from the facts that the melting temperature of a particle decreases strongly with decreasing particle size for small particles,[2] while the Curie temperature shows only a slight variation with the change in particle size.[3] Thus sufficiently small liquid particles of a ferromagnetic material with Curie temperature close to the melting temperature should be ferromagnetic. Here we present experimental evidence in favor of ferromagnetic behavior of liquid droplets produced during the laser ablation[4] of amorphous magnetic materials in the presence of a magnet.

The experimental installation and procedures are described in detail in Ref. 5. We deposited amorphous ribbons of the atomic composition $Fe_{67}Co_{18}Si_1B_{14}$ and a bulk amorphous material of the composition $Fe_{4.35}Co_{68.15}Si_{12.5}B_{15}$ by means of a laser ablation technique. The deposition was done in a vacuum of about 10^{-7} mbar on *p*-type silicon substrates of the (100) orientation. Two samples were produced during each deposition cycle: one was deposited on the substrate with a strong magnet placed behind the substrate, and the other was deposited without the magnet. The magnet axis was perpendicular to the substrate surface. A distance of 15 cm separated the two samples and the magnet did not affect the deposition of the second sample.

The samples were analyzed by scanning electron microscopy, Auger electron spectroscopy, profilometry, and magnetometry. An ensemble of droplets produced during laser ablation[4] was detected at the surface of the deposited films. The droplets were

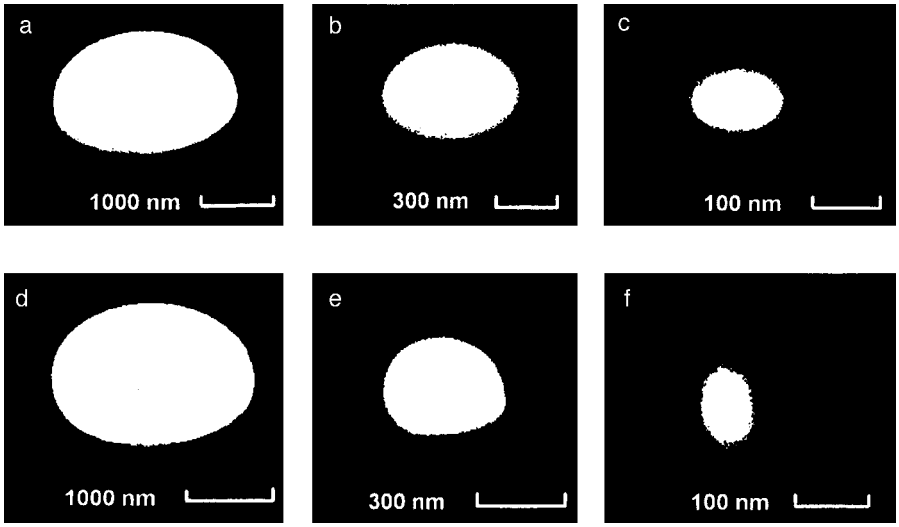

FIG. 1. Scanning electron images of the film surface with droplets of different sizes investigated under the flat angle of 45°: a—c were taken for the sample produced without the magnet, d—f were measured for the sample fabricated with the magnet. The images contrast is high in order to emphasize the droplet contours.

distributed with a concentration of 10^4-10^6 cm^{-2} and a size range from several tens of nanometers up to several micrometers. The droplet composition was close to that of the film.

We found interesting peculiarities of the droplet shape. The shape of the droplets on films deposited without the magnet did not change with reduction of the droplet size, while the shape of the droplets produced in the presence of the magnet showed a strong size dependence. Droplets having dimensions smaller than some critical size were elongated in the direction of magnetic field, and the ratio of the droplet height h to the droplet diameter d (an aspect ratio) increased from a value of 0.1 for large droplets (evaluated by means of profilometry) to a value of 1–2 for small droplets (measured by electron microscopy). Figure 1 shows three typical pairs of droplets of different sizes measured by means of a scanning electron microscope. Images a–c correspond to the sample prepared without the magnet, and d–f correspond to the sample deposited in the presence of the magnet. In order to evaluate the ratio of the droplet height to the droplet diameter, these images were taken at an angle of 45° relative to the substrate surface (see Fig. 2; the droplet images measured at normal incidence of the electron beam were circles). Figure 2 demonstrates how the aspect ratio (>0.22) can be evaluated from the inclined droplet images. For droplets with small aspect ratios the projection image should be an ellipse with axes in the ratio 0.7. We observed this ratio for all droplets on the films produced without the magnet and for large droplets on the films deposited with the magnet. However, the axis ratios of the projection image of small droplets (with projection diameter smaller than 300 nm) on the films deposited with the magnet were greater than 0.7. Then, simple geometry indicates that the ratio of the droplet height to the diameter for small droplets is much higher than that of large droplets. The aspect ratio for the droplet e, with

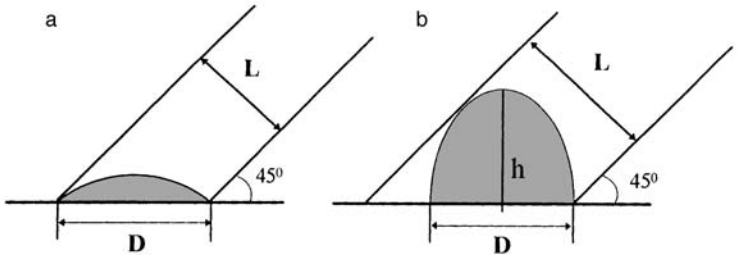

FIG. 2. Schematic diagrams of measurements of the droplet aspect ratio: a—a droplet with a small ratio of the droplet height to diameter, b—a droplet with a high ratio of the droplet height to diameter.

a diameter of 300 nm, can be evaluated as roughly 0.7, and for the droplet f, with a diameter of 70 nm, as 1.5.

The ferromagnetic nature of small droplets is the most probable explanation for the observed change of the droplet shape. It is clear that a minimum of the magnetic energy of a ferromagnetic droplet placed in high, uniform magnetic field requires a high aspect ratio, while a minimum of the surface energy results in a small aspect ratio, which is governed by surface energies. The higher the droplet magnetization, the higher the aspect ratio will be. The fact that all the droplets studied have a circular projection on the surface (the large droplets were sphere segments) means that they were liquid when they became ferromagnetic. The ferromagnetic properties of the droplets can be explained by the size dependence of the melting temperature or/and supercooling of droplets. The melting temperature of a particle can be estimated from a comparison of the surface and volume energies as

$$T = T_{mb} - C\,\frac{\sigma_s - \sigma_l}{(c_s - c_l)\rho h}, \tag{1}$$

where T_{mb} is the melting temperature of the bulk, C is the constant which depends upon the particle geometry and reflects the surface-to-volume dimensionless ratio, σ_s and σ_l are surface energies of solid and liquid states respectively, c_s and c_l are the heat capacities of the solid and liquid states, ρ is the density of the material, and h is the characteristic particle size. For example, for flat cobalt droplets the values are as follows: $\Delta c = c_s - c_l = 10^5$ erg/g·K, $\Delta\sigma = \sigma_s - \sigma_l = 200$ erg/cm^2, $\rho = 8.9$ g/cm^3, the droplet height is the characteristic particle size, and the coefficient $C = 4$. Taking $h = 20$ nm, we get for $\Delta T = T_{mb} - T = 300$ K, which is close to the difference between the Curie temperature $T_c = 1388$ K and the bulk melting temperature $T_{mb} = 1765$ K of cobalt ($T_{mb} - T_c = 377$ K). Another piece of evidence in favor of size dependence of the melting temperature is the fact that smaller droplets manifest greater magnetic properties (higher aspect ratios). Indeed, the magnetization near the Curie temperature depends strongly upon the temperature. A droplet of a smaller size has a lower melting temperature, which results in higher magnetization.

To check the ferromagnetic nature of small droplets we performed a test deposition of the amorphous bulk material with the magnet axis parallel to the substrate and the magnet placed behind the substrate at a distance of 1 cm from its center. As a result, an in-plane magnetic field was generated at the surface and a deflection force acted on the

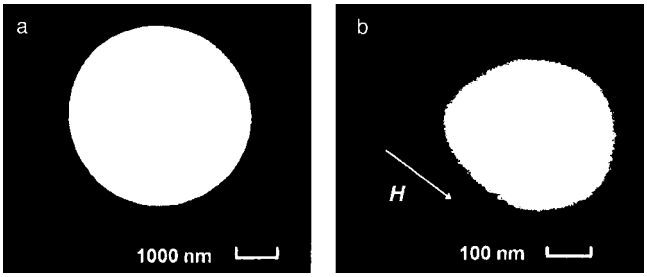

FIG. 3. Scanning electron images of droplets taken at normal incidence of the electron beam on a film deposited in the presence of an in-plane magnetic field **H**: a—large droplet, b—small droplet.

magnetic particles. We found no deviation of droplets in respect to the position of the deposition spot. That means that the droplets had a temperature higher than the Curie temperature during the flight from the target to the substrate and acquired magnetic properties at the substrate surface. Again we observed a difference in the shape of large and small droplets. Figure 3 shows electron micrographs of two droplets of different sizes (the film surface was perpendicular to the electron beam). The large droplet (a) has a circular form, meanwhile the small droplet (b) has a form close to that of an ellipse with the major axis along the direction of the in-plane magnetic field. Such a form should be expected for a droplet that becomes ferromagnetic in a molten state during the process of cooling.

In conclusion, the changes of the shape of the droplets produced by laser ablation of amorphous alloys in the presence of a magnetic field are strong evidence in favor of the fact that we have observed for the first time a ferromagnetic liquid state of laser-ablated small droplets of a ferromagnetic material. This liquid ferromagnetic state can arise due to size dependence of the melting temperature of small objects and due to droplet supercooling. The effect discovered may be useful for the production of magnetic nanoobjects and quantum dots.

The authors thank Dmitriy Kolmykov for the help with electron microscopy measurements. The work was supported by NATO Linkage Grant and Russian Fund for Fundamental Research Grants (No. 18956 and No 19608). The authors acknowledge the support of the Istituto Nazionale Fisica della Materia.

[1] A. Inoue and A. Katsuya, Jpn. J.: Mat. Trans. JIM **37**, 1332 (1996).
[2] P. M. Ajayan and L. D. Marks, Phys. Rev. Lett. **63**, 279 (1989).
[3] M. Godinho, J. L. Dormann, M. Nogues *et al.*, J. Magn. Magn. Mater. **144**, 369 (1995).
[4] G. Koren, A. Gupta, R. J. Baseman *et al.*, Appl. Phys. Lett. **55**, 2450 (1989).
[5] P. I. Nikitin, A. A. Beloglazov, A. Yu. Toporov *et al.*, J. Appl. Phys. **82**, 1408 (1997).

Published in English in the original Russian journal. Edited by Steve Torstveit.

Ferromagnetic resonance in multilayer $[Fe/Cr]_n$ structures with noncollinear magnetic ordering

A. B. Drovosekov, N. M. Kreĭnes, and D. I. Kholin
P. L. Kapitsa Institute of Physical Problems, Russian Academy of Sciences, 117334 Moscow, Russia

V. F. Meshcheryakov
Moscow Institute of Radio Engineering, Electronics, and Automatics, 117464 Moscow, Russia

M. A. Milyaev, L. N. Romashev, and V. V. Ustinov
Institute of Metal Physics, Urals Branch of the Russian Academy of Sciences, 620219 Ekaterinburg, Russia

(Submitted 7 April 1998)
Pis'ma Zh. Éksp. Teor. Fiz. **67**, No. 9, 690–695 (10 May 1998)

The excitation spectrum in an $[Fe/Cr]_n$ multilayer structure with noncollinear magnetic ordering was studied by the ferromagnetic resonance (FMR) method in the frequency interval 9.5–37 GHz at room temperature. Besides an acoustic branch, several additional modes were observed under parallel excitation of resonance. The FMR spectrum was calculated analytically in a biquadratic exchange model, neglecting in-plane anisotropy, for an infinite number of layers in the structure and numerically for a finite number of layers contained in real samples. It was shown that the observed modes correspond to excitation of standing spin waves with wave vectors perpendicular to the film plane. [S0021-3640(98)01609-0]

PACS numbers: 76.50.+g, 75.70.Cn, 75.60.Ej

It is now known that neighboring ferromagnetic layers in multilayer structures (including trilayers, called sandwiches) with a nonferromagnetic interlayer can assume collinear ordering — ferromagnetic or antiferromagnetic[1] — and noncollinear ordering, in which case in the absence of an external magnetic field the angle between the magnetizations of neighboring layers is different from both 0° and 180°.[2–5] It has been shown that the collinear magnetic ordering of such superlattices can be described well in most cases by the standard bilinear exchange interaction J_1, whose magnitude oscillates as the thickness of the nonferromagnetic interlayer increases. The discovery of noncollinear ordering has made it necessary to take into account the biquadratic exchange interaction J_2 in the expression for the magnetic energy of a multilayer structure.[2] Although quite a large number of theoretical works have been devoted to describing such noncollinear structures (see Refs. 6 and 7), the questions of the origin of biquadratic exchange and the possibility of describing the interaction of magnetic layers in multilayer magnetic films in terms of J_1 and J_2 remain open. In this connection it is of great interest to study superlattices with noncollinear magnetic ordering.

Ferromagnetic resonance (FMR) is an effective and quite simple experimental method of investigating magnetic superlattices. This method has been repeatedly used by different groups (see references cited in Ref. 8) to study multilayer magnetic structures (mainly sandwiches). In most cases the experimental data obtained were discussed with only the bilinear exchange taken into account. A calculation of the FMR spectrum for trilayer samples in the biquadratic exchange model was performed in Refs. 9–13. It was shown that the form of the optical branch of the oscillations depends substantially on J_1 and J_2, but the number of experimental works where J_2 was sufficiently large and was taken into account in the analysis of the spectra is very limited.[13] We note that the biquadratic exchange model was also used in Refs. 13–16 to describe the Brillouin scattering spectra in sandwiches.

In the present work we investigated experimentally the magnetization curves and FMR spectra of an $[Fe/Cr]_n$ multilayer structure with noncollinear magnetic ordering in a wide range of frequencies and magnetic fields. The spectrum of a multilayer magnetic structure was calculated in a biquadratic exchange model. The results of static and resonance measurements are compared on the basis of the model employed.

The measurements of FMR and the static magnetic properties were performed on two samples: S9 — $[Cr(10.4\ Å)/Fe(21.2\ Å)]_{12}$ and S14 — $[Cr(7.7\ Å)/Fe(33.2\ Å)]_{16}$ grown in a ''Katun' S'' molecular-beam epitaxy system. The substrates consisted of single-crystal MgO plates cut parallel to the (100) plane. Sample quality was monitored and the Fe and Cr layer thicknesses were determined using small-angle x-ray diffraction and x-ray spectral microanalysis (the method is described in Ref. 17). According to the data obtained, the crystallographic orientation of the iron and chromium layers is identical to that of the substrate. Three Bragg peaks from the Fe/Cr superlattice can be clearly seen in the small-angle x-ray diffraction spectrum. This attests to the good quality of the samples and sharp interfaces between the layers.

The magnetic structure of the samples was determined on the basis of their magnetization curves. The measurements were performed with a vibrating-coil magnetometer at room temperature in two field orientations: parallel (up to 17 kOe) and perpendicular (up to 9 kOe) to the film plane. The in-plane field was applied along the hard crystallographic axis [110] of the iron layers. Figure 1 shows the projection M of the magnetization vector of the iron layer on the direction of the external static magnetic field **H** versus the intensity of the field H. The measurements performed in a field perpendicular to the sample plane show that in the absence of an external magnetic field the magnetizations of the iron layers lie in the film plane. The magnetization curves in a field parallel to the sample plane are characterized by a high remanent magnetization M_0 and continuous passage to a saturation value M_S, indicating the presence of noncollinear magnetic ordering in our superlattices. The angles $\varphi_0 = 2\ \cos^{-1}(M_0/M_S)$ of the initial ordering of the neighboring magnetic layers in samples S9 and S14, obtained from static measurements, are indicated on the plots in Fig. 1.

Ferromagnetic resonance was investigated at room temperature at frequencies ranging from 9.5 to 37 GHz in fields up to 10 kOe. The sample was placed at the bottom of a cylindrical resonant cavity in which the microwave modes H_{011}, H_{012}, and H_{013} were excited. A constant magnetic field was applied parallel to the sample plane along the [011] axis, just as for magnetization measurements. Excitation of resonance was either longitudinal or transverse, depending on the position of the sample at the bottom of the

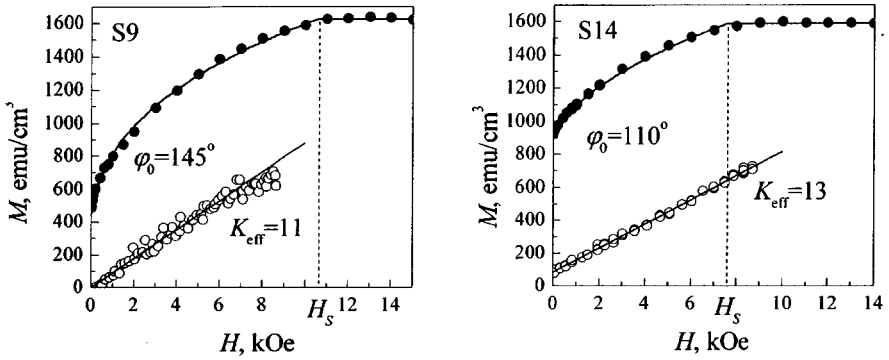

FIG. 1. Magnetization of the samples versus the magnetic field. Dots — experimental data (● — **H** parallel, ○ — **H** perpendicular to the sample plane). Curves — result of an analytical calculation, φ_0 — angle of initial ordering of neighboring magnetic layers.

cavity. Figure 2 shows examples of the experimental traces of the resonance lines for two orientations of the microwave field for sample S9. In the case of transverse pumping (curve *1*) only one branch, of high intensity, is observed. It corresponds to uniform precession of the magnetizations of all magnetic layers, as follows from a comparison with the calculations. In the case of longitudinal pumping (curve *2*) the intensity of this line is substantially weaker, but several additional modes are observed; in the figure their positions are marked by arrows. The results of the resonance measurements for two samples are presented in Fig. 3. The magnitude of the ''experimental errors'' shown in the plots corresponds to the distance between the maximum and minimum of the derivative of the microwave power absorption in the sample. In most cases the center of the line is determined with an accuracy that is several times better. The FMR spectra obtained on different pieces of the initial film S9 were completely identical and did not depend on the shape of the sample.

To explain the nature of the series of modes that we observed with longitudinal excitation of resonance we performed an analytical calculation of the spectrum of spin

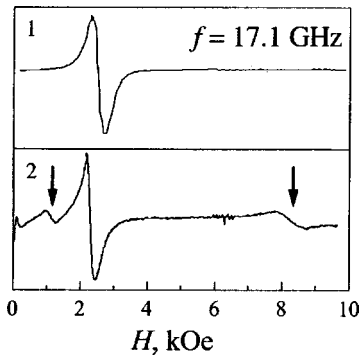

FIG. 2. Examples of traces of the resonance lines for sample S9 with transverse (curve *1*) and longitudinal (curve *2*) excitation of resonance. The scale along the ordinate for curve *1* is approximately 20 times larger than for curve *2*.

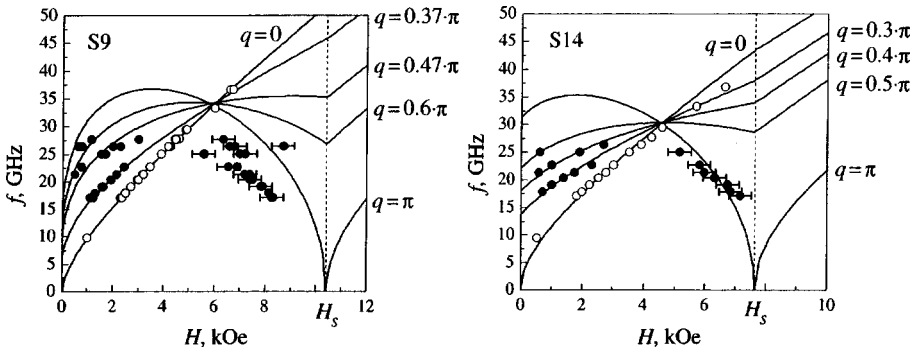

FIG. 3. FMR frequency versus the intensity of the external magnetic field for two samples. Dots — experiment (● — longitudinal, ○ — transverse excitation of resonance). Lines — result of analytical calculation.

waves with wave vectors perpendicular to the film plane for an infinite superlattice. The calculation was performed in the biquadratic exchange model for the case of an in-plane external magnetic field **H**. It was assumed that the magnetizations of all iron layers have the same magnitude M_S and that the magnetic moment of each layer precesses as a whole. A similar calculation was performed in Ref. 18 neglecting the external magnetic field. Neglecting the fourth-order anisotropy in the film plane[a)] and the possible anisotropy of the exchange constants J_1 and J_2, the magnetic part of the energy of an $[\mathrm{Fe/Cr}]_n$ multilayer structure per unit area of the film can be written as follows in the present model:

$$E=-d\sum_{i=1}^{n}(\mathbf{M}_i\cdot\mathbf{H})+\frac{J_1}{M_S^2}\sum_{i=1}^{n-1}(\mathbf{M}_i\cdot\mathbf{M}_{i+1})+\frac{J_2}{M_S^4}\sum_{i=1}^{n-1}(\mathbf{M}_i\cdot\mathbf{M}_{i+1})^2+d\frac{K_{\mathrm{eff}}}{2}\sum_{i=1}^{n}(\mathbf{M}_i\cdot\mathbf{z})^2, \tag{1}$$

where $\mathbf{M}_i$ is the magnetization of the ith iron layer, d is the thickness of the iron layer, K_{eff} is the effective surface anisotropy coefficient, and **z** is the normal to the film plane. The equilibrium value of the angle α_i between the magnetization of the ith layer and the direction of the external field **H** can be determined by minimizing the energy (1):

$$\alpha_i=(-1)^i\cos^{-1}(M/M_S).$$

The value of M can be determined as an implicit function of H:

$$\begin{cases} H=AM+BM^3 & \text{for} \quad H\leqslant H_S; \\ M=M_S & \text{for} \quad H>H_S. \end{cases} \tag{2}$$

Here $A=(4J_1-8J_2)/dM_S^2$, $B=16J_2/dM_S^4$, and $H_S=(4J_1+8J_2)/dM_S$ is the saturation field. To calculate the FMR frequencies we use the Landau–Lifshitz equation without the dissipative term:

$$\gamma^{-1}\dot{\mathbf{M}}_i=-\mathbf{M}_i\times\mathbf{H}_i^{\mathrm{eff}}, \quad \text{where} \quad \mathbf{H}_i^{\mathrm{eff}}=-(\partial E/\partial\mathbf{M}_i)d^{-1}. \tag{3}$$

The solution of the linearized equations (3) can be sought in the form of a traveling wave with frequency ω_q and constant phase shift q of the precession of the magnetizations of

neighboring iron layers, equal to the product of the wave vector by the superlattice period. Omitting the intermediate calculations, we present immediately the expression for the frequency $\omega_q(H)$ of the oscillations:

$$\left(\frac{\omega_q}{\gamma}\right)^2 = \begin{cases} [C(1+\cos q)+K_{\text{eff}}][CM^2(1+\cos q) \\ +(C+BM^2)(M_S^2-M^2)(1-\cos q)] \quad \text{for} \quad H \leqslant H_S, \\ \left(H-H_S\dfrac{1-\cos q}{2}\right)\left(H-H_S\dfrac{1-\cos q}{2}+K_{\text{eff}}M_S\right) \quad \text{for} \quad H>H_S, \end{cases} \tag{4}$$

where $C=(A+BM^2)/2$ (see explanations for Eq. (2)).

For $q=0$ we obtain an expression for the acoustic mode and for $q=\pi$ an expression for the optical mode, corresponding to the analogous formulas in Ref. 12. In the case $H=0$ formula (4) gives a spectrum that agrees, aside from notation, with Ref. 18. The computational results for the spectra are presented in Fig. 3 (solid curves). The values of the constants J_1, J_2, and M_S employed in constructing the curves $\omega_q(H)$ were obtained by fitting expressions (2) to the experimental magnetization curves in a field parallel to the film plane (see Fig. 1).

We present below the values of these constants:

$J_1=0.40$ ergs/cm^2, $J_2=0.23$ ergs/cm^2, $M_S=1.62\times10^3G$—for sample S9;

$J_1=0.22$ ergs/cm^2, $J_2=0.39$ ergs/cm^2, $M_S=1.59\times10^3G$—for sample S14.

The value of K_{eff} was determined from magnetization curves in a perpendicular field. According to the calculations of Ref. 12 these curves should possess a linear initial segment $M=H/K_{\text{eff}}$ (the values obtained for K_{eff} are given on the plots in Fig. 1). The solid curves in Fig. 3 show the optical mode ($q=\pi$), acoustic mode ($q=0$), and several modes with intermediate values of q, best describing the experimental data. The plots presented demonstrate qualitative agreement between calculations and experiment, while in the case of the sample S14 there is a definite quantitative agreement. This allows us to assert that the modes which we observed do indeed correspond to excitation of standing spin waves with wave vectors perpendicular to the film plane.

To take into account the effect on the FMR spectrum of having a finite number of layers in the sample, we performed a numerical calculation for systems containing specified numbers of iron layers. The results of such a calculation for sample S14 are presented in Fig. 4. The spectrum of the finite structure is quantitatively close to that of an infinite structure, though it has a number of characteristic features. The spectrum consists of a finite number of modes equal to the number of layers in the film. Some of the modes can be excited in fields less than the saturation field H_S only under conditions of longitudinal pumping (dashed curves) and some only under conditions of transverse pumping (solid curves). In fields exceeding H_S a uniform microwave field can excite only one mode, corresponding to precession of the magnetic moments of all iron layers as a whole (solid line). We note that the numerical calculation did not permit improving the agreement between the static and resonance measurements for sample S9.

In summary, a series of FMR modes, corresponding to excitation of standing spin waves with wave vectors perpendicular to the film plane, was observed in superlattices with noncollinear magnetic ordering. Analytical and numerical calculations of the FMR spectrum were performed for such structures in the biquadratic exchange model.

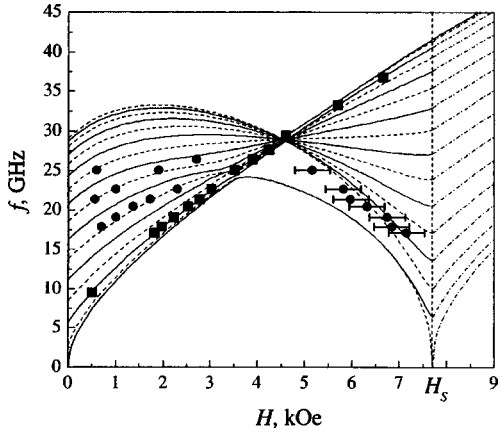

FIG. 4. FMR frequencies versus the constant magnetic field for sample S9. Lines — result of computer calculation taking into account a finite number of layers in the structure. Dots — experimental data (● — longitudinal, ■ — transverse excitation of resonance).

We wish to express our sincere appreciation to N. G. Bebenin and V. I. Marchenko for stimulating discussions. This work was supported by the Russian Fund for Fundamental Research under Grants 96-02-16687, 98-02-17517, and 98-02-16797 and by the U.S. Civilian Research & Development Foundation for the Independent States of the Former Soviet Union (CRDF) under Grant RP1-207. D. I. Kholin is grateful to Forschungszentrum Julich GmbH for financial support.

[a)]According to published data[13,14,16] the fourth-order anisotropy in iron films in Fe/Cr structures, in order of magnitude, is 500 Oe, which is much smaller than the exchange fields in our samples.

[1] P. Grünberg, R. Schreiber, Y. Pang *et al.*, Phys. Rev. Lett. **57**, 2442 (1986).
[2] P. Grünberg, S. O. Demokritov, A. Fuss *et al.*, J. Appl. Phys. **69**, pt. 2A, 4789 (1991).
[3] V. V. Ustinov, L. N. Romashev, V. I. Minin *et al.*, Fiz. Met. Metalloved. **80**(2), 71 (1995).
[4] A. Schreyer, J. F. Ankner, Th. Zeidler *et al.*, Phys. Rev. B **52**, 16066 (1995).
[5] V. V. Ustinov, N. G. Bebenin, L. N. Romashev *et al.*, Phys. Rev. B **54**, 15958 (1996).
[6] J. C. Slonczewski, Phys. Rev. Lett. **67**, 3172 (1991); J. Appl. Phys. **73**, pt. 2A, 5957 (1993); J. Magn. Magn. Mater. **150**, 13 (1995).
[7] S. O. Demokritov, E. Tsymbal, P. Grünberg *et al.*, Phys. Rev. B **49**, 720 (1994).
[8] P. E. Wigen and Z. Zhang, Braz. J. Phys. **22**, 267 (1992).
[9] M. Maccio, M. G. Pini, P. Politi, and A. Rettori, Phys. Rev. B **49**, 3283 (1994).
[10] N. G. Bebenin, A. V. Kobelev, A. P. Tankeev, and V. V. Ustinov, Fiz. Met. Metalloved. **82**(4), 39 (1996).
[11] N. G. Bebenin, A. V. Kobelev, A. P. Tankeyev, and V. V. Ustinov, J. Magn. Magn. Mater. **165**, 468 (1997).
[12] N. M. Kreines, A. N. Kolmogorov, and V. F. Mescheriakov, J. Magn. Magn. Mater. **177–181**, 1189 (1998).
[13] S. M. Rezende, C. Chesman, M. A. Lucena *et al.*, J. Magn. Magn. Mater. **177–181**, 1213 (1998).
[14] B. Heinrich and J. Cochran, Adv. Phys. **42**, 523 (1993).
[15] M. Grimsditch, S. Kumar, and E. Fullerton, Phys. Rev. B **54**, 3385 (1996).
[16] A. Azevedo, C. Chesman, M. Lucena *et al.*, J. Magn. Magn. Mater. **177–181**, 1177 (1998).
[17] V. V. Ustinov, T. P. Krinitsina, V. V. Popov *et al.*, Fiz. Met. Metalloved. **84**(4), 161 (1997).
[18] N. G. Bebenin and V. V. Ustinov, Fiz. Met. Metalloved. **84**(2), 29 (1997).

Translated by M. E. Alferieff

Characteristics of the process of reorientation of bipolar drops of a nematic with rigidly fixed poles

A. V. Shabanov, V. V. Presnyakov, V. Ya. Zyryanov,[a)] and S. Ya. Vetrov
L. V. Kirenskiĭ Institute of Physics, Siberian Branch of the Russian Academy of Sciences, 660036 Krasnoyarsk, Russia

(Submitted 7 April 1998)
Pis'ma Zh. Éksp. Teor. Fiz. **67**, No. 9, 696–700 (10 May 1998)

The director configuration in a bipolar drop of a nematic with rigidly fixed poles is calculated as a function of the electric field directed perpendicular to the symmetry axis of the drop. It is shown that the reorientation of the drop is a dual process: a threshold process in the region where the initial director orientation is orthogonal to the electric field, and a nonthreshold process elsewhere in the drop. A relation for determining the critical field is obtained. Experimental investigations of the characteristics of scattered light for a film of polymer-encapsulated liquid crystals confirm the computational results. © *1998 American Institute of Physics.* [S0021-3640(98)01709-5]

PACS numbers: 61.30.Gd

According to experimental and theoretical investigations[1–3] the reorientation of bipolar drops of a nematic liquid crystal (LC) under the action of an electric field directed perpendicular to the symmetry axis is a threshold, three-stage process. At low voltages no change was observed in the orientational structure of the drop. When the threshold field was reached, the poles of the drop started to move and the bipolar configuration of the director turned so that the symmetry axis was oriented along the field, if the dielectric-constant anisotropy of the LC is positive. Increasing the voltage further caused the director to line up with the field lines in the entire volume of the drop.[1,3] At the same time, the possibility that both poles of the drop become rigidly fixed was not ruled out in Ref. 1. As assumed in Ref. 1, this will make the reorientation of a drop with nucleation of a linear disclination at each pole a threshold process. Rigid fixing of both poles has been observed experimentally[4] in an ensemble of bipolar drops of the nematic liquid crystal 5CB which were dispersed in polyvinylbutyral. In the present letter a theoretical calculation of the orientational structure of such drops as a function of the electric field strength is performed. The computational results are analyzed in comparison with the experimentally measured characteristics of light scattered by a film of polymer-encapsulated liquid crystals (PELCs).

The configuration of the director in a nematic drop in an electric field was calculated by the standard procedure[3] of minimizing the free energy in the one-constant approximation:

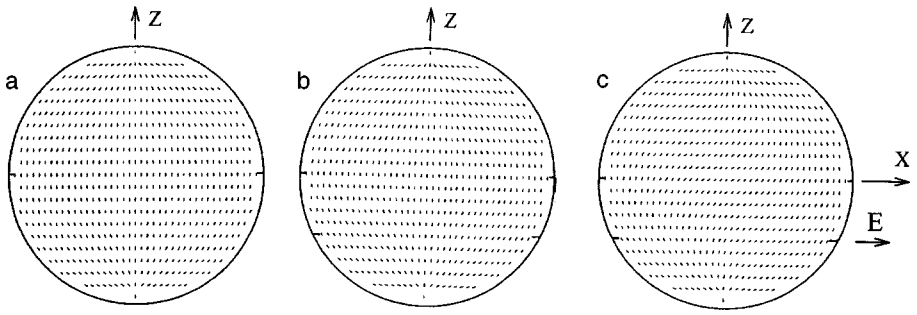

FIG. 1. Orientational structure of a bipolar drop of a nematic in the XZ plane with a) $E_n=0$, b) $E_n=3.2$, and c) $E_n=3.7$.

$$F=\frac{1}{2}\int\{K[(\nabla\cdot\mathbf{n})^2+(\nabla\times\mathbf{n})^2]-\epsilon_0\Delta\epsilon(\mathbf{n}\cdot\mathbf{E})^2\}dV, \tag{1}$$

where $\mathbf{n}$ is the director of the LC, K is the elastic modulus, $\Delta\epsilon=\epsilon_\parallel-\epsilon_\perp$, $\epsilon_\parallel$ and $\epsilon_\perp$ are the components of the dielectric constant, and $\mathbf{E}$ is the electric field vector. We assume the LC molecules to be rigidly anchored on the surface of the polymer matrix and the electric field inside the drop to be uniform. The director orientation at the interface is planar. Unline the case of Ref. 3, a homeotropic orientation of the director is imposed at two diametrically opposite points on the surface of the drop (on the Z axis, Fig. 1), and the vector $\mathbf{E}$ is assumed to be oriented in the direction of the X axis.

Figure 1 shows the computational results for the orientational structure of a spherical drop of a nematic in the section ZX for three values of the normalized electric field:

$$E_n=E/E_0;\quad E_0=\frac{1}{R}\sqrt{\frac{K}{\epsilon_0\Delta\epsilon}}. \tag{2}$$

Here R is the radius of the drop. For $E=0$ (Fig. 1a), just as in Ref. 3, a bipolar director configuration with the symmetry axis directed along the Z axis is realized. Point defects (boojums[5]) occur at points of homeotropic orientation of the director.

When a field is applied, the director configuration starts to change. First, the orientation is observed to change only in the regions where the vectors $\mathbf{E}$ and $\mathbf{n}$ are not orthogonal, and the ordering symmetry of the director in the XZ plane remains the same as before, but the angle of inclination of $\mathbf{n}$ with respect to the Z axis increases (Fig. 1b). The director of the LC at points located on the Z axis and in the XY plane remains stationary. This process is elucidated in Fig. 2 for the central point of the drop and for a point shifted rightward and upward from the center by $R/2$ along the Z and X coordinate axes.

The situation changes substantially for $E_n>3.3$ (Figs. 1c and 2). At the center of the drop and at other points on the Z axis and in the XY plane the director starts to turn. The lines of the director assume a characteristic S shape. Rotation is equally likely to start in one or the other direction, and the resulting patterns will be mirror symmetric with

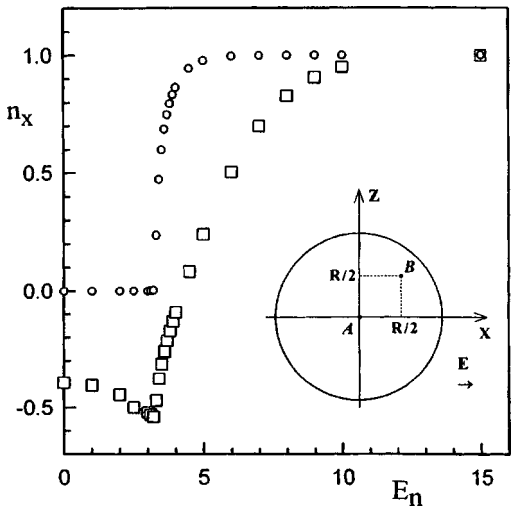

FIG. 2. Projection of the director of the LC on the X axis versus the electric field strength for the points A (○) and B (□) whose location inside the drop is shown in the inset.

respect to the XY plane. Further increasing the field will produce increasingly more uniform orientation of the director in the direction of the field in the volume of the drop. The field

$$E_c = 3.3\,\frac{1}{R}\sqrt{\frac{K}{\epsilon_0 \Delta\epsilon}} \tag{3}$$

is the critical value for the entire volume of the drop. For points where the vectors **E** and **n** are initially orthogonal to one another this has the meaning of a threshold field; elsewhere in the drop it appears as a sharp kink in the curve of the director orientation versus the field strength (Fig. 2).

The experimentally investigated PELC samples prepared as in Ref. 4 consisted of a 15 μm thick polyvinylbutyral film in which drops of the nematic liquid crystal 5CB were dispersed. The round LC drops had a maximum diameter of 19 μm in the film plane and were located in the same layer, making it possible to perform visual observations of the reorientation process using a polarization microscope. In the absence of a field the drops manifested in crossed polarizers a texture that is characteristic for a bipolar director configuration,[5] poles being arranged so that in all drops the axes joining the poles lay in the film plane. The sample was placed between two glass substrates with transparent electrodes on the interior sides. Thus the electric field in the experiment was perpendicular to the initial symmetry axis of the drops. The intensity of the light scattered by the PELC film at an angle α with respect to the direction of the helium–neon laser beam, incident normally, was recorded as a function of the applied voltage using a $X-Y$ plotter.

According to a theoretical geometrical-optics analysis[6] of the characteristics of light scattering by an ensemble of LC drops with size greater than the wavelength of the light, the ray passing along the X axis through the center of the drop makes the main contribution to the intensity of the radiation passing straight through the drop. Therefore in our

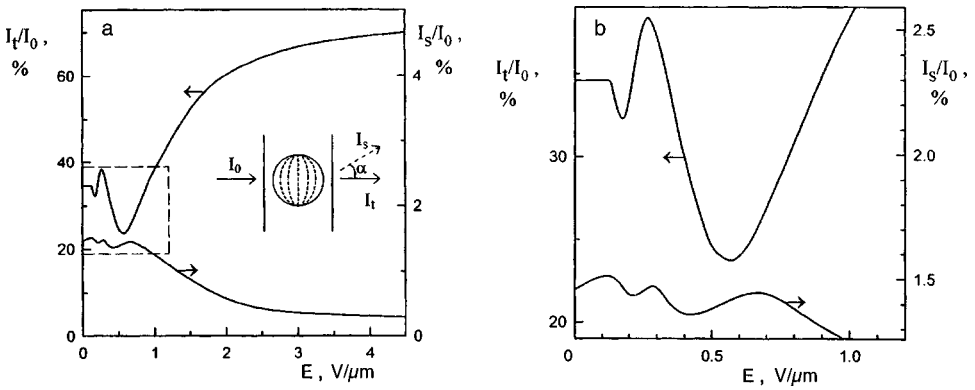

FIG. 3. a) Intensity I_t of the directly transmitted radiation and intensity I_s of the radiation scattered by an angle $\alpha \approx 7°$ versus the applied field. b) Enlargement of the outlined fragment in part a.

case the dependence of the intensity of the radiation passing straight through the drop on the applied field should be of a threshold character. The ray trajectories passing through the side regions of the drop curve as a result of the index gradient at the polymer–LC interface and the continuous variation of the index inside the drop.[6] Therefore the light scattered at an angle $\alpha \neq 0$ carries information about the director orientation in the side regions of the drop and the field dependence of its intensity should be of a nonthreshold form.

The experimental data (Fig. 3) confirm these conclusions. Here the intensity of the transmitted radiation was measured in the range of angles $0 \leqslant \alpha \leqslant 0.5°$ and the intensity of the radiation separated by a ring-shaped diaphragm was measured in the range of scattering angles $6.8 \leqslant \alpha \leqslant 8.5°$. The oscillations on the curves of the directly transmitted radiation above threshold had been observed and discussed earlier in Ref. 4. As one can see, the light-scattering curve has a nonthreshold character and oscillates.

The measured value of the critical field E_c for the experimental sample was equal to 0.13 V/μm. An estimate using Eq. (3) and the parameters $K=(K_{11}+K_{22}+K_{33})/3$, $K_{11}=6.2\times10^{-12}$ N, $K_{22}=3.1\times10^{-12}$ N, $K_{33}=8.3\times10^{-12}$ N (Ref. 7), $\Delta\epsilon=11.8$ (Ref. 8), and $R=9.5$ μm gives the critical field $E_c=0.08$ V/μm. The radius of drops of maximum size was used in the calculations. Since the threshold field for such drops is minimum, they determine the value of E_c for an ensemble of drops of different size. The discrepancy between the computed and experimentally measured values of E_c is mainly due to two factors. First, the real shape of an LC drop in such samples is an ellipsoid, flattened in the film plane, with a ratio of axes equal to about 1.7 (Ref. 9). This makes it necessary to modify the computational model in order to take into account the ellipsoidal nature of the drop. It is obvious that decreasing the size of the drop along at least one of the coordinates will increase the computed value of E_c. The second factor is the redistribution of the applied electric field in the polymer–LC structure. Since the dielectric constant of the LC 5CB is higher than that of the polyvinylbutyral matrix ($\epsilon_\perp/\epsilon_p=1.46$ (Ref. 4)), the critical value of the field inside the drop will be less than the applied field $E_c=0.13$ V/μm.

In summary, the results of this work show that the process leading to the reorienta-

tion of bipolar drops of a nematic is in general a nonthreshold process. This result should also be true for drops with mobile poles. One can talk about a threshold only with respect to separate aspects of the process: onset of motion of the poles of the drop in the case when the poles are not rigidly fixed, or onset of local rotation of a region of a drop where the vectors **E** and **n** are orthogonal to one another in the case when the poles are rigidly fixed. The possibility of a combination of the two types of reorientation of bipolar drops, when the configuration of the director initially changes as shown in Fig. 1 and pole motion starts with a further increase in the field, cannot be ruled out. Apparently, the onset of changes in the configuration of the director (Figs. 1a and 1b) could not be observed by visually[1,2,4] because the deflections of **n** are small and the eye is too insensitive. It should be noted that contrary to the assumption in Ref. 1, the onset of rotation in the central part of the drop (Fig. 1c) is not accompanied by the formation of linear disclinations.

This work was supported by the Ministry of Science of the Russian Federation (under the program ''Physics of Quantum and Wave Processes,'' Grant 2.3) and the Ministry of Education of the Russian Federation (Program ''Fundamental Natural Science'').

[a)]e-mail: mspec@iph.krasnoyarsk.su

---

[1] A. V. Koval'chuk, M. V. Kurik, O. D. Lavrentovich, and V. V. Sergan, Zh. Éksp. Teor. Fiz. **94**, 350 (1988) [Sov. Phys. JETP **67**, 1065 (1988)].
[2] A. V. Koval'chuk, O. D. Lavrentovich, and V. V. Sergan, Pis'ma Zh. Tekh. Fiz. **14,** 197 (1988) [Sov. Tech. Phys. Lett. **14**, 87 (1988)].
[3] S. Zumer and J. W. Doane, Phys. Rev. A **34**, 3373 (1986).
[4] V. Ya. Zyryanov, V. V. Presnyakov, and V. F. Shabanov, Pis'ma Zh. Tekh. Fiz. **22**(14), 22 (1996) [Tech. Phys. Lett. **22**(7), 563 (1996)].
[5] G. E. Volovik and O. D. Lavrentovich, Zh. Éksp. Teor. Fiz. **85,** 1997 (1983) [Sov. Phys. JETP **58**, 1159 (1983)].
[6] R. D. Sherman, Phys. Rev. A **40**, 1591 (1989).
[7] J. D. Bunning, T. E. Faber, and P. L. Sherrell, J. Phys. (Paris) **42**, 1175 (1981).
[8] S. Chandrasekhar, *Liquid Crystals*, Cambridge University Press, New York, 1977 [Russian transl., Mir, Moscow, 1980].
[9] P. S. Drzaic and A. Muller, Liq. Cryst. **5**, 1467 (1989).

Translated by M. E. Alferieff

Polymorphism of biperiodic stripe domain structures

G. V. Arzamastseva, F. V. Lisovskiĭ,[a)] and E. G. Mansvetova
Institute of Radio Engineering and Electronics, Russian Academy of Sciences, 141120 Fryazino, Moscow Region, Russia

(Submitted 9 April 1998)
Pis'ma Zh. Éksp. Teor. Fiz. **67**, No. 9, 701–706 (10 May 1998)

Magnetic-field-induced polymorphism of biperiodic stripe domain structures of films with a positive anisotropy constant and easy axis parallel to the normal to the surface is studied. A symmetry classification of the observed types of domain structures is performed, and the phase diagram of the films in the ($H_\perp$, $H_\parallel$) plane, where $H_\perp$ and $H_\parallel$ are, respectively, the components of the magnetic field vector perpendicular and parallel to the normal to the surface, is determined. © *1998 American Institute of Physics.* [S0021-3640(98)01809-X]

PACS numbers: 75.70.Kw

It is well known that uniaxial films of magnets with a positive anisotropy constant β_u and easy axis along the normal **n** to the surface (henceforth the z axis) and having thicknesses in a definite range $L_{cr}^{*}<L<L_{cr}^{(1)}$, where L_{cr}^{*} and $L_{cr}^{(1)}$ are certain critical values, exhibit quasiharmonic subsurface distortions of the domain wall (DW) profiles in the initial equilibrium stripe domain structure (DS), as a result of which the distribution of the magnetization vector **M** becomes biperiodic (see, for example, Refs. 1–6). Until very recently such structures had scarcely been studied.

We studied DSs in uniaxial films of magnetic garnets with the composition $Lu_{2.1}Bi_{0.9}Fe_{5-x}Mg_xO_{12}$ ($x=0-0.17$) and thickness $L=1-40$ μm, grown by liquid-phase epitaxy (using as Bi_2O_3 or $PbO-Bi_2O_3$ as solvents) on $Gd_3Ga_5O_{12}$ substrates with the (111) orientation. The growth regime was similar to that used in Refs. 7 and 8. The Néel temperature T_N of the films was equal to 560 K and the saturation magnetization $4\pi M$ was equal to 1800 G. Field intensities $H_\parallel^{*}=1500-1750$ Oe and $H_\perp^{*}=25-500$ Oe, respectively, were required in order to magnetize the samples to saturation at $T=293$ K with fields parallel ($H_\parallel=H_z$) and perpendicular ($H_\perp=H_y$) to the normal **n** to the surface. The required fields were produced by an electromagnet with two pairs of orthogonally arranged coils. The values of the uniaxial anisotropy constants for the experimental films at room temperature were in the range 0.72–0.98. For $H_\perp=0$ a simple (monoperiodic) stripe DS with flat (unmodulated) DWs was present in films less than 5 μm thick, while in thicker films a biperiodic stripe DS with in-phase harmonic subsurface modulation of the distribution of the vector **M** in all DWs was present.

The experiments were performed at $T=293$ K with $H_\perp=$ var and $H_\parallel=$ const. A saturating value of the field intensity $H_\perp>H_\perp^{*}$ was established for a chosen value of $H_\parallel$, after which the current in the corresponding pair of coils of the electromagnet was

decreased continuously to zero, the polarity of the current was changed, and the film was once again switched into a state of magnetic saturation by a field $H_\perp$ oriented opposite to the initial direction. Then all observations were repeated for the ascending branch of the hysteresis loop. In the entire existence region of simple and biperiodic DSs, the latter were well ordered but contained defects of the free and bound magnetic dislocation types, i.e., the state of the magnet corresponded to a liquid-crystal phase or a Berezinskiĭ–Kosterlitz–Thouless phase.[9]

In the case of a phase transition (PT) induced by a magnetic field $H_\perp$ from a uniformly magnetized state into a state with a simple stripe DS with period d the walls between the domains became oriented parallel to the vector $\mathbf{H}_\perp$, i.e., they were characterized by a reciprocal lattice vector $\mathbf{b}_1=(2\pi/d)\mathbf{e}_x$. To describe biperiodic DSs it is necessary to know, besides d, two other parameters: Λ_1 and Λ_2 (in the general case $\Lambda_1\neq\Lambda_2$), equal to, respectively, the periods of the surface modulation of the DW profile at the film–free-space and film–substrate interfaces. Then the reciprocal lattice space becomes two-dimensional with $\mathbf{b}_{2i}=(2\pi/\Lambda_i)\mathbf{e}_y$, where $i=1, 2$.

The magnetization distribution in a DS of any type was nonuniform over both the thickness and the extended faces of the films. Observations of the behavior of the DSs showed that the existence region of biperiodic structures in the ($H_\perp$, $H_\parallel$) phase diagram always lies inside the region of stability of simple stripe DSs.[b)] Depending on the past history and the values of the components of the field intensity ($H_\perp$, $H_\parallel$), several types of biperiodic DSs classifiable by symmetry materialize.

The typical form of a phase diagram for one of the experimental films (No.1), 16 μm thick, is displayed in Fig. 1. The curves of the first- and second-order PTs are drawn using solid and dashed lines, respectively; the boundaries of instability are drawn by the dot–dash line; Roman numerals denote different stable states of the film (I — uniformly magnetized states, II — simple stripe DSs, III–VI — biperiodic stripe DSs). The results of a symmetry classification are also indicated in Fig. 1 for the states III–VI: motif-forming elements (in the form of black-and-white figures, outlined by a thick solid line), domain walls (dashed lines), and rectangular Bravais cells (thin solid lines). Auxiliary dashed lines are used to accent the individual symmetry operations. The black–white distribution of the motif-forming elements symbolically represent the nonuniform distribution of the vector $\mathbf{M}$ on any of the two film surfaces (or in any plane parallel to the film): Regions where the projections M_z all have the same sign (for any value of M_z) are indicated in black, and regions where M_z has the opposite sign are indicated in white, while the dashed lines (DWs) correspond to the set of points where $M_z=0$. Within the framework of the symbols adopted the symmetry of the biperiodic DSs which are realized is described by one of six two-dimensional space groups of the rectangular system with a primitive (*Pam*2, *Pa*, *Pmm*2, *Pm*) or centered (*Cmm*2, *Cm*) Bravais cell. The structures with *Pa*, *Pm*, and *Cm* symmetry can exist in dual modifications corresponding to two antiparallel directions of the vector $\mathbf{H}_\perp$.

The simplest situation is a symmetric in-phase biperiodic DS (Fig. 2a) with the *Pam*2 symmetry, arising for $H_\perp=0$, i.e., in region VI in Fig. 1. Any field $H_\perp$, however weak, transfers such a structure by a second-order PT into one of two modifications of an asymmetric in-phase biperiodic DS (Fig. 2b) with *Pa* symmetry, which coexist in the regions V in Fig. 1. A further increase of $H_\perp$ causes (for $H_\parallel<H_\parallel^{(cr)}\simeq 70$ Oe) these structures to transform into a asymmetric[c)] antiphase biperiodic DSs (Fig. 2c) with *Pm*

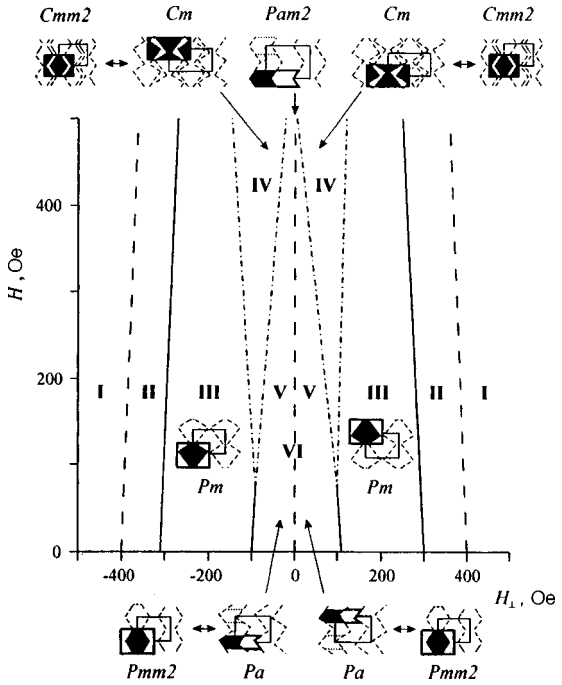

FIG. 1. Phase diagram of film No. 1, 16 μm thick, in the ($H_\perp$, $H_\parallel$) plane.

symmetry, which exist in the regions III in Fig. 1. As $H_\perp$ increases, such structures transform (first-order PT) into simple stripe structures (regions II in Fig. 1).

For $H_\parallel > H_\parallel^{(cr)}$ new links appear in the chain of PTs: transformation of antiphase biperiodic DSs into in-phase biperiodic structures as $H_\perp$ varies occurs via ''buffer'' DSs (Fig. 2d) with *Cm* symmetry, which exist in regions IV in Fig. 1. These structures, which form a sequence of alternating sections of in-phase and antiphase biperiodic DSs and possess a period $d' = 2d$ twice that of the neighboring phases, can be called double mirror-symmetric biperiodic DSs. If their existence region in the diagram in Fig. 1 intersects the ordinate, then for $H_\perp = 0$ they transform into double bisymmetric biperiodic DSs with *Cmm*2 symmetry.

The evolution of the experimentally observed DSs for film No. 1 with $H_\parallel = 0$ and $H_\perp = \text{var}$ is illustrated in Fig. 3. Starting from the region with a simple stripe DS and decreasing the field intensity $H_\perp$, an antiphase biperiodic DS (with the maximum possible modulation period of the DW profile $\Lambda_1 = \Lambda_{1\max}$ for the given surface), which, judging from the form of the observed diffraction patterns is close to being symmetric, forms abruptly on the film–free-space interface at a definite critical value of $H_\perp$. In a somewhat weaker field a similar DW bending instability also arises on the film–substrate interface (with the minimum possible period $\Lambda_2 = \Lambda_{2\min} < \Lambda_{1\max}$ for the given surface). In some range of values of $H_\perp$ both surface structures exist independently and do not influence one another; the modulation periods Λ_1 and Λ_2 of the DW profiles in both structures remain virtually constant. Then, as a result of an increase in the penetration depth of the modulation of the DW profiles, there arises between the surface biperiodic

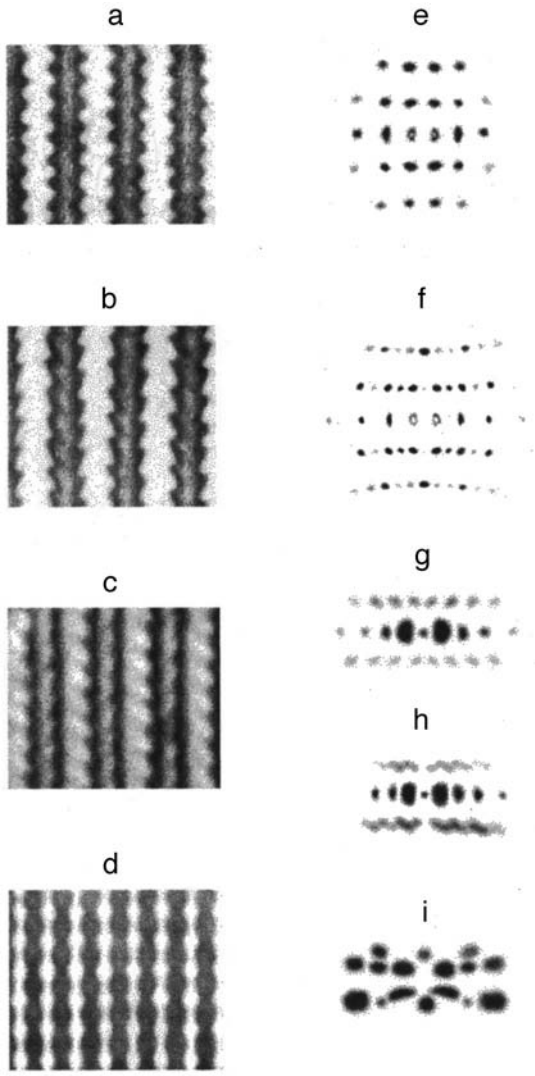

FIG. 2. Photographs of some of the observed DSs (a–d) and the corresponding diffraction patterns (e–i) for film No. 1.

structures a coupling that causes the antiphase symmetric biperiodic DS to transform into one of the dual modifications of the in-phase asymmetric biperiodic DS. Moreover, a pronounced field dependence of the modulation periods Λ_1 and Λ_2 appears; their values change abruptly and converge toward one another. Next, complete spatial synchronization[d)] of quasiharmonic distortions of the profile on both film surfaces ($\Lambda_1 = \Lambda_2 = \Lambda$, where $\Lambda_{1\min} < \Lambda < \Lambda_{2\max}$) obtains and a single in-phase asymmetric biperiodic DS forms and remains stable for $H_\perp = 0$ also.

After the sign of the field changed and its intensity increased by a small amount (<5 Oe), abrupt magnetization reversal (change in the sign of the projection M_z in all

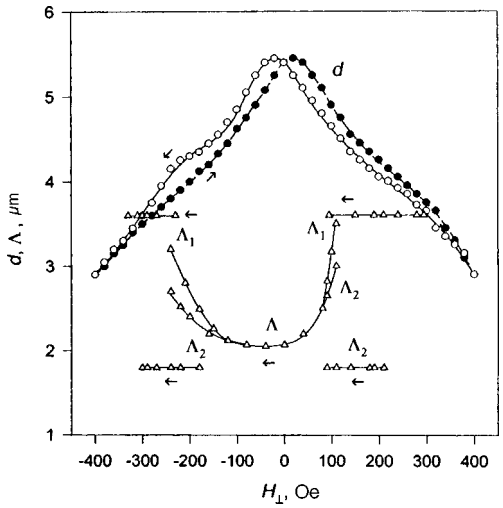

FIG. 3. Geometric parameters of biperiodic stripe DSs in film No. 1 versus the magnetic field $H_\perp$.

domains to the initial direction of the vector $\mathbf{H}_\perp$), accompanied by a transition of the initial in-phase asymmetric biperiodic DS into the dual modification, occurred in the film.[e)] As the intensity $H_\perp$ of the field with the opposite (with respect to the initial) direction increased, all processes proceeded similarly in the opposite sequence with hysteresis characteristic for a first-order phase transition. Nucleation processes materialized via magnetic dislocations, which introduced into the initial domain array not only different values of the periods d and Λ but also a different local symmetry. Second-order phase transitions occurred only for transitions between symmetric and asymmetric modifications of in-phase (symmetry groups *Pam*2 and *Pa*) and antiphase (symmetry groups *Pmm*2 and *Pm*) biperiodic DSs, but with cyclic variation of the field $H_\perp$ they also occurred in noncoincident intervals for different directions of variation of the field because the field dependence of the period d of the ''parent'' stripe DS also exhibits hysteresis (see Fig. 3).

The existence of different types of biperiodic DSs is confirmed by experiments on the diffraction of light by two-dimensional domain arrays. When light incident on the film along the z axis is scattered, diffraction maxima arise in the directions $\mathbf{k}_{(p,q)}=\mathbf{k}+p\mathbf{b}_1+q\mathbf{b}_2$, where $\mathbf{k}$ is the wave vector of the primary light beam, p and q are integers, and $\mathbf{b}_1$ and $\mathbf{b}_2$ are basis vectors of the reciprocal lattice. A symmetry analysis shows that for $\overline{d}_+=\overline{d}_-=d/2$, where $\overline{d}_+$ and $\overline{d}_-$ are the average widths of domains with $M_z>0$ and $M_z<0$, respectively, quenching of maxima with $p=2n$ and arbitrary q (except for the main diffraction maximum) will be observed for the in-phase symmetric biperiodic DSs, while for antiphase symmetric biperiodic DSs quenching of maxima with $p=2n+1$ and arbitrary q (except for maxima with $(p,q)=(\pm 1,0)$) will be observed. When light is scattered by biperiodic structures with a doubled period the directions to the diffraction maxima are determined by the relations $\mathbf{k}_{(p,q)}=\mathbf{k}+p\mathbf{b}_1'+q\mathbf{b}_2$, where $\mathbf{b}_1'\simeq\mathbf{b}_1/2$ and $\mathbf{b}_1$ is a corresponding reciprocal-lattice vector for the parent in-phase or antiphase structure that has given rise to the particular double biperiodic DS. For bisymmetric double bipe-

riodic DSs quenching of all diffraction maxima with $p=2n$ and arbitrary $q \neq 0$, where $|n| \geqslant 1$, is observed; this does not happen for mirror-symmetric double biperiodic structures.

Photographic negatives of the experimentally observed diffraction patterns for film No. 1 are presented in Figs. 2e–i. Photographs e and f correspond to symmetric and asymmetric in-phase biperiodic DSs, photograph g corresponds to a double mirror-symmetric system, photograph h corresponds to coexistence of in-phase asymmetric and dual mirror-symmetric systems, and photograph i corresponds to the coexistence of in-phase asymmetric and antiphase symmetric biperiodic DSs (in the latter case, to eliminate stray illumination, the central diffraction maximum and the lower part of the diffraction pattern were shielded). The form of the actually observed diffraction patterns agrees well with a qualitative symmetry analysis.

This work was supported by the Russian Fund for Fundamental Research under Project 96-02-16082-a.

[a)]e-mail: lisf@dataforce.net

[b)]If the film thickness $L \rightarrow L_{cr}^{*}+0 \simeq 5$ μm, then the existence region of domains with modulated DW profiles contracts to a point, while the amplitude of the harmonic distortions of a DW profile goes to zero monotonically.

[c)]Symmetric modifications of antiphase DSs can exist only for $H_{\perp}=0$. Such a situation can materialize in quite thin films with a wide hysteresis loop for a first-order phase transition between states with *Pm* and *Pa* symmetry.

[d)]In sufficiently thick films ($L > \simeq 20$ μm) a single ''synchronized'' biperiodic DS does not form at all: In the entire existence region two unrelated systems of DWs with modulated profiles and different modulation periods Λ_1 and Λ_2 but the same period d of the stripe domains are observed.

[e)]When the intensity $H_{\perp}$ of the field decreased back to zero, the asymmetric in-phase biperiodic DS transformed into a symmetric structure.

[1]W. S. Paxton and T. G. Nilan, J. Appl. Phys. **26**, 65 (1955).
[2]H. Williams and R. Sherwood, in *Magnetic Properties of Metals and Alloys* [Russian translation], IL, Moscow, 1961, p. 61.
[3]J. Kaczer and R. Gemperle, Czech. J. Phys., Sect. B **11**, 157 (1961).
[4]G. S. Kandaurova, Izv. Vyssh. Uchebn. Zaved. Fiz. **5**, 12 (1964).
[5]L. S. Palatnik, L. I. Lukashenko, Yu. V. Zolotnitskiĭ *et al.*, Zh. Éksp. Teor. Fiz. **59**, 1177 (1970) [Sov. Phys. JETP **32**, 643 (1971)].
[6]S. Tikazumi, *The Physics of Ferromagnetism: Magnetic Characteristics and Applications* [Russian translation], Mir, Moscow, 1987.
[7]H. Tamada and M. Kaneko, T. Okamoto, J. Appl. Phys. **64**, 554 (1988).
[8]H. Huahui, S. Jan, D. Hanming *et al.*, IEEE Trans. Magn. **MAG-25**, 3497 (1989).
[9]I. E. Dikshteĭn, F. V. Lisovskiĭ, E. G. Mansvetov *et al.*, Zh. Éksp. Teor. Fiz. **86**, 1473 (1984) [Sov. Phys. JETP **59**, 863 (1984)].

Translated by M. E. Alferieff

Excitons and excitonic complexes in GaAs/AlGaAs quantum wells with a low-density quasi-two-dimensional electron and hole channel

O. V. Volkov,[a)] V. E. Zhitomirskiĭ, and I. V. Kukushkin
Institute of Solid-State Physics, Russian Academy of Sciences, 142432 Chernogolovka, Russia

K. von Klitzing and K. Eberl
Max-Planck-Institut für Festkörperforschung, 70569 Stuttgart, Germany

(Submitted 9 April 1998)
Pis'ma Zh. Éksp. Teor. Fiz. **67**, No. 9, 707–713 (10 May 1998)

The recombination spectra of excitons and excitonic complexes in undoped GaAs/AlGaAs single quantum wells are investigated. It is shown on the basis of a study of the magnetic-field dependence of the emission spectra and the degree of optical orientation in zero magnetic field and on the basis of electrooptic measurements that not only the density but also the sign of the charge carriers in a well depend strongly on the photoexcitation energy. It is shown on the basis of a comparative analysis of the spin splitting of the recombination lines of free and bound excitons that the recombination line which was attributed earlier to a positively charged exciton corresponds to the recombination of an exciton bound on a neutral acceptor. © *1998 American Institute of Physics.* [S0021-3640(98)01909-4]

PACS numbers: 73.20.Dx, 71.35.Cc

1. Interest in low-dimensional electron–hole systems with low carrier density — with an average distance between the particles much greater than the Bohr radius of an exciton — has increased substantially recent years. In such systems the formation of excitonic complexes (trions) X^- and X^+which are analogs of the hydrogen ions H^- and H_2^+ can occur. The study of these complexes is extremely interesting both for understanding the role of the Coulomb interaction in a system of several particles and for modeling the properties of matter in ultrahigh magnetic fields, in which the magnetic quantization energy is much higher than the binding energy of the particles. The latter case is easily obtained in semiconductors on account of the fact that the effective mass of the electrons and holes is much smaller than the mass of a free electron and proton.

In quantum wells the restriction on carrier motion in a direction perpendicular to the plane of the well results in a higher binding energy of electron–hole complexes, and the formation of X^- and X^+ becomes energetically favorable in photoexcited systems with a small excess of electrons or holes.[1] Nonetheless, a number of unanswered questions remain, both theoretical and experimental. For example, as was shown in Ref. 2, the excitonic complexes X^- are strongly localized and apparently consist of excitons bound

on a neutral impurity in a barrier next to a well (D^0X). The questions of the nature of these impurities and of what happens in the system as carrier density increases and the recombination line of the excitonic complexes transforms into an emission line of a quasi-two-dimensional (2D) gas, remain open. The second question is difficult to investigate theoretically because of the large number of interacting particles, so that even the simulation of an isolated free trion is very approximate, and the complicated structure of the valence band is not taken into account at all.[3]

In the most interesting, low-density range ($\sim 10^{10}$ cm^{-2}) the particle localization makes it practically impossible both to determine the carrier density by transport methods and to control it by means of gates. However, a number of experiments[4,2] indicate that because of the comparatively high density of residual impurities (*n* or *p* type) in AlGaAs even undoped quantum wells contain a low-density 2D electron or hole gas. Here the important parameter determining the carrier type and density is the photoexcitation energy. The present work is devoted to a detailed investigation of this phenomenon by optical methods. Excitation by photons with different energy made it possible to switch from a negatively to a positively charged 2D system through zero carrier density. A comparative analysis of the magnetic field dependences of the splittings of the recombination lines of a free exciton and electron and hole excitonic complexes was performed, and it demonstrates the difference in the degree of their localization. It is shown that just as in the case of X^- (Ref. 2) the line previously attributed to X^+ corresponds to recombination of a localized complex, specifically, an exciton bound on a neutral acceptor located in a barrier next to a well.

2. We investigated undoped 200 Å and 300 Å wide GaAs single quantum wells (SQWs) with $Al_{0.3}Ga_{0.7}As$ barriers grown by molecular-beam epitaxy (MBE) on a undoped GaAs substrate. The characteristic carrier mobility in the lightly-doped test structures was equal to 2.6×10^6 cm^2/V·s with density 5×10^{10} cm^{-2} (Ref. 2). The high quality of the experimental structures is also confirmed by the small width (0.1 meV) of the luminescence lines in a $\sim$10 T magnetic field. Optical excitation of the system was performed with a tunable Ti/Sp laser with photon energy 1.77–1.46 eV and/or He/Ne laser with photon energy 1.959 eV. The spectral instrument consisted of a Ramanor U-1000 double monochromator, which, combined with a charge-coupled (CCD) semiconductor detector, gave a resolution of 0.03 meV. The measurements were performed at temperature 1.5–2.5 K in magnetic fields in the range 0–11 T.

3. Figure 1a shows the photoluminescence spectra measured for a 300 Å SQW in zero magnetic field under excitation by two lasers with different power ratios. The spectra *A* and *E* were obtained by excitation with Ti/Sp and He/Ne lasers, respectively, with a power density of 50 mW/cm^2. The spectra *B*, *C*, and *D* were obtained with excitation by a Ti/Sp laser of the same power as *A* combined with illumination with a He/Ne laser with power equal to 1×10^{-3}, 2×10^{-3}, and 4×10^{-3} times the power of the Ti/Sp laser. As is well known, the ratio of the intensities of free and bound excitons can serve as a measure of the carrier density for a dielectric system.[1,2] As the carrier density increases, this ratio drops to zero and at the same time a transition to a metallic state occurs. The spectrum *A*, where the recombination line of a free exciton is practically absent, corresponds to electron density close to the metal–insulator transition point (compare Fig. 1 in Ref. 2, where spectra measured in a doped structure with a similar architecture were measured). In the case at hand electrons accumulate in the well on account of residual

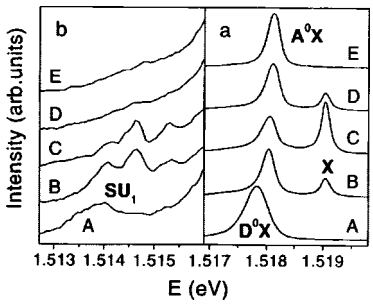

FIG. 1. a) Photoluminescence spectra measured in a 300 Å SQW in zero magnetic field with combined excitation by Ti/Sp in He/Ne lasers with different power ratios. b) Cyclotron replica in photoluminescence spectra measured in a 2 T magnetic field under the same conditions as in (a).

impurities present in AlGaAs with a density of the order of 1×10^{15} cm^{-3} (Ref. 4). Illumination at photon energies above the band gap in AlGaAs decreases the carrier density in the well on account of the fact that the electrons and holes created in the barrier are separated by an electric field and dynamically neutralize the charge of ionized impurities in the barrier and carriers in the well (irrespective of their sign).[4,2] This explains the increase in the intensity of the *X* recombination line of a free exciton in the spectra *B* and *C*. However, as the power of illumination by the He/Ne laser increases further (*D*), the intensity goes back down to the point that the *X* line vanishes completely from the spectrum (*E*). This behavior can be explained only by a restorative increase in the carrier density in the well.

It is well known[5] that the complex $X^-(D^0X)$ in a magnetic field characteristically exhibits cyclotron replicas — additional spectral lines with a linear negative diamagnetic shift equal to one or several electron cyclotron energy quanta. They are related with the recombination of the complex with the remaining electron being transferred into higher-lying Landau levels. Cyclotron replicas were indeed observed in the cases *A*–*C* (Fig. 1a). The corresponding section of the spectrum in a 2 T magnetic field is shown in Fig. 1b. However, in the cases *D* and *E* electron-type cyclotron replicas are completely absent. This indicates that the increase in carrier density in this case is due to the appearance of a 2D hole gas in the well. The cyclotron replicas here have a much smaller splitting and are not resolved in the recombination spectra. Therefore, with increasing power of illumination with photon energies above the band gap in AlGaAs, a transition occurs from a 2D electronic system to a hole system through zero density. Interestingly, a cyclotron replica transforms substantially in the region close to zero electron density. Splitting into three narrow lines is seen in the spectra *B* and *C*. These lines are most likely due to transitions between impurity-center states with different symmetry.[6] As electron density increases (*A*), the Coulomb potential of the impurity center becomes screened and these lines transform into a single wide line.

We obtained similar results for a 200 Å wide SQW. In this case, however, the structure was found to be initially *p* type, and excitation by a He/Ne laser resulted in inversion of the carrier type and the appearance of a 2D electronic channel. Figure 2a shows spectra measured in a 2.5 T magnetic field with excitation above and below the band gap in AlGaAs. A cyclotron replica associated with recombination of a D^0X com-

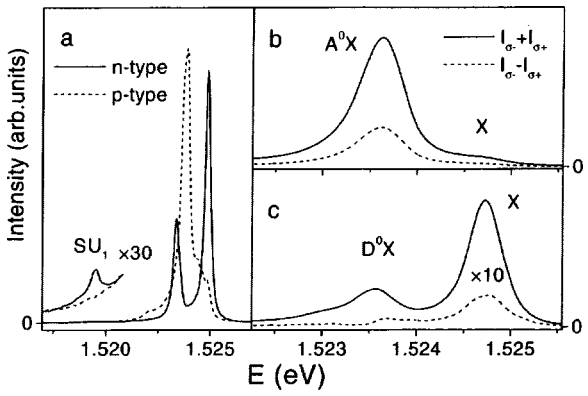

FIG. 2. a) Photoluminescence spectra measured for a 200 Å SQW in a 2.5 T magnetic field with 1.959 eV (solid line) and 1.653 eV (dashed line) photoexcitation. b,c) Sum and difference of the spectra measured in two circular polarizations in zero magnetic field with excitation by circularly polarized 1.599 eV light (b) and in combination with 1.959 eV illumination (c).

plex is clearly seen in the spectra in the first case, while it is absent in the second case. To determine the nature of the bound excitonic state in this case we employed the method of optical orientation, similar to that used in Ref. 7 to study X^- and X^+ complexes in doped structures. Figure 2b (solid line) shows the photoluminescence spectrum measured in zero magnetic field with excitation by circularly polarized light with photon energy only slightly greater than the band gap in GaAs. The orientation of the electron spin is partially preserved in the process of energy relaxation of the electrons. On account of the strong spin–orbit interaction, which is characteristic of holes, hole scattering during the relaxation process results in complete spin disorientation. For this reason, the recombination line of a D^0X complex possessing two electrons with opposite spins is found to be unpolarized, while the recombination line of a A^0X complex possessing one electron should be strongly polarized. Figure 2b (dashed line) shows the difference of the intensities measured in two circular polarizations. The appreciable degree (35%) of polarization of the low-energy line indicates that it is indeed due to the recombination of a A^0X complex in a 2D hole system. However, even weak illumination by a He/Ne laser with power equal to 3×10^{-4} times that of the main pump (Fig. 2c) decreases the degree of polarization of the low-energy line by two orders of magnitude and in a magnetic field leads simultaneously to the appearance of a cyclotron replica that is characteristic of a D^0X complex. This proves that in this case a transition occurs from a 2D hole to an electronic system. The difference in the sign of the initial carrier density as compared with a 300 Å SQW is apparently due to the difference in the type of carriers introduced uncontrollably into AlGaAs in the different MBE apparatus where these structures were grown. It should be noted that the carrier-type inversion is not uniquely related with the excitation energy. For example, excitation by an Ar^+ laser did not produce inversion in the experimental structures, while a series of narrow resonances, whose excitation does lead to inversion, was observed at energies below the band gap in AlGaAs. The mechanism of this phenomenon has yet to be explained.

Figure 3 shows the energy of the recombination lines of free and bound excitonic

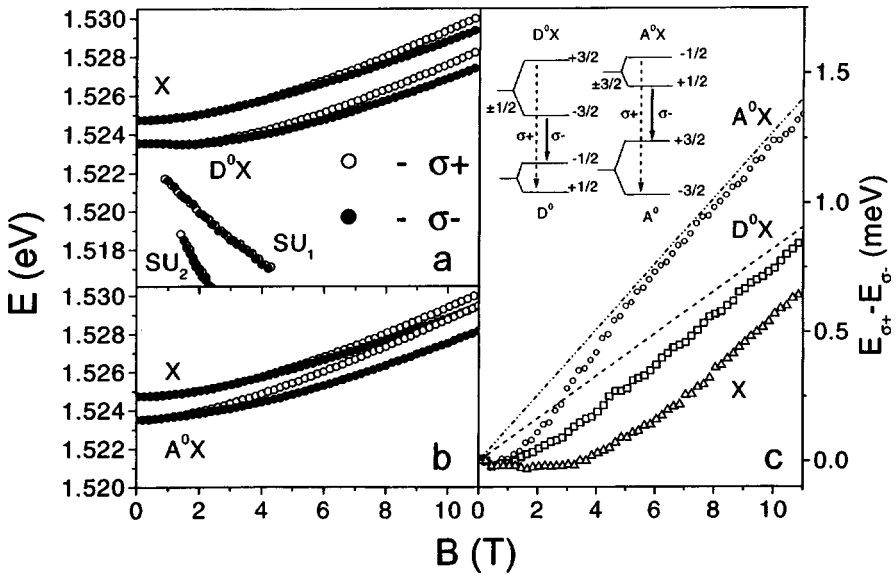

FIG. 3. a,b) Spectral position of the recombination lines of free and bound excitons and cyclotron replicas versus magnetic field, measured in two polarizations for a 200 Å SQW with 1.959 eV (a) and 1.653 eV (b) photoexcitation. c) Energy splitting between the σ^+ and σ^- components of the recombination lines versus the magnetic field, measured for a free exciton (△) and for excitonic complexes bound on a donor (□) and acceptor (○). The dashed and dot-dash lines show the field dependence of the splitting measured for a neutral donor and acceptor in GaAs.

states, measured in two circular polarizations, versus the magnetic field for a 200 Å SQW under excitation above (a) and below (b) the band gap in AlGaAs. In the first case the cyclotron replicas $SU_{1,2}$ associated with recombination of a D^0X complex are also shown. It should be noted that the spin splitting of the recombination line of a A^0X complex (difference of the transition energies in two polarizations) is much greater than the splitting of the recombination line of the D^0X complex. Figure 3c shows the magnetic field dependence of the spin splitting for the recombination lines of a free exciton X as well as the complexes D^0X and A^0X. The inset shows the transition scheme corresponding to recombinations $D^0X \rightarrow D^0 + h\nu$ and $A^0X \rightarrow A^0 + h\nu$. It is easy to see that the difference of the transition energies measured in two polarizations should be the same for these two processes and equal to the sum of the electron and hole spin splittings, just as in the case of a free exciton. The experimentally observed difference of the splittings in these three cases, like the nonlinearity in the magnetic field, could be due only to the nonlinear magnetic field dependence of the hole energy levels, as a result of which their spin splitting depends on the kinetic energy of the hole.[8] The spin splitting of the hole energy levels increases with the binding energy of the hole in the plane. This confirms the conjecture that both electronic (X^-) (see Ref. 2) and hole (X^+) trions are localized, and the binding energy of the hole should be maximum in the final state in the case of recombination of the A^0X complex, as is in fact observed experimentally. Moreover, the spin splitting of the recombination lines of D^0X and A^0X complexes in high fields approaches the splitting corresponding to these complexes in a three-dimensional semiconductor (dashed lines in Fig. 3c).[6,9] We note that if the hole trion were free (X^+), the

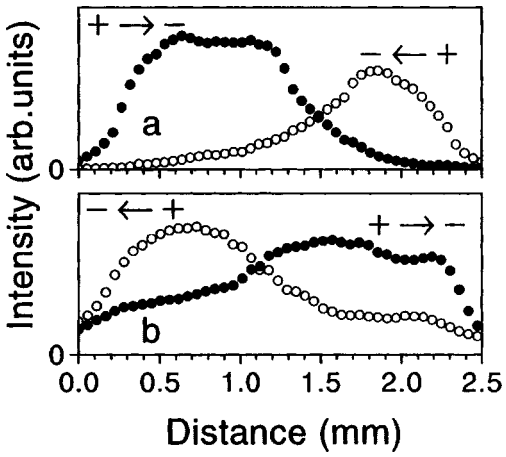

FIG. 4. Distribution of the total intensity of the radiation over the sample in the direction of the external electric field ($E = \pm 300$ V/cm) for a 200 Å SQW with 1.959 eV (a) and 1.653 eV (b) photoexcitation.

final state in the case of its recombination would correspond to a free hole and the spin splitting would be even smaller than for a free exciton, which radically contradicts experiment.

To confirm conclusively that inversion of the carrier type occurs in a quantum well under illumination at photon energies above the band gap in AlGaAs, we performed a simple electrooptic experiment. Two indium contacts in the form of parallel strips separated by 2.5 mm were made on the surface of the sample. It was found that the intensity of the photoluminescence of an uniformly illuminated sample is distributed very nonuniformly when an in-plane electric field is applied to it. The charge carriers, screening the applied electric field, move toward one of the electrodes, and a region with close-to-zero density, where the in-plane applied voltage drop occurs, is produced around the other electrode. The electric field in this region leads to impact ionization of excitons and a corresponding decrease in the luminescence intensity. The sign of the carriers can be determined from the sign of the field applied to the structure. Figure 4 shows the distribution of the total intensity of the exciton luminescence, measured in a ± 300 V/cm electric field with excitation above (a) and below (b) the band gap in AlGaAs. As one can see from the figure, in the first case the carriers have a negative sign (they move toward the positive electrode), while in the second case they are positive.

In summary, we have observed that not only the density but also the sign of carriers in undoped quantum wells can change as a result of excitation of the system by photons with energy above the band gap in AlGaAs. A comparative analysis of the spin splitting of the recombination lines of free and bound excitons was performed, making it possible to identify excitonic complexes as excitons localized on neutral donors and acceptors in the case of a 2D electron and hole system.

This work was supported by the Russian Fund for Fundamental Research and the Volkswagen Foundation.

[a)]e-mail: volkov@issp.ac.ru

[1]A. J. Shields, M. Pepper, D. A. Ritchie, and M. Y. Simmons, Adv. Phys. **44**, 47 (1995).
[2]O. V. Volkov, V. E. Zhitomirskiĭ, I. V. Kukushkin *et al.*, JETP Lett. **66**, 766 (1997).
[3]J. R. Chapman, N. F. Johnson, and V. N. Nicopoulos, Phys. Rev. B **57**, 1762 (1998).
[4]J. L. Osborne, A. J. Shields, M. Pepper *et al.*, Phys. Rev. B **53**, 13002 (1996).
[5]G. Finkelstein, H. Shtrikman, and I. Bar-Joseph, Phys. Rev. B **53**, 12593 (1996).
[6]V. A. Karasyuk, D. G. S. Beckett, M. K. Nissen *et al.*, Phys. Rev. B **49**, 16381 (1994).
[7]G. Finkelstein, H. Shtrikman, and I. Bar-Joseph, Phys. Rev. B **53**, 1709 (1996).
[8]U. Ekenberg and M. Altarelli, Phys. Rev. B **32**, 3712 (1985).
[9]W. O. G. Schmitt, E. Bangert, and G. Landwehr, J. Phys.: Condens. Matter **3**, 6789 (1991).

Translated by M. E. Alferieff

Defect-induced instabilities in condensed media

O. B. Naĭmark[a)]
Institute of Mechanics of Continuous Media, Urals Branch of the Russian Academy of Sciences, 614013 Perm, Russia

(Submitted 21 January 1998; resubmitted 6 April 1998)
Pis'ma Zh. Éksp. Teor. Fiz. **67**, No. 9, 714–721 (10 May 1998)

Some universal responses of condensed media to intense loads are studied. This behavior is attributed to the evolution of ensembles of mesoscopic defects (microcracks, microshears). It is shown that there exist several types of attractors which control the evolution of ensembles of defects under conditions of nonequilibrium transitions. The role of these transitions in the development of anomalies of the deformational behavior of solids and instabilities during fluid flow is discussed. [S0021-3640(98)02009-X]

PACS numbers: 62.50.+p, 61.72.Qq, 83.50.−v, 62.20.Fe

Condensed media exhibit unexpected indications of universal behavior under intense loads in the range of stress amplitudes and load durations where strength and relaxation effects due to structural changes have a considerable influence. Experiments on shock loading of liquids and solids with pressure amplitudes less than 100 GPa have established the existence of general deformational responses of condensed media under conditions such that a governing role is played by the influence of the structure-sensitive properties (strength, plasticity) due to the evolution of mesoscopic defects. The density of these defects reaches 10^{12}–10^{14} cm^{-3}, but each mesoscopic defect consists of a dislocation ensemble and exhibits the properties of this ensemble. Scenarios of the evolution of ensembles of mesoscopic defects show features of nonequilibrium kinetic transitions, and experimental data obtained in a wide range of stress intensities and rates of strain confirm the universality of the structural evolution and its effect on relaxational properties and fracture. This universality can be viewed as a form of self-similarity and shows up strikingly in plastic instability and localization of fracture under dynamic loading. The self-similarity in the behavior of solids under a pulsed load is due to the excitation of spatiotemporal structures in ensembles of defects. In solids subjected to shock-wave loading these structures exhibit pronounced fractographic features and their formation is accompanied by qualitative changes in the response of solids to loading (''dynamical branch'' during spallation,[1] anomalous dependence of the viscosity on the rate of strain,[2] ultradeep penetration[3]). The parameters describing the typical mesoscopic defects (microcracks, microshears) were introduced in Refs. 4 and 5 as a localization of the corresponding group of symmetries of the distortion tensor and can be viewed as fluctuations of the displacement field. These defects are described by symmetric tensors of the form $s_{ik}=s\nu_i\nu_k$ in the case of microcracks and $s_{ik}=1/2s(\nu_i l_k+l_i\nu_k)$ for microshears. Here $\boldsymbol{\nu}$ is unit vector normal to the base of a microcrack (normal break) or slip plane of a

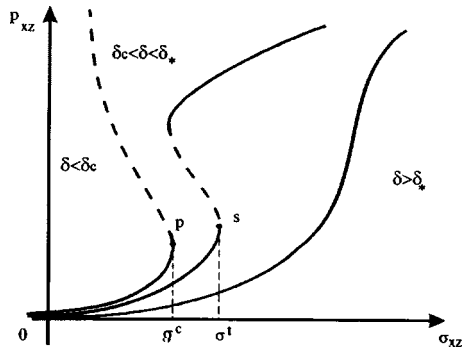

FIG. 1. Characteristic responses of materials to growth of defects.

microscopic shear; **l** is a unit vector in the direction of shear; s is the volume of a microcrack or the shear intensity for a microscopic shear. The microscopic kinetics for the parameter s_{ik} is determined by the Langevin equation

$$\dot{s}_{ik}=K_{ik}(s_{lm})-F_{ik}, \tag{1}$$

where $K_{ik}(s_{lm})$ and F_{ik} are, respectively, the deterministic and random parts of the force field and satisfy the relations $\langle F_{ik}(t)\rangle=0$ and $\langle F_{ik}(t')F_{ik}(t)\rangle=Q\delta(t-t')$. Here Q is the correlation function of the fluctuating forces (nonequilibrium potential determining the energy relief of the initial structure). The size and orientation distribution function $W(s,\boldsymbol{\nu},\mathbf{l})$ of the defects in the phase space of the states is given by the Fokker–Planck equation

$$\frac{\partial}{\partial t}W=-\frac{\partial}{\partial s_{ik}}K_{ik}W+\frac{1}{2}Q\frac{\partial^2}{\partial s_{ik}\partial s_{ik}}W. \tag{2}$$

As was shown in Ref. 4, the Lagrangian of these defects, which consist of dislocation pile-ups, can be written in the form

$$E=E_0-H_{ik}s_{ik}+\alpha s_{ik}^2 \tag{3}$$

and includes a term $H_{ik}s_{ik}$ that reflects the interaction of defects with an external field and between defects. The ''effective field'' H_{ik} is written as a sum of an external stress field and the mean-field produced by the defects: $H_{ik}=\gamma\sigma_{ik}+\lambda p_{ik}$, where σ_{ik} is the macroscopic stress tensor, $p_{ik}=n\langle s_{ik}\rangle$ is the macroscopic microdefect density tensor, n is the microdefect density, and λ and γ are parameters of the material. The quadratic term αs_{ik}^2 in Eq. (3) reflects the energy fluctuation arising in the immediate vicinity of a defect as a result of the development of the defect. The solution of the Fokker–Planck equation based on the assumption of statistical self-similarity of the defect distribution[6] makes it possible to represent the distribution function in the form $W=Z^{-1}\exp(-E/Q)$, where Z is a generalized partition function. The macroscopic magnitude p_{ik} of the ''stationary'' nonequilibrium fluctuations is determined by averaging:[4]

$$p_{ik}=n\int s_{ik}W(s,\boldsymbol{\nu},\mathbf{l})ds\ d^3\boldsymbol{\nu}\ d^3\mathbf{l}. \tag{4}$$

Figure 1 shows p_{xz} versus σ_{xz} for the case of a simple shear for different values of the

parameter $\delta=2\alpha/\lambda n$. The parameter δ is determined by two characteristic scales: the characteristic size l_n of the nucleus of a mesoscopic defect and the average distance l_c between defects. The dislocation model of mesoscopic defects[5] gives $\alpha\approx G/V_0$, where G is the shear modulus and V_0 is the initial ''free'' volume (volume of the nucleus). Estimating the mean-field constant as $\lambda\approx G$ gives $\delta\approx l_c/l_n$. The solution of Eq. (4) shows that transitions to equivalent classes of curves in Fig. 1 occur when the parameter δ reaches critical values δ_* and δ_c, which are bifurcation points. The curves in Fig. 1 correspond to the characteristic responses of a material to a change in the basic modes describing an ensemble of defects, and phenomenologically this behavior can be reflected in the form of the Ginzburg–Landau expansion for the free energy F:[5]

$$F=\frac{1}{2}A\left(1-\frac{\delta}{\delta_*}\right)p_{ik}^2+\frac{1}{4}Bp_{ik}^4-\frac{1}{6}C\left(1-\frac{\delta}{\delta_c}\right)p_{ik}^6-D\sigma_{ik}p_{ik}+\frac{1}{2}\mu(\nabla p_{ik})^2, \tag{5}$$

where A, B, C, and D are expansion parameters. Considering the ''polar'' character of the interaction of the defects and the consequent appearance of nonlocality, a term quadratic in the gradient of p_{ik} has been introduced in the expansion of the free energy, where μ is the nonlocality parameter. The solid lines in Fig. 1 show the ''thermodynamic'' branches[7] corresponding to minima of the free energy. The points $P(\sigma_{xz}^c,p_{xz}^c)$ and $S(\sigma_{xz}^t,p_{xz}^t)$ are points of a transition to the ''dynamical'' branches.

The dissipative function for a medium relaxing by flow and as a result of the development of defects has the form[4]

$$TP_s=-\frac{1}{T}q_k\nabla_k T+\sigma_{ik}e_{ik}^{\nu}-\frac{\delta F}{\delta p_{ik}}\dot{p}_{ik}\geqslant 0, \tag{6}$$

where T is temperature, q_k is heat flux, $\delta F/\delta p_{ik}$ is the thermodynamic force acting on a system when p_{ik} is different from its equilibrium value, and $e_{ik}^{\nu}=e_{ik}-\dot{p}_{ik}$ is the ''viscous'' component of the rate-of-strain tensor. The condition that the dissipative function be positive-definite leads to a system of equations for the tensor variables:

$$\sigma_{ik}=\eta e_{ik}^{\nu}+\chi\dot{p}_{ik}, \tag{7}$$

$$-\frac{\delta F}{\delta p_{ik}}=-\chi e_{ik}^{\nu}+\zeta\dot{p}_{ik}, \tag{8}$$

where η, χ, and ζ are kinetic coefficients. For the case of simple shear, from Eq. (7) follows an expression for the effective viscosity

$$\eta_{im}=\frac{\sigma_{xz}}{e_{xz}}=\eta-(\eta-\chi)\frac{\dot{p}_{xz}}{e_{xz}}. \tag{9}$$

This is a kinetic equation (8) for the nonequilibrium rate-of-strain fluctuations due to defects.[4] Transitions through the bifurcation points δ_c and δ_* lead to a sharp change in the symmetry of the distribution function as a result of the appearance of some orientationally degenerate macroscopic modes of the tensor p_{ik}. The effect of transitions on the evolution of defect-induced nonequilibrium rate-of-strain fluctuations is determined by the type of bifurcation — the group properties of the kinetic equation for the tensor p_{ik}

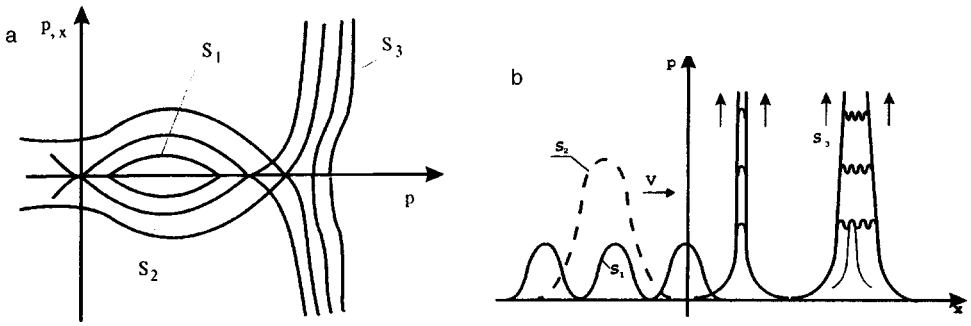

FIG. 2. Types of heteroclines and the corresponding characteristic forms.

for different domains of δ ($\delta > \delta_*$, $\delta_c < \delta < \delta_*$, $\delta < \delta_c$). The qualitative relationships governing the changes in the behavior of the system are reflected in Fig. 2 in the form of families of heteroclines which are solutions of the equation

$$A\left(1-\frac{\delta}{\delta_*}\right)p_{xz}+Bp_{xz}^3-C\left(1-\frac{\delta}{\delta_c}\right)p_{xz}^5+\frac{\partial}{\partial x}\left(\mu\frac{\partial p_{xz}}{\partial x}\right)=0. \tag{10}$$

In the region $\delta > \delta_*$ this equation is of the elliptic type with periodic solutions with spatial scale Λ and possesses p_{ik} anisotropy determined mainly by the applied stress. This distribution of p_{ik} gives rise to weak pulsations of the velocity without introducing any qualitative changes in the character of the laminar flow. As $\delta \to \delta_*$ Eq. (8) changes locally from elliptic to hyperbolic (separatrix S_2), and the periodic solution transforms into a solitary-wave solution. This transition is accompanied by divergence of the inner scale Λ: $\Lambda \approx -\ln(\delta - \delta_*)$. In this case the solution has the form $p_{xz}(\xi) = p_{xz}(x - Vt)$. The wave amplitude and velocity and the width of the wave front are determined by the parameters of the nonequilibrium (orientational) transition:

$$p_{xz}=\frac{1}{2}p_a[1-\tanh(\xi l^{-1})], \quad l=\frac{4}{p_a}\left(2\frac{\mu}{A}\right)^{1/2}. \tag{11}$$

The velocity of the solitary wave is $V = \mu A(p_a - p_m)/(2\zeta^2)$, where $p_a - p_m$ is the jump in p_{xz} in the course of an orientational transition. A transition through the bifurcation point δ_c (separatrix S_3) is accompanied by the appearance of spatiotemporal structures of a qualitatively new type characterized by explosive accumulation of defects as $t \to t_c$ in the spectrum of spatial scales (peaking regimes).[8] In this case the kinetics of p_{xz} is determined by the difference of the exponents of the higher-order terms in the expansion in Eq. (5). Assuming a power-law dependence of the nonlocality parameter on p_{xz}, the kinetic equation (8) can be written in the form

$$\frac{\partial p}{\partial t} \approx S(p_c)p^{\omega}+\frac{\partial}{\partial x}(\mu_0(p_c)p^{\beta})\frac{\partial p}{\partial x}, \tag{12}$$

where $p = p_{xz}/p_c$ and $\omega = 5/3$. In Ref. 8 it is shown that for equations of the type (12) the developed stage of kinetics of p in the limit $t \to t_c$ can be described by a self-similar solution of the form

$$p_A(x,t) = g(t)f(x). \tag{13}$$

The function $f(x)$ can be determined by solving the corresponding eigenvalue problem. For example, for the case $\omega=\beta+1$ the self-similar solution of Eq. (12) has the form

$$p(x,t)=[S_0(t-t_0)]^{-1/\beta}\left(\frac{2(\beta+1)}{\beta(\beta+2)}\sin^2\left(\frac{\pi x}{L_T}+\pi\theta\right)\right)^{1/\beta}, \tag{14}$$

where θ is a random number in the interval (0,1). The scale L_T, the so-called fundamental length,[8] has the meaning of a spatial period of the solution (14):

$$L_T=\frac{2\pi}{\beta}((\beta+1)\mu_0 S_0^{-1})^{1/2}. \tag{15}$$

As follows from Eq. (14), the parameter p and the flux $-\mu_0 p^\beta(\partial p/\partial x)$ vanish at the points $x_k=C+kL_T$ (here $C=-L_T$ and k assumes the values $k=\pm1,\ \pm2,\ \pm3,\ \ldots$). Moreover, Eq. (14) describes the independent ''explosive'' growth of p (peaking regime)[8] over the fundamental length L_T. In the interval $\delta_c<\delta<\delta_*$ the rate-of-strain fluctuations ''conform'' to the spectrum of solitary waves, meaning that $e_{ik}\approx\dot{p}_{ik}$, and Eq. (9) gives the asymptotic viscosity $\eta=\chi$. The independence of the viscosity of condensed media for rates of strain $e\sim10^4-10^6$ s^{-1} was established in Ref. 9 in measurements of the decay of disturbances on shock-wave fronts. A surprising result of these experiments is that the viscosity is virtually constant $\eta\approx10^4$ P for all condensed media studied (aluminum, lead, water, mercury). It is natural to conjecture that the maximum penetration depth into the region of metastability (orientational transition), the point S in Fig. 1, is reached for rates of strain $e\sim10^5$ s^{-1}. This ensures resonance excitation of collective modes in the form of a spectrum of solitary waves, and in consequence $e_{ik}\approx\dot{p}_{ik}$. A similar result is also observed in a close interval of rates of strain under shock-initiation of plastic instability in metals, where a sharp transition to an orientationally ordered state in an ensemble of defects gives rise to regions of shear instability (adiabatic shear bands[3]). The behavior of the ensemble of defects conforms to the kinetics in the peaking regime after the instability threshold $p=p_c$ is crossed for $\delta<\delta_c$, as has been observed experimentally[10] in the shock-wave loading of materials with microsecond loading durations during so-called ''spallation'' fracture. The stress wave was initiated in a circular rod using a gas gun, and the loading parameters (stress amplitude, fracture time, Fig. 3) were measured using a laser differential interferometer.[1] Increasing the amplitude of the shock pulse sharply decreases the dependence of the fracture time τ_c on the pulse amplitude σ_a (''dynamical'' branch with spallation[2]). The appearance of this branch is accompanied by a qualitative change in the fractographic pattern of the fracture surface, where multiple generation of mirror-image zones is observed. The diameter of the zones, which are nuclei of macroscopic cracks, corresponds to the localization scale of disperse fracture for the moment of onset of the peaking regime. The localization scales (fundamental lengths) decrease with increasing amplitude of the supercritical stresses. The reason for the weak dependence $\tau_c(\sigma_a)$, which is an indicator of self-similarity, becomes obvious: Resonance excitation of the spectrum of characteristic forms in the peaking regime.

Some experimental data on the physical mechanisms leading to the development of instabilities in condensed media indicate the possibility of describing instabilities in liquids on the basis of an analysis of the kinetics of nonequilibrium fluctuations, if the latter are viewed as real defects in the structure of the liquids.[11] In the case of liquids mesos-

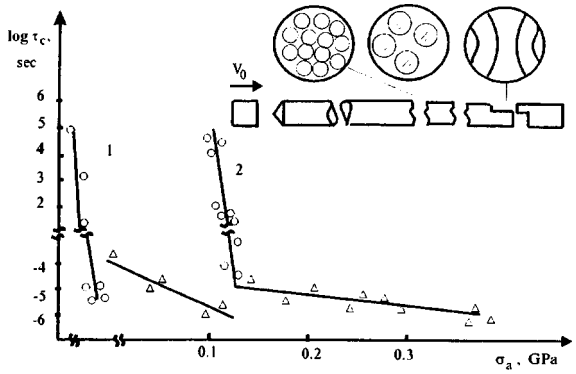

FIG. 3. Sample fracture time τ_c for polymethyl methacrylate (*1*) and ultraporcelain (*2*) versus the amplitude σ_a of the stress pulse. Inset: Schematic illustration of the form of the fracture surface in different cross sections of the spallation.

copic defects, being by their very nature nonequilibrium fluctuation displacement (or rate-of-strain) fields in solids, are also regarded as real structural defects which are produced during collective motion of groups of molecules. This mechanism of motion does not correspond to the conventional diffusion mechanism of momentum transfer in simple liquids. Apparently, Frenkel[12] was the first to call attention to the analogy in the mechanisms of flow of solids and liquids, noting that ''... x-ray diffraction pictures of liquids are similar to those of microcrystalline solids, and it would be possible to interpret their general features on the basis of the idea that a liquid consists of a large number of randomly oriented submicroscopic-size crystals'' and ''... the widely held view that the fluidity of liquids is caused by the absence of shear elasticity, i.e., by a zero shear modulus, ... is incorrect (except, possibly, for the case of liquid helium II).'' These statements are confirmed by measurements of the shear moduli and relaxation spectra of simple liquids,[13] where relaxation times $\tau \approx 10^{-5}$ s, differing by 5 to 6 orders of magnitude from the molecular (diffusion) relaxation times, were established. The relaxation time τ can be estimated, using Einstein's formula, as the characteristic self-diffusion time $\tau_m = \Delta^2/6D_{sd}$, where Δ is the distance between the fluid particles and D_{sd} is the self-diffusion coefficient. In the case of weakly-viscous liquids an estimate of the relaxation time gives $\tau_m \approx 10^{-10}$–10^{-12} s. However, in many cases the collective effects arising in liquids as a result of the interaction of groups of molecules can play an important role. The relaxation of a nonequilibrium state of groups of molecules requires a coordinated displacement and reorientation of many molecules and therefore involves longer times. In Ref. 13 the existence of shear elasticity accompanying the superposition of shear oscillations in a liquid at frequencies 10^5 Hz is explained by these collective effects. A coordinated displacement of groups of molecules (similarly to the relative slipping of blocks or grains in solids) can be realized during nucleation of mesoscopic defects arising between these groups of molecules.

The following scenario of the development of instabilities in a liquid is possible in accordance with the characteristic features, examined above, of the nonlinear behavior of ensembles of defects. A transition to turbulence accompanying intensification of flow occurs as the parameter δ decreases as a result of an increase in the density of defects.

The region $\delta > \delta_*$ corresponds to defect-induced fluctuations of the displacement (rate-of-strain) field which have the form of weak periodic pulsations of the velocity. The transition through the bifurcation point δ_* (the region $\delta_c < \delta < \delta_*$) leads to nucleation in the flux of solitary waves which are generated as a result of orientational instability in an ensemble of microscopic shears. The conditions for developed turbulence obtain in the region $\delta < \delta_c$, where the flow conforms to nonequilibrium macroscopic rate-of-strain fluctuations which are due to the development of a spectrum of characteristic forms p_{ik} in the peaking regime. Evidently, the minimum scale corresponding to a simple structure (Fig. 2) determines the lower limit of the inertial interval (upper limit for the viscous interval) introduced by Kolmogorov.[14]

It is interesting to compare the real picture of turbulent flow with the scenario given by the dynamics of p_{ik}. The dynamics of the development of turbulence has been investigated in Ref. 15 in an analysis of the evolution of a turbulent spot in a Poiseuille flow with Reynolds numbers $R \sim 840-1500$. It is observed that the turbulent spot has the form of a triangular wing, and the turbulent motion arises inside a region on the boundary of which disturbances in the form of solitary waves arise. These waves, generated on the boundary of the spot, propagate into the laminar zone and transform into quasiperiodic damped pulsations of the velocity. The motion of solitary waves in the direction of the spot results in secondary instability and growth of the spot. This experimentally observed scenario agrees with the nonlinear dynamics of macroscopic defect-induced rate-of-strain fluctuations. The laws established for the development of instabilities in condensed media suggest the possible existence of a bifurcation tree, leading to turbulence,[16] that can be described on the basis of a kinetic approach.[17]

This work was supported in part by the Russian Fund for Fundamental Research under Grant 96-01-00471.

[a)]e-mail: lab13@icmm.perm.su

[1] V. V. Belyaev and O. B. Naĭmark, Dokl. Akad. Nauk SSSR **312**, 289 (1990) [Sov. Phys. Dokl. **35**, 436 (1990)].
[2] O. B. Naĭmark and V. V. Belyaev, Fiz. Goreniya Vzryva **25**, 115 (1989).
[3] O. B. Naimark, in *Advances in Fracture Research*, edited by B. Karihaloo, Sydney, Australia, 1997, Vol. 6, p. 2795.
[4] O. B. Naĭmark, ''On the thermodynamics of strain and fracture of solids containing microcracks'' [in Russian], Preprint, Institute of Mechanics of Continuous Media, Academy of Sciences of the USSR (1982).
[5] O. B. Naimark, in *Proceedings of IUTAM Symposium on Nonlinear Analysis of Fracture*, edited by J. R. Willis, Cambridge, England (1997), p. 285.
[6] L. R. Botvina and G. I. Barenblatt, Problemy Prochnosti **12**, 17 (1985).
[7] G. Nicolis and I. Prigogine, *Self-Organization in Nonequilibrium Systems: From Dissipative Structures to Order Through Fluctuations*, Wiley Interscience, Wiley, New York, 1977 [Russian translation, Mir, Moscow, 1979].
[8] S. P. Kurdyumov, ''Eigenfunctions of the combustion of a nonlinear medium and the contructive laws of its organization'' [in Russian], Preprint, Keldysh Institute of Applied Mathematics, Soviet Academy of Sciences, 1979.
[9] A. D. Sakharov, R. M. Zaĭdel', V. N. Mineev, and A. G. Oleĭnik, Dokl. Akad. Nauk SSSR **159**, 1019 (1964) [Sov. Phys. Dokl. **9**, 1091 (1965)]; V. N. Mineev and E. N. Savinov, Zh. Éksp. Teor. Fiz. **52**, 629 (1967) [Sov. Phys. JETP **25**, 411 (1967)]; V. N. Mineev and R. M. Zaĭdel', Zh. Éksp. Teor. Fiz. **54**, 1633 (1968) [Sov. Phys. JETP **27**, 874 (1968)].
[10] E. N. Bellendir, V. V. Belyaev, and O. B. Naĭmark, Pis'ma Zh. Tekh. Fiz. **15**(13), 90 (1989) [Sov. Tech. Phys. Lett. **15**(7), 534 (1989)].

[11] O. B. Naĭmark, Pis'ma Zh. Tekh. Fiz. **23**(13), 81 (1997) [Tech. Phys. Lett. **23**(7), 529 (1997)].
[12] J. Frenkel, *Kinetic Theory of Liquids*, Clarendon Press, Oxford, 1946 [cited Russian original, Nauka, Leningrad, 1975].
[13] B. V. Derjagin *et al.*, Polymer **30**, 1 (1989).
[14] A. N. Kolmogorov, Dokl. Akad. Nauk SSSR **30**, 299 (1941).
[15] D. R. Carlson, S. E. Widnall, and M. F. Peeters, J. Fluid Mech. **121**, 487 (1982).
[16] G. M. Zaslavskiĭ and R. Z. Sagdeev, *Introduction to Nonlinear Physics* [in Russian], Nauka, Moscow, 1988.
[17] Yu. L. Klimontovich, Physica B **229**, 51 (1996).

Translated by M. E. Alferieff

ERRATA

Erratum: Quantum tunneling in ferromagnetic nanoparticles interacting with a spin thermostat: effective Hamiltonian [JETP Lett. 67, No. 1, 28–33 (10 January 1998)]

I. S. Tupitsyn
Kurchatov Institute Russian Science Center, 123182 Moscow, Russia

[S0021-3640(98)02109-4]

PACS numbers: 61.46.+w, 75.50.Tt, 75.10.Jm, 99.10.+g

The title of this article should read as follows:

Quantum tunneling in ferrimagnetic nanoparticles interacting with a spin thermostat: effective Hamiltonian

The first sentence in the abstract should read as follows: An effective Hamiltonian is obtained which describes quantum tunneling in ferrimagnetic nanoparticles in the presence of a hyperfine interaction of the electron spins in the nanoparticle with the microscopic spins in the environment (such as paramagnetic impurities or nuclear spins).

The publisher apologizes for this error.

